"G. d'Annunzio"
University of Chieti-Pescara

Center of Advanced Studies and Technology

Ph.D. course in Biomolecular and Pharmaceutical Sciences
Curriculum: **Molecular Medicine**
Cycle XXXVI

Ph.D. Thesis:

Understanding pathological mechanisms of Marinesco-Sjögren syndrome

Department of Innovative Technologies in Medicine & Dentistry
Unit of Biochemistry and molecular biology
SSD BIO 11

PhD student
Dr. **Francesca Potenza**
Matr. N° 3216147

Coordinator
Prof. **Assunta Pandolfi**

Supervisor
Prof. **Michele Sallese**

Academic years 2020/2024

Index

1. **Introduction** 3
   - Clinical Features 3
   - Molecular aspects 5
   - Potential treatments 7
   - Animal model 8
   - In vitro model 9
   - Main research proposal 10
2. **First breakthrough** 11
   - Rationale 11
   - Results 11
   - Discussion 23
   - Material and methods 23
3. **CRISPR-Cas9 C2C12 SIL1 clone generation** 29
   - Rationale 29
   - Results 30
   - Discussion 32
   - Material and methods 33
4. **Primary cell culture** 36
   - Rationale 36
   - Results 37
   - Material and methods 40
5. **Second breakthrough** 43
   - Rationale 43
   - Results 44
   - Discussion 51
   - Material and methods 53
6. **Third breakthrough** 59
   - Rationale 59
   - Results 60
   - Discussion 66
   - Material and methods 66
7. **Conclusion** 71
   - Summary 71
   - Discussion on key findings 72
   - Conclusion and further research 75
8. **Bibliography** 77

1 Introduction

Clinical features

Marinesco-Sjögren syndrome (MSS) represents a fascinating puzzle in neurogenetics. It is an extremely rare neuromuscular disorder that manifests itself from an early age. Its worldwide prevalence is not precisely known, but it is estimated to affect approximately one in a million people[1]. Discovered in the 1930s, MSS remains a medical enigma due to its complexity and the great variability of its symptoms. MSS is a genetic disease that, in 50% of cases, is caused by a mutation in the SIL1 gene and is inherited in an autosomal recessive manner. Numerous pathogenic variants of this gene have been described, but a direct and constant correlation between the type of mutation and the severity of the disease has not yet been found [2]. The clinical manifestations of MSS are highly variable, despite the fact that the SIL1 protein is present in all cells of the body, the reason why only some tissues, such as the cerebellum, muscles and lens, are affected by this disease remains unclear [3].

The main symptoms of MSS are cerebellar ataxia, myopathy and bilateral cataracts as shown in Figure 1 [4]. Cataracts can be present at birth or develop in the first years of life and often progress rapidly, requiring surgery around the age of 10 [5]. At the muscular level, patients present with hypotonia, muscle weakness, delayed psychomotor development and myopathy. Muscle fibers degenerate and biopsies often show replacement by fibroadipose tissue and changes in both fiber size and type composition [6,7]. The cerebellum is affected by degeneration of Purkinje neurons, causing atrophy and subsequent ataxia with impaired balance. The combination of muscle and cerebellar defects causes delays in motor and speech development. Cerebellar lesions may cause dysmetria, dysdiadochokinesia, dysarthria, and postural and gait ataxia. Motor function progressively deteriorates during growth, reaching a plateau of varying severity from patient to patient, but most of them will require walking aids. MSS patients often exhibit short stature and may have skeletal abnormalities[1]. Due to SIL1's role in neuronal development, some individuals may also experience mild to severe intellectual disability [8,9]. Another common symptom is primary gonadal failure, characterized by decreased sex

hormone production, which contributes to short stature and delayed puberty. While MSS is a debilitating multi-organ disease, it does not affect lifespan[1].

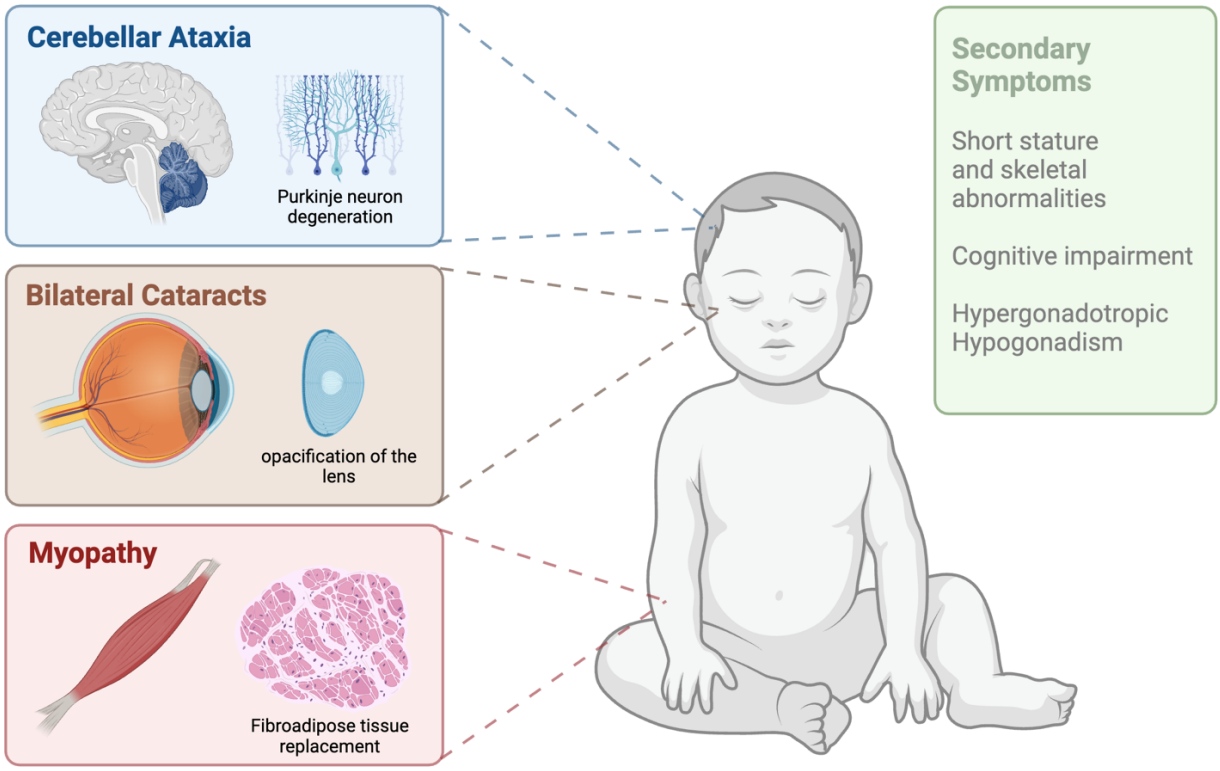


Figure 1. Main clinical signs of patients affected from Marinesco-Sjögren syndrome
From "*Potential approaches for the treatment of Marinesco –Sjögren syndrome".* Viele M. et al. DOI: 10.61012_20248_590

Diagnosis is based on clinical evaluation, supplemented by magnetic resonance imaging (MRI) to assess cerebellar atrophy, ophthalmological examinations to identify cataracts, and muscle biopsies to confirm myopathy. Genetic testing to identify biallelic mutations in the SIL1 gene is used to confirm a clinical diagnosis of MSS.

Currently, there's no cure for MSS. While cataracts can be corrected surgically, other symptoms require supportive therapies to manage and slow their progression. Hypergonadotropic hypogonadism is treated with hormone therapy to prevent osteoporosis. Psychomotor difficulties are typically monitored and addressed by neurologists and physiotherapists[1]. The wide range of symptoms and the rarity of MSS present significant challenges in understanding the underlying pathological mechanisms. However, utilizing animal models for preclinical research and exploring personalized medicine approaches may lead to advancements in treating this condition.

Molecular aspects

SIL1 protein plays a crucial role in maintaining the balance of the endoplasmic reticulum (ER) by aiding in protein folding[10]. Sil1 is indeed a nucleotide exchange factor for BiP, the main ER chaperone and primary sensor of ER stress. BiP's ability to bind newly synthesized unfolded proteins and to release the folded substrate is tightly regulated by a cycle of ATP binding (Figure 2), hydrolysis, and nucleotide exchange. ATP binding promotes an open conformation, allowing low-affinity binding to hydrophobic regions of unfolded proteins. ATP hydrolysis stabilizes the interaction, closes the lid, and facilitates client protein folding. ADP exchange for ATP opens the lid, releasing the folded protein. SIL1 specifically binds to ADP-bound BiP to catalyze the release of ADP and re-binding of ATP [11]. If this nucleotide exchange is defective, as in the case of SIL1 loss, BiP remains associated with its client protein, ultimately leading to accumulation of unfolded proteins, ER stress and activation of the unfolded protein response (UPR).

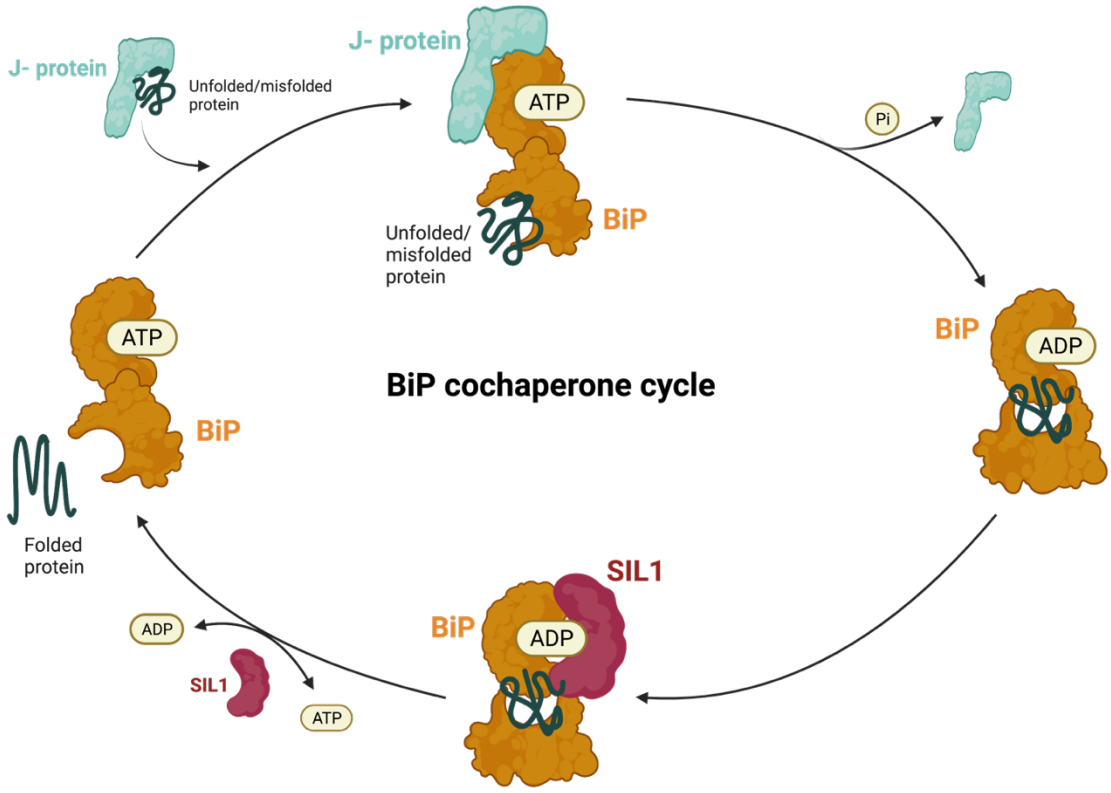


Figure 2. BiP's ATP cycle
From Study of the pathological mechanisms in the Marinesco-Sjögren syndrome by means of a multi-omics approach. EWCD Poster Potenza F. et al.

The UPR is a complex signaling pathway whose purpose is to restore ER proteostasis by boosting ER protein-folding capacity, degrade unfolded proteins, and inhibit protein synthesis as a mechanism to reduce the ER load. This is achieved through activation of three distinct ER transmembrane protein sensors: inositol-requiring enzyme 1 (IRE1), activating transcription factor 6 (ATF6), and protein kinase R (PKR)-like endoplasmic reticulum kinase (PERK) (Figure 3). PERK phosphorylates eIF2α, suppressing general protein synthesis while allowing specific transcripts, like ATF4, to be translated. ATF4 activates downstream effectors, including CHOP, a pro-apoptotic protein. IRE1 splices XBP1 and degrades mRNAs, while ATF6 is activated through proteolytic cleavage and translocates to the nucleus to activate UPR genes. Although UPR is a pro-survival response, when its mechanisms fail to resolve stress, its prolonged activation will lead to cell death[12]. ORP150, another chaperone with nucleotide exchange activity for BiP, could potentially compensate for SIL1 deficiency. Overexpression of ORP150 has been shown to prevent ataxia and muscle problems in woozy mice[13]. However, spontaneous overexpression of ORP150 may not be sufficient to fully replace SIL1. The extent of UPR activation likely correlates with cellular damage. In non-clinically diseased cells, such as fibroblasts, UPR activation is limited, while it becomes more pronounced in skeletal muscle and Purkinje cells, as observed in preclinical models[7,14,15].

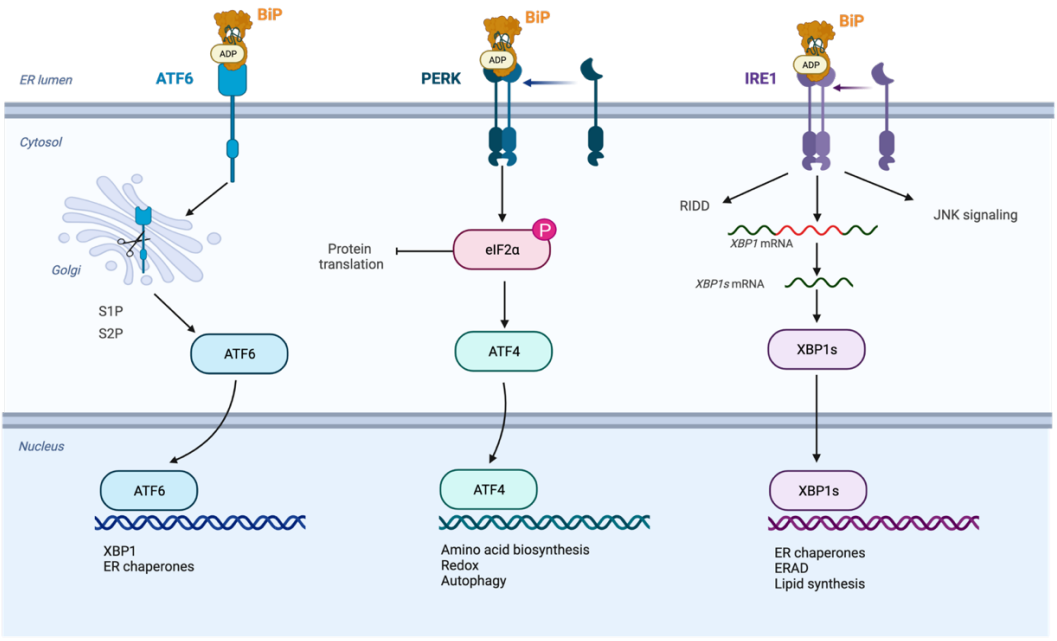


Figure 3. Unfolded Protein Response (UPR)
From *Study of the pathological mechanisms in the Marinesco-Sjögren syndrome by means of a multi-omics approach.* EWCD Poster Potenza F. et al.

Potential treatments

Marinesco-Sjögren syndrome (MSS) is a neurodegenerative disease caused by misfolded proteins. The UPR is a cellular response that occurs when misfolded proteins accumulate within the cell. Among the sensors of the UPR, protein kinase R (PERK) plays a particularly important role in neurodegenerative diseases. When PERK is activated, it inhibits protein synthesis, leading to a deficiency of proteins essential for the survival of neurons. This process contributes to neuronal degeneration [16].

In recent years, scientists have explored the idea of blocking PERK activity trying to slow the progression of MSS. Some preclinical studies have shown promising results using PERK inhibitors, such as GSK2606414. These inhibitors have been shown to restore protein synthesis and improve motor function in animal models of MSS[17,18]. However, it is important to note that these are still preliminary studies and that further research is needed to fully understand the side effects and long-term efficacy of these therapies.

Another potential therapeutic approach for MSS is represented by the so-called "chemical chaperones". These are small molecules that can bind to misfolded proteins and help them reach the correct conformation. Some chemical chaperones are already used to treat other genetic diseases, such as Fabry disease. However, for MSS it is still necessary to identify specific chaperones able to interact with the SIL1 protein, whose mutation is at the basis of the disease[19].

Finally, gene therapy represents a viable option for the treatment of MSS. The idea is to introduce a healthy copy of the SIL1 gene into patient cells, thus correcting the genetic defect that is at the basis of the disease. Recent advances in gene therapy have made it possible to use viral vectors to deliver the correct gene into cells. Although clinical trials of gene therapy for MSS are still in their early stages, the results obtained in other genetic diseases are very encouraging.[20]
In conclusion, research on MSS has made significant progress in recent years (Figure 4). Although there is still no definitive cure for this disease, the different therapeutic strategies being studied offer real hope for patients and their families.

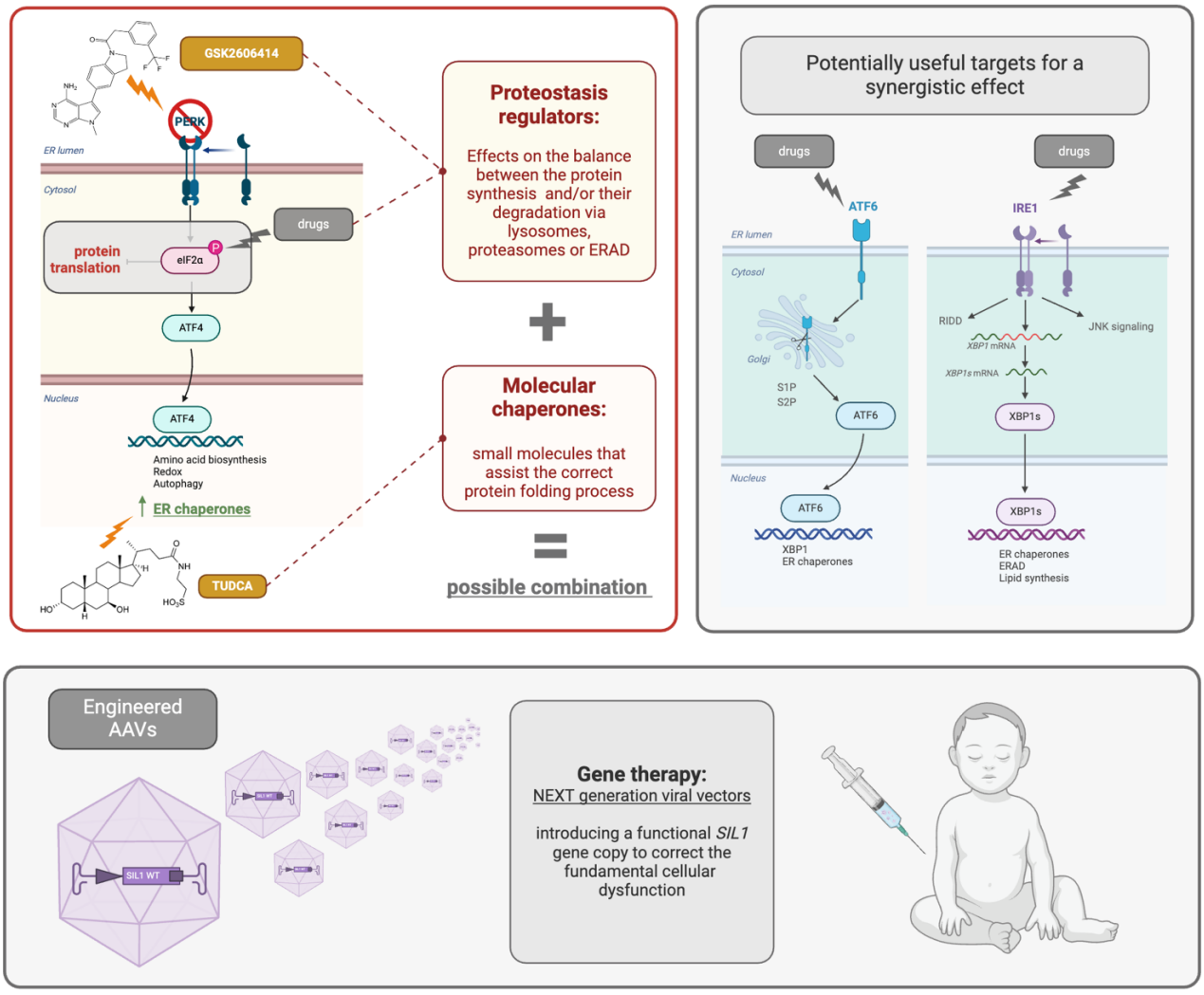


Figure 4. Potential treatments for Marinesco-Sjögren syndrome.
From "*Potential approaches for the treatment of Marinesco –Sjögren syndrome".* Viele M. et al. DOI: 10.61012_20248_590

Animal models

Two mouse models have been developed to study Marinesco-Sjögren syndrome (MSS). The woozy mouse carries a spontaneous mutation in the SIL1 gene, while the SIL1Gt mouse is genetically engineered[21]. Both models exhibit symptoms similar to human MSS, including cerebellar ataxia, muscle weakness, and cataracts. These models are valuable tools for understanding the disease's mechanisms and developing potential treatments.

The woozy mouse carries a mutation in the SIL1 gene, which is the primary cause of MSS in humans[22]. As a result, these mice exhibit key pathological features of the disease, including cerebellar atrophy and myopathy. In the cerebellum of woozy mice, the UPR is

activated in Purkinje cells, leading to their degeneration and cerebellar atrophy. This is achieved by increased levels of markers, such as CHOP and XBP-1, as well as signs of apoptosis, including TUNEL positivity and caspase-3 activation. In the muscles of woozy mice, the UPR is also activated, leading to muscle atrophy and other pathological changes. These changes include alterations in the sarcoplasmic reticulum, mitochondria, and myonuclei. Additionally, there is evidence of impaired autophagy and lysosome function, suggesting that the accumulation of misfolded proteins may also contribute to muscle damage[7,18].

SIL1Gt mice exhibit a phenotype similar to the woozy mouse, suggesting the crucial role of SIL1 in skeletal muscle physiology and neurodegeneration. The study by Ichhaporia et al.[15] revealed a progressive decrease in muscle strength in SIL1Gt mice as they aged. This was accompanied by structural abnormalities in their muscle tissue, including irregular fibers and myofibrillar disorganization. A proteomic analysis showed significant changes in the expression of hundreds of proteins in the muscles of SIL1Gt mice. These changes affected various cellular compartments and physiological pathways, such as cation channel activity, insulin receptor signaling, and glucose metabolism[15]. While SIL1Gt mice do not exhibit bilateral cataracts, they can develop unilateral cataracts sporadically[4].

In vitro models

Rare diseases, by definition, affect a limited number of people. This makes it hard and expensive to conduct large-scale clinical trials. The low prevalence of rare diseases represents an obstacle to obtaining sufficient biological samples to create cell lines. Furthermore, genetic are often characterized by great variability, making development of cellular models that represent all possible mutations very complicated.

The lack of adequate cellular models is therefore a major challenge in this research niche. This shortage has profound implications for the understanding, diagnosis and development of effective therapies for these diseases. Cellular models offer a low-cost, simplified but powerful way to study the molecular mechanisms underlying a disease and the development of new technologies, such as CRISPR-Cas9 genome editing, offers new

opportunities to create personalized and representative cellular models to delve deeper into the pathological mechanisms[23].

For this research project we dispose of skin fibroblasts from a patient affected by MSS, but given the rarity of the disease it might be very difficult to make a comparison with other patients' derived cells. The disease, as described above, also does not primarily affect this cell line, but rather skeletal muscle cells and cerebellum Purkinje cells. Therefore, besides patient's fibroblasts and possible primary cultures from Woozy mice there is a clear need to develop more manageable, disease specific, in vitro models.

Main research proposal

My doctoral research focused on understanding the molecular mechanisms behind Marinesco-Sjögren syndrome (MSS). To accomplish this, I initiated the development of an in vitro model that accurately mirrored the pathological state observed in MSS patients. I generated a CRISPR/Cas9-edited C2C12 cell line, a commercial murine myoblast line, to precisely target and disrupt the SIL1 gene, creating a stable knockout (KO) model. This model, mirroring the genetic alterations in MSS patients, would have provided a valuable tool for investigating the disease's pathophysiology.

Simultaneously, to gain a comprehensive understanding of the molecular changes associated with MSS, we employed multiomic analyses. This approach involved concurrently examining multiple levels of biological information, including genomics, transcriptomics, and proteomics. By comparing the omics data from my in vitro model to that of patient fibroblasts, we aimed to identify key pathways and molecular processes disrupted in MSS. Through in silico analysis of the omics data, we sought to uncover altered pathways and gene networks implicated in MSS. Through the modulation of these pathways, I hypothesized that we could decipher the root causes of muscle cell death or the survival mechanisms of other cell types in the disease context.

In the following paragraphs, I will delve into each of these research steps in detail, discussing the published papers that have contributed to our understanding over these years.

2 First breakthrough

Proteomic Analysis of Marinesco–Sjögren Syndrome Fibroblasts Indicates Pro-Survival Metabolic Adaptation to SIL1 Loss. November 2021

https://doi.org/10.3390/ijms222212449

Rationale

Although UPR seems to be the most obvious molecular consequence of SIL1 loss of function, it has not been fully ascertained whether this is the cause of the death or degeneration of the most affected cell types. It would be realistic to imagine that a set of alterations lead to the final pathological clinical picture.

The other question that arises spontaneously is: why, if SIL1 is a protein constitutively expressed by all cells and tissues of the body, when a genetic mutation with loss of its function is present, only some cell types degenerate? How can the other cells continue to perform their functions normally?

To explore the pathogenic mechanisms and potential adaptive responses to SIL1 deficiency, we conducted cellular and proteomic analyses on skin fibroblasts from a young patient with the SIL1 R111X mutation. While fibroblasts might not be directly affected in MSS, recent research suggests that their protein profile can provide insights into neuromuscular disease pathogenesis[24]. By examining the proteome of MSS patient fibroblasts (HF-MSS), we aimed to identify molecular changes beyond SIL1 loss.

Results

To determine if cultured skin fibroblasts from MSS patients (HF-MSS) displayed molecular and morphological changes similar to those observed in other cell types lacking SIL1, we examined UPR activation and autophagy[3,4]. Western blot analysis confirmed the absence of SIL1 protein and revealed modest activation of the PERK and ATF6 branches of the

UPR in HF-MSS cells. Specifically, levels of ATF4 and phosphorylated eIF2-α (at threonine 52) were elevated compared to control fibroblasts (HF-CT) (Figure 2.1. A). Additionally, cleaved ATF6 levels were increased, indicating stress-activated processing. However, there was no increase in sXBP1, suggesting no IRE1 activation (Figure 2.1 B). Furthermore, we examined the expression of several chaperones induced during ER stress. BiP and PDI were upregulated in HF-MSS cells, while ORP150 remained unaffected (Figure 2.1. C).

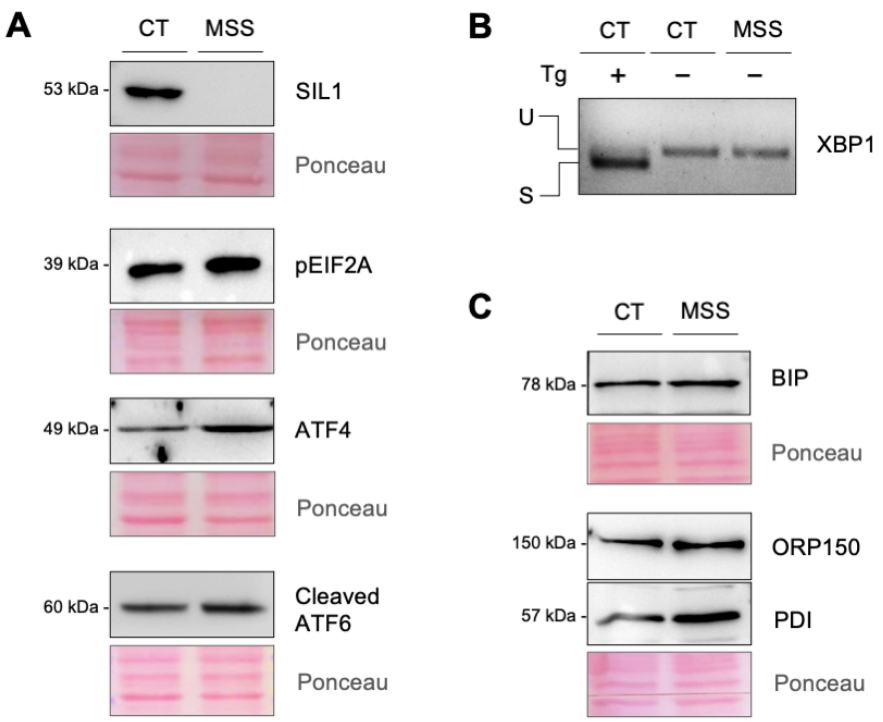


Figure 2.1. UPR activation in MSS patient fibroblasts. (A,C) HF-CT (CT) and HF-MSS (MSS) cultured under standard growth conditions were analyzed by Western blotting to assess the expression of SIL1, ATF4, ATF6, and the phosphorylated form of EIF2α (A), BiP, ORP150, and PDI (C) as indicated. Immunoblots are representative of at least two independent experiments. Ponceau S staining of the blots is shown to control for equal protein loading. (B) XBP1 splicing was assessed by PCR. HF-CT (first lane) treated with 1 μM Thapsigargin (Tg) for 6 h was used as a positive control. The higher and lower bands represent the unspliced (U) and spliced (S) forms of XBP1.

From "Proteomic Analysis of Marinesco–Sjögren Syndrome Fibroblasts Indicates Pro-Survival Metabolic Adaptation to SIL1 Loss". Potenza et al. https://doi.org/ 10.3390/ijms222212449

Autophagic vacuoles are another hallmark of MSS pathology, observed in patient muscle tissue, woozy mouse muscle and Purkinje cells, and various SIL1-deficient cell lines. To investigate their presence in HF-MSS cells, we stained them for LAMP1, a lysosomal marker. Fluorescence microscopy revealed a striking number of large, ring-like LAMP1-positive structures, likely enlarged lysosomes or autophagic vacuoles (Figure 2.2 A). In contrast, control cells exhibited few such structures, displaying the typical cytosolic LAMP1-positive dots (Figure 2.2 A,B).

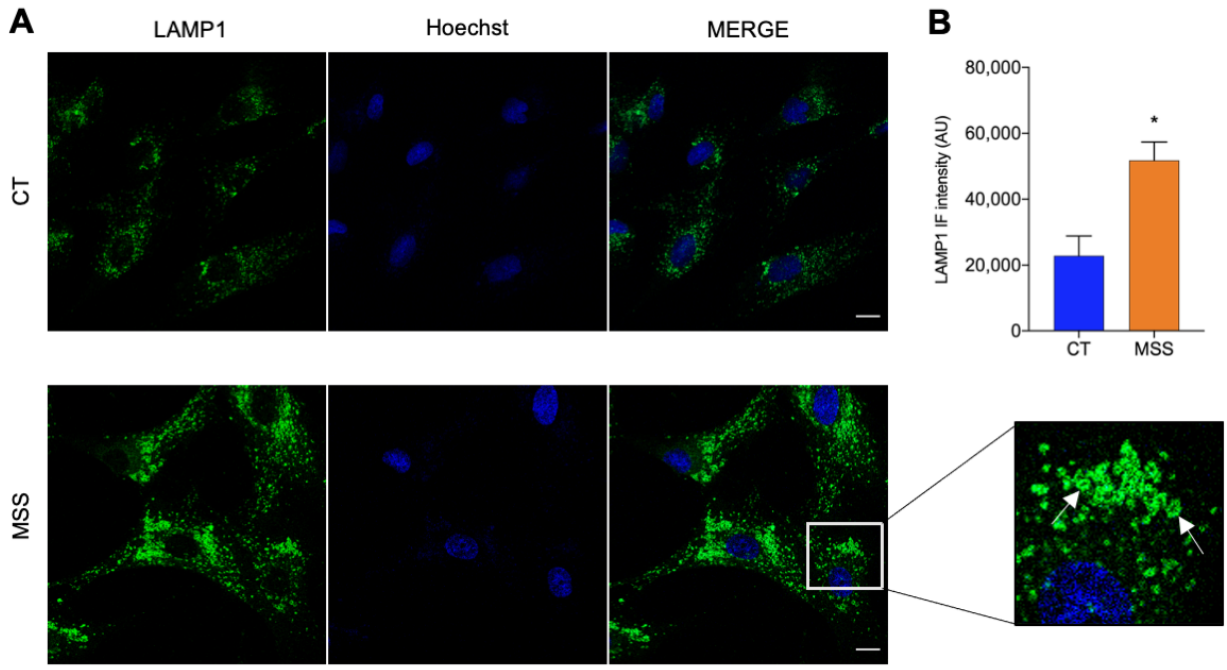


Figure 2.2. LAMP1-positive structures increase in HF-MSS cells. (A) HF-CT (CT) and HF-MSS (MSS) were plated on glass coverslips, fixed in PFA 4%, and processed for immunofluorescence. Confocal images of cells immunostained for LAMP1 (green) and reacted with Hoechst 33342 (blue) to stain the nuclei. The merge of green and blue channels is represented in the third panel. A magnification of the squared area is also shown. White arrows indicate ring-like structures. Scale bar: 20 μm. (B) Quantification of total LAMP1 staining shown in A. * $p < 0.05$.

From "Proteomic Analysis of Marinesco–Sjögren Syndrome Fibroblasts Indicates Pro-Survival Metabolic Adaptation to SIL1 Loss". Potenza et al. https://doi.org/ 10.3390/ijms222212449

Electron microscopy (EM) analysis revealed a higher frequency of cytoplasmic vacuoles containing membrane clusters and multilamellar bodies in HF-MSS cells compared to HF-CT (Figure 2.3. A,B). These structures were also more numerous in HF-MSS cells. Additionally, Western blot analysis showed upregulation of LC3-I, LC3-II, and LAMP1, while SQSTM1/p62 was downregulated (Figure 2.3. C). The increased lipidated LC3-II suggests enhanced autophagosome formation or impaired autophagic degradation. SQSTM1/p62, a receptor for ubiquitinated proteins, can be degraded by autophagic vacuoles. These findings collectively indicate an upregulated autophagic degradation pathway. Cell viability and apoptotic cell death, assessed by trypan blue staining and caspase-3 activation, were comparable between HF-MSS and control cells (data not shown). This initial characterization aligns with previous studies on other MSS cell models, demonstrating ER stress and a mild UPR activation without affecting cell survival or apoptotic cell death[17].

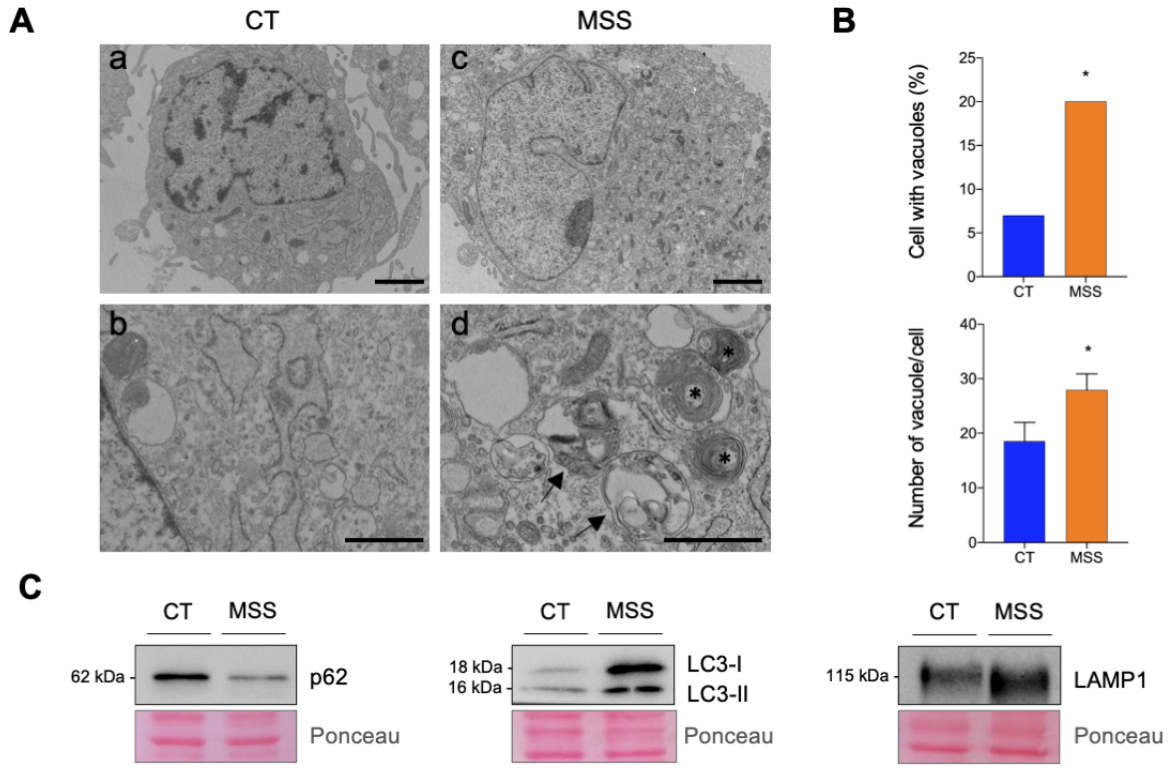


Figure 2.3. Electron microscopy (EM) and immunoblot analysis of autophagic vacuoles. (A) Ultrastructural alterations in HF-MSS. Representative EM micrographs of HF-CT (a) and HF-MSS (c) cells. Details at higher magnification of the cytoplasm of HF-CT (b) and HF-MSS (d) cells. HF-MSS cells accumulate vacuoles containing large clusters of membranes (arrowheads) and multilamellar bodies (asterisks). Scale bars: a and c: 2 µm; b and d: 1 µm. (B) Upper graph, percentage of HF-CT and HF-MSS cells exhibiting vacuoles/multilamellar bodies (n = 100 cells/group); lower graph, average number of vacuoles/multilamellar bodies per cell calculated by considering only the cells showing such structures. Statistical significance Chi square test (lower) and t-test (upper) * $p < 0.05$. (C) HF-CT (CT) and HF-MSS (MSS) cultured under standard growth conditions were analyzed by Western blotting for the expression of p62/SQSTM1 (p62), LC3, and LAMP1. Immunoblots are representative of at least two independent experiments. Ponceau S staining of the blots is shown to control for equal protein loading.

From "*Proteomic Analysis of Marinesco–Sjögren Syndrome Fibroblasts Indicates Pro-Survival Metabolic Adaptation to SIL1 Loss*". Potenza et al. https://doi.org/ 10.3390/ijms222212449

To explore molecular changes associated with MSS pathogenesis and potential adaptive responses to SIL1 loss, we conducted a proteomic analysis of HF-MSS and control fibroblasts. Using shotgun proteomics, we identified 625 differentially expressed (DE) proteins, with 305 downregulated and 320 upregulated (Figure 2.4. A). The high correlation between protein intensities in HF-MSS and HF-CT samples (R2 = 0.92) indicates reliable and reproducible relative quantification. This analysis provides a valuable dataset for further investigation into the molecular mechanisms underlying MSS.

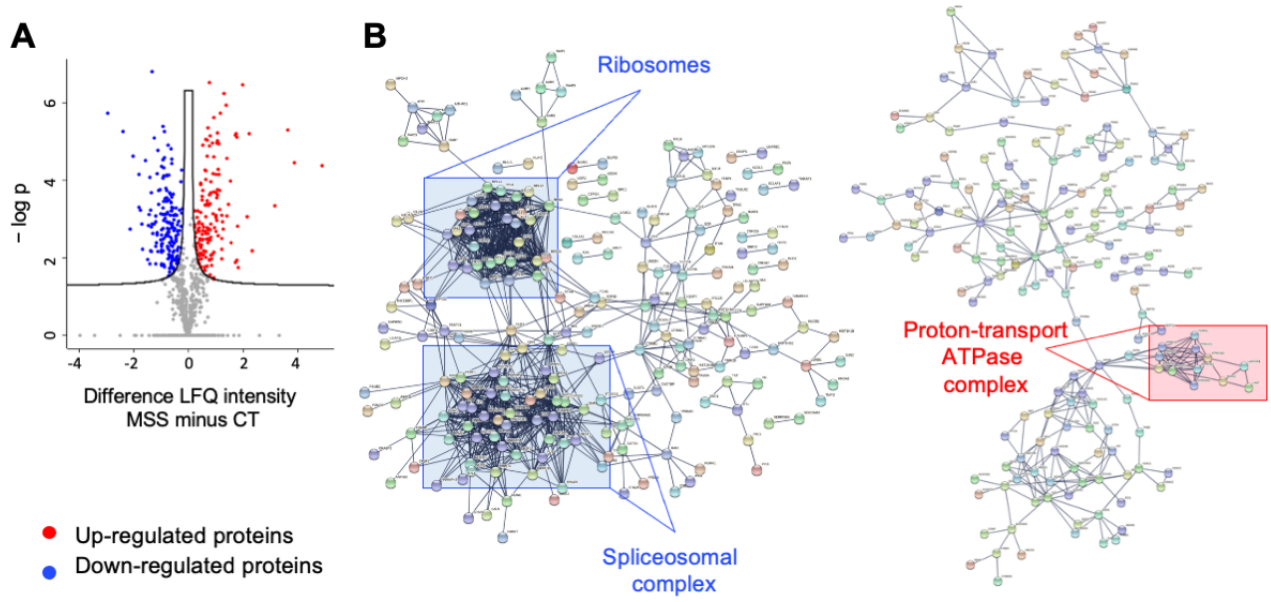


Figure 2.4. Proteomic analysis graphical networks. (A) Volcano Plot: Statistical analysis of differentially expressed proteins between HF-CT and HF-MSS cells, run by Perseus. LQF intensity of HF-MSS minus that of HF-CT was plotted against the negative logarithm of the p-values. (B) STRING network of proteins downregulated (left) and upregulated (right) in HF-MSS, confidence level set at 0.9. Squares indicate examples of clusters of interacting proteins involved in the indicated functions.

From "Proteomic Analysis of Marinesco–Sjögren Syndrome Fibroblasts Indicates Pro-Survival Metabolic Adaptation to SIL1 Loss". Potenza et al. https://doi.org/ 10.3390/ijms222212449

We used a combination of tools to understand how the proteins affected in HF-MSS (differentially expressed, DE) might be working together. One tool, STRING revealed a large network of connected proteins, with far more connections than expected by chance (Figure 2.4. B). This suggests these proteins aren't random, but rather work together in important pathways related to HF-MSS. Interestingly, even when they looked only at the most reliable interactions, the network remained significant, highlighting the quality of the data.

STRING also provided clues about the specific "biological processes" affected form the Gene Onthology (GO) enrichment analysis. Many proteins involved in making and processing messenger RNA (mRNA), the molecule used to build new proteins, were downregulated. This suggests a slowdown in protein production within the cells. However, other processes, like transporting molecules around the cell and breaking down energy sources, were also impacted, with the direction of change (up or down) depending on the specific function. More details about these processes are listed in the provided table 2.1.

Table 2.1. Selected biological processes altered in HF-MSS, based on Gene Ontology enrichment analysis.

Term ID [1]	Term Description [2]	Observed Gene Count [3]	Background Gene Count [4]	False Discovery Rate [5]
GO:0016071	mRNA metabolic process	83	667	2.5×10^{-21}
GO:0000398	mRNA splicing, via spliceosome	45	284	6.16×10^{-15}
GO:0006397	mRNA processing	54	456	2.70×10^{-13}
GO:1903311	regulation of mRNA metabolic process	36	238	1.89×10^{-11}
GO:0043488	regulation of mRNA stability	21	113	4.54×10^{-8}
GO:0050684	regulation of mRNA processing	18	114	4.33×10^{-6}
GO:0048024	regulation of mRNA splicing, via spliceosome	15	77	4.38×10^{-6}
GO:0006413	translational initiation	30	142	1.17×10^{-12}
GO:0006412	translation	44	362	3.99×10^{-11}
GO:0006417	regulation of translation	38	327	3.73×10^{-9}
GO:0002181	cytoplasmic translation	15	57	1.90×10^{-7}
GO:0006446	regulation of translational initiation	8	71	0.0246
GO:0006614	SRP-dependent cotranslational protein targeting to membrane	23	92	6.11×10^{-11}
GO:0016192	vesicle-mediated transport	139	1699	6.02×10^{-21}
GO:0060627	regulation of vesicle-mediated transport	30	480	0.0077
GO:0006892	post-Golgi vesicle-mediated transport	9	83	0.0197
GO:0055114	oxidation-reduction process	94	932	4.04×10^{-9}
GO:0015980	energy derivation by oxidation of organic compounds	17	217	0.0112
GO:0044281	small molecule metabolic process	134	1779	1.21×10^{-17}
GO:0062012	regulation of small molecule metabolic process	21	332	0.0272

[1] Unique seven-digit identifier prefixed by GO. [2] Textual description of the term. [3] Number of genes linked to that GO term in the input list. [4] Number of genes linked to a GO term in the entire background set. [5] Expected ratio of the number of false positive classifications (false discoveries) to the total number of positive classifications.

Table from "Proteomic Analysis of Marinesco–Sjögren Syndrome Fibroblasts Indicates Pro-Survival Metabolic Adaptation to SIL1 Loss". Potenza et al. https://doi.org/ 10.3390/ijms222212449

Among the "Molecular Function" of these proteins, we found that many were involved in RNA-binding (the instructions for making proteins), acting as enzymes called oxidoreductases, or binding to nucleotides (building blocks of DNA and RNA) (table 2.2.). Interestingly, while proteins involved in RNA-binding and the cytoskeleton generally decreased, other functions like nucleotide binding and oxidoreductase activity often increased. However, because some proteins were going up and others down, it's hard to say exactly what this means for the cell.

Next, we examined where these proteins are located within the cell (table 2.3.). Many proteins are found in organelles, like the endoplasmic reticulum, vesicles, and melanosomes. Some of these organelles, like melanosomes and vacuoles, were enriched in proteins that were going up, while others, like the actin cytoskeleton and ribonucleoprotein complex, were enriched in proteins that were going down. This suggests that the loss of SIL1 might be affecting protein production and degradation in different ways.

Overall, while this analysis provides some clues about how the loss of SIL1 might be affecting the cell, it is clear that more information is needed to fully understand the complex changes happening in HF-MSS.

Table 2.2. Selected molecular functions altered in HF-MSS, based on Gene Ontology enrichment analysis

Term ID [1]	Term Description [2]	Observed Gene Count [3]	Background Gene Count [4]	False Discovery Rate [5]
GO:0003723	RNA binding	86	850	2.57×10^{-17}
GO:0003729	mRNA binding	36	198	2.76×10^{-13}
GO:0003727	single-stranded RNA binding	13	80	0.00011
GO:0003725	double-stranded RNA binding	11	70	0.00058
GO:0019843	rRNA binding	10	60	0.00079
GO:0008135	translation factor activity, RNA binding	11	84	0.0021
GO:0000049	tRNA binding	8	56	0.0079
GO:0061980	regulatory RNA binding	5	34	0.0424
GO:0016491	oxidoreductase activity	75	716	8.70×10^{-16}
GO:0016860	intramolecular oxidoreductase activity	12	47	5.01×10^{-6}
GO:0000166	nucleotide binding	134	2097	2.45×10^{-12}
GO:0017076	purine nucleotide binding	108	1865	1.36×10^{-7}
GO:0030554	adenyl nucleotide binding	79	1524	0.00039
GO:0008092	cytoskeletal protein binding	71	882	4.82×10^{-10}
GO:0046961	proton-transporting ATPase activity, rotational mechanism	9	21	4.97×10^{-6}
GO:0008553	proton-exporting ATPase activity, phosphorylative mechanism	9	23	8.55×10^{-6}
GO:0015078	proton transmembrane transporter activity	12	120	0.0082
GO:0005178	integrin binding	19	122	2.30×10^{-6}
GO:0050839	cell adhesion molecule binding	24	200	3.68×10^{-6}
GO:0098634	cell-matrix adhesion mediator activity	3	7	0.0229

[1] Unique seven-digit identifier prefixed by GO. [2] Textual description of the term. [3] Number of genes linked to that GO term in the input list. [4] Number of genes linked to a GO term in the entire background set. [5] Expected ratio of the number of false positive classifications (false discoveries) to the total number of positive classifications.

Table from "Proteomic Analysis of Marinesco–Sjögren Syndrome Fibroblasts Indicates Pro-Survival Metabolic Adaptation to SIL1 Loss". Potenza et al. https://doi.org/ 10.3390/ijms222212449

Table 2.3. Selected cellular components altered in HF-MSS, based on Gene Ontology enrichment analysis.

Term ID [1]	Term Description [2]	Observed Gene Count [3]	Background Gene Count [4]	False Discovery Rate [5]
GO:0043226	organelle	566	12432	1.37×10^{-50}
GO:0043229	intracellular organelle	560	12193	3.30×10^{-50}
GO:0043227	membrane-bounded organelle	516	11244	1.07×10^{-37}
GO:0005783	endoplasmic reticulum	120	1796	9.40×10^{-13}
GO:0005788	endoplasmic reticulum lumen	30	299	1.86×10^{-6}
GO:0005793	endoplasmic reticulum-Golgi intermediate compartment	13	113	0.00095
GO:0031982	vesicle	173	2318	4.41×10^{-24}
GO:0031410	cytoplasmic vesicle	166	2226	6.49×10^{-23}
GO:0099503	secretory vesicle	96	948	1.62×10^{-20}
GO:0030139	endocytic vesicle	35	275	8.75×10^{-10}
GO:0045335	phagocytic vesicle	23	122	2.25×10^{-9}
GO:0042470	melanosome	35	105	1.55×10^{-20}
GO:1990904	ribonucleoprotein complex	89	770	2.33×10^{-22}
GO:0030532	small nuclear ribonucleoprotein complex	11	67	0.00021
GO:0005773	vacuole	74	682	4.05×10^{-17}
GO:0005775	vacuolar lumen	30	172	2.47×10^{-11}
GO:0005774	vacuolar membrane	31	311	1.36×10^{-6}
GO:0005764	lysosome	67	582	1.24×10^{-16}
GO:0015629	actin cytoskeleton	42	432	1.75×10^{-8}
GO:0032432	actin filament bundle	12	57	1.38×10^{-5}

[1] Unique seven-digit identifier prefixed by GO. [2] Textual description of the term. [3] Number of genes linked to that GO term in the input list. [4] Number of genes linked to a GO term in the entire background set. [5] Expected ratio of the number of false positive classifications (false discoveries) to the total number of positive classifications.

Table from "Proteomic Analysis of Marinesco–Sjögren Syndrome Fibroblasts Indicates Pro-Survival Metabolic Adaptation to SIL1 Loss". Potenza et al. https://doi.org/ 10.3390/ijms222212449

We next used the KEGG database to identify specific pathways that might be altered in this condition, and found that pathways involved in making, transporting, and translating mRNA were downregulated, suggesting that the cell was slowing down protein production (table 2.4.). However, pathways bindweed in breaking down proteins were upregulated, suggesting that the cell was focusing on clearing away unfolded proteins.
We found changes in metabolic pathways, including those responsible for the catabolism of fatty acids and energy production, Interestingly, the cell seemed to be producing more fatty acids for energy, but also using them to build up membranes. The pathways involved in making sugars and amino acids were also affected, with some enzymes going up and others going down. We can speculate that the cell was adjusting its metabolism to meet its changing needs.
Overall, these findings suggest that HF-MSS cells are undergoing significant changes in their protein production and metabolism. The cell appears to be reducing protein synthesis while increasing the breakdown of unfolded proteins. Additionally, the cell is adjusting its energy production and metabolism according to its needs.

Table 2.4. Selected altered pathways in HF-MSS, based on KEGG enrichment analysis

Term ID [1]	Term Description [2]	Observed Gene Count [3]	Background Gene Count [4]	False Discovery Rate [5]
hsa03040	spliceosome	26	130	3.14×10^{-10}
hsa03010	ribosome	21	130	3.48×10^{-7}
hsa03013	RNA transport	14	159	0.0074
hsa04145	phagosome	26	145	1.35×10^{-9}
hsa04142	lysosome	24	123	1.39×10^{-9}
hsa01100	metabolic pathways	99	1250	1.52×10^{-13}
hsa00020	citrate cycle (TCA cycle)	9	30	7.00×10^{-5}
hsa01212	fatty acid metabolism	10	48	0.00024
hsa01230	biosynthesis of amino acids	11	72	0.00075
hsa00010	glycolysis/Gluconeogenesis	10	68	0.0017
hsa00030	pentose phosphate pathway	5	30	0.0259

[1] Unique identifier for each KEGG object which takes the form of a prefix followed a five-digit number. [2] Textual description of the term.
[3] Number of genes linked to that KEGG term in the input list. [4] Number of genes linked to a KEGG term in the entire background set.
[5] Expected ratio of the number of false positive classifications (false discoveries) to the total number of positive classifications.

Table from "Proteomic Analysis of Marinesco–Sjögren Syndrome Fibroblasts Indicates Pro-Survival Metabolic Adaptation to SIL1 Loss". Potenza et al. https://doi.org/ 10.3390/ijms222212449

In order to get a broader view of the pathways affected by the loss of SIL1, we took advantage of another tool called Ingenuity Pathway Analysis from QIAGEN. IPA identified a large number of pathways that were disrupted, which is consistent with previous studies (table 2.5.). Some of these pathways, like phagosome, fatty acid metabolism, and TCA cycle, were also identified using KEGG. Additionally, IPA found evidence of mitochondrial

dysfunction and defects within protein synthesis, which could be in line with the activation of the PERK pathway.

As resumed in table 2.6., IPA also predicted that HF-MSS cells might have increased phagocytosis (a process of engulfing and destroying foreign particles), fatty acid metabolism, and cell death. On the other hand, DNA repair mechanisms and cell cycle progression were predicted to be decreased. Surprisingly, IPA initially predicted a decrease in movement disorders and neurodegeneration. However, upon closer examination, we realized that this was likely due to the increased activity of lysosomal enzymes, which are often downregulated in neurodegenerative diseases[25].

Table 2.5. Selected canonical pathways altered in HF-MSS, based on Ingenuity Pathway Analysis

Ingenuity Canonical Pathway [1]	−log (*p*-Value) [2]	z-Score [3]
phagosome maturation	14.6	
EIF2 signaling	14	−2.357
caveolar-mediated endocytosis signaling	7.97	
fatty acid β-oxidation I	7.88	2.53
TCA cycle II (Eukaryotic)	6.89	2.121
isoleucine degradation I	6.83	2.236
mitochondrial dysfunction	6.78	
valine degradation I	4.99	2.236
tryptophan degradation III (Eukaryotic)	4.49	1.342
spliceosomal cycle	3.51	−2.646
tRNA charging	2.43	−1.342

[1] Textual description of the term. [2] Negative logarithm of *p*-value. [3] Also called standard score, is the number of standard deviations by which the value of a raw score is above or below the mean value of what is being observed or measured.

Table from "Proteomic Analysis of Marinesco–Sjögren Syndrome Fibroblasts Indicates Pro-Survival Metabolic Adaptation to SIL1 Loss". Potenza et al. https://doi.org/ 10.3390/ijms222212449

Table 2.6. Selected disease or functions that are predicted to be increased or decreased on the basis of differential proteins in HF-MSS, based on Ingenuity Pathway Analysis.

Disease or Functions Annotation [1]	*p*-Value	z-Score [2]	Predicted Activation State [3]
fatty acid metabolism	4.57×10^{-12}	2.017	Increased
cellular homeostasis	5.29×10^{-11}	2.129	Increased
cell death of tumor cell lines	8.41×10^{-24}	2.15	Increased
endocytosis by eukaryotic cells	5.24×10^{-11}	2.311	Increased
metabolism of glycosphingolipid	0.00000134	2.387	Increased
cell death of tumor cells	1.13×10^{-13}	2.416	Increased
sensitivity of cells	0.000000386	2.56	Increased
phagocytosis	3.93×10^{-8}	2.708	Increased
phagocytosis of cells	0.000000438	2.714	Increased
degradation of extracellular matrix	7.31×10^{-8}	2.905	Increased
cell death of cancer cells	1.17×10^{-10}	2.995	Increased
cell death of osteosarcoma cells	1.76×10^{-12}	3.545	Increased
homologous recombination	9.48×10^{-9}	−3.637	Decreased
accumulation of lipid	2.49×10^{-9}	−3.636	Decreased
homologous recombination of cells	5.85×10^{-9}	−3.499	Decreased
glucose metabolism disorder	0.00000102	−3.279	Decreased
DNA recombination	6.51×10^{-9}	−3.235	Decreased
motor dysfunction or movement disorder	1.01×10^{-18}	−2.934	Decreased
movement Disorders	9.11×10^{-19}	−2.666	Decreased
lysosomal storage disease	2.68×10^{-10}	−2.591	Decreased
repair of DNA	0.000000166	−2.545	Decreased
cell death of breast cancer cell lines	9.12×10^{-8}	−2.374	Decreased
astrocytosis	0.00000147	−2.219	Decreased
degeneration of central nervous system	8.66×10^{-9}	−2.218	Decreased
neurodegeneration	0.000000465	−2.185	Decreased
degeneration of nervous system	0.000000827	−2.128	Decreased
amyloidosis	7.3×10^{-13}	−2.08	Decreased
degeneration of brain	1.46×10^{-8}	−2.032	Decreased

[1] Textual description of the term. [2] Also called standard score, is the number of standard deviations by which the value of a raw score is above or below the mean value of what is being observed or measured. [3] Prediction based on the observed gene expression changes in the dataset.

Table from "Proteomic Analysis of Marinesco–Sjögren Syndrome Fibroblasts Indicates Pro-Survival Metabolic Adaptation to SIL1 Loss". Potenza et al. https://doi.org/ 10.3390/ijms222212449

We then validated some proteomics findings by examining the expression of specific proteins using immunofluorescence and Western blotting. These experiments confirmed that proteins involved in RNA processing and translation were significantly downregulated in HF-MSS cells. For example, nucleolin and nucleophosmin, two proteins important for ribosome production, were barely detectable in many HF-MSS cells.
Additionally, chaperones and lysosomal proteins were upregulated in HF-MSS. Chaperones help to fold proteins correctly, while lysosomal proteins break down damaged proteins. Immunofluorescence analysis showed that in HF-MSS cells, the endoplasmic reticulum (ER), was misshapen and enlarged, and contained high levels of chaperones. Interestingly, about 30% of HF-MSS cells were significantly larger than normal cells. These larger cells showed the most severe abnormalities, such as low levels of nucleolin and nucleophosmin and high levels of chaperones (Figure 2.5. A and 2.6. A). This suggests that the enlarged cell size may be a part of the pathological phenotype in HF-MSS.

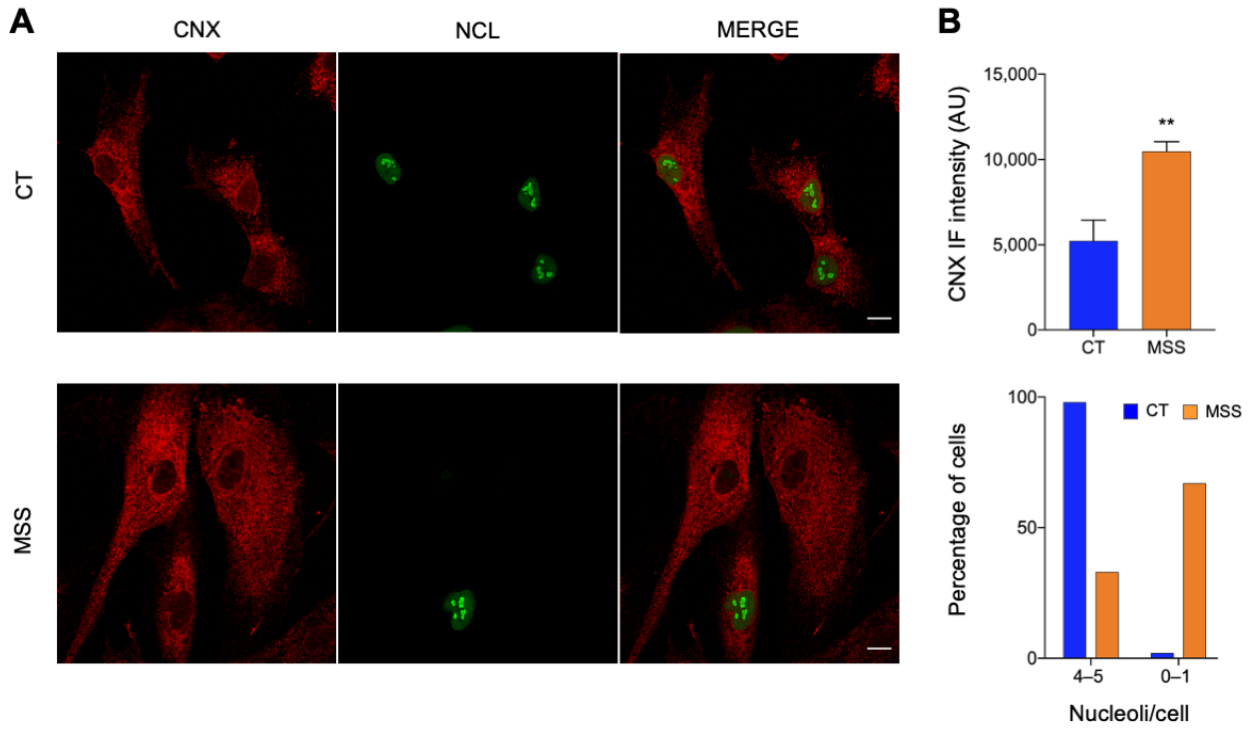


Figure 2.5. Fluorescence microscopy of representative DE proteins. (A) HF-CT (CT) and HF-MSS (MSS) were plated on glass coverslips, fixed in PFA 4%, and processed for immunofluorescence. Confocal images of cells stained for CNX (red) and NCL (green) are shown. The merge of green and red channels is shown in the third panel. Scale bar: 20 μm. (B) Quantification of total CNX staining and the number of NCL-positive nucleoli/cell of the experiment shown in A. Blue and red bars indicate HF-CT and HF-MSS, respectively. ** $p < 0.01$.

From "*Proteomic Analysis of Marinesco–Sjögren Syndrome Fibroblasts Indicates Pro-Survival Metabolic Adaptation to SIL1 Loss*". Potenza et al. https://doi.org/ 10.3390/ijms222212449

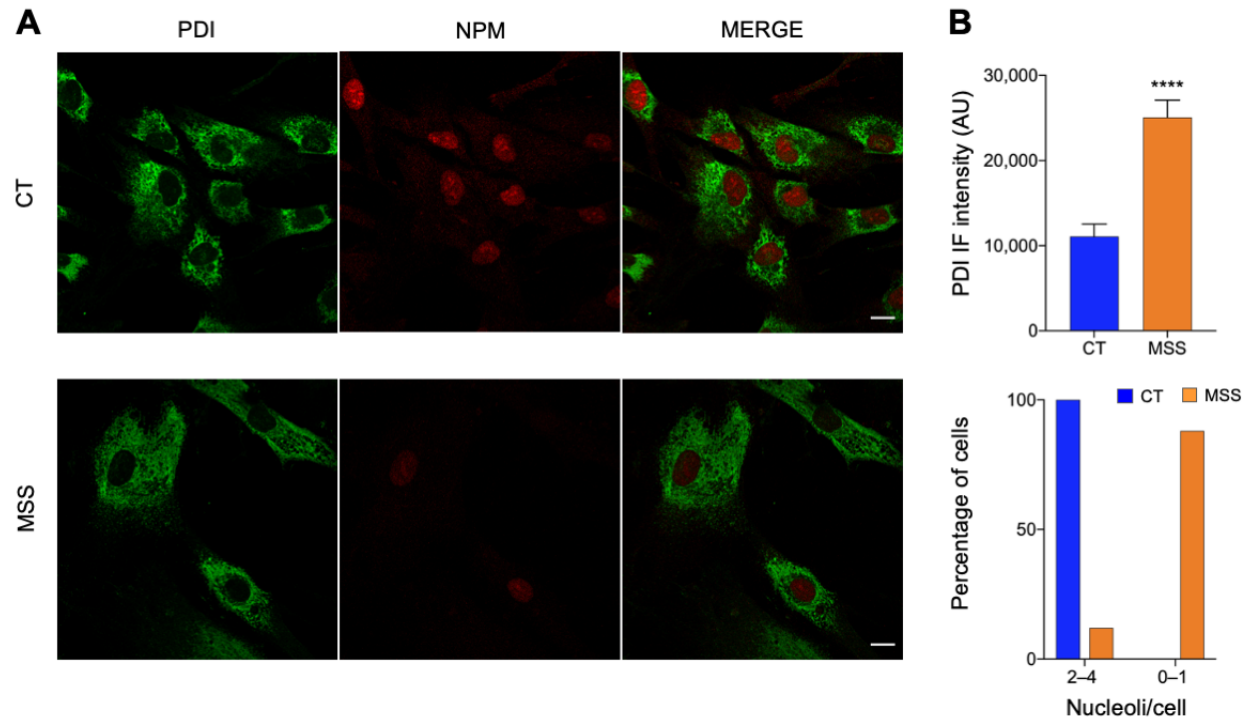


Figure 2.6. Fluorescence microscopy validation of proteomic analysis. (A) HF-CT (CT) and HF-MSS (MSS) were plated on glass coverslips, fixed in PFA 4%, and processed for immunofluorescence. Confocal images of cells stained for PDI (green) and NPM (red) are shown. The merge of green and red signal is also shown. Scale bar: 20 μm. (B) Quantification of total PDI staining and the number of NPM-positive nucleoli/cell of the experiment shown in A. Blue and red bars indicate HF-CT and HF-MSS, respectively. **** $p < 0.0001$.

From "*Proteomic Analysis of Marinesco–Sjögren Syndrome Fibroblasts Indicates Pro-Survival Metabolic Adaptation to SIL1 Loss".* Potenza et al. https://doi.org/ 10.3390/ijms222212449

We further confirmed the proteomics findings using Western blotting, which showed that nucleolin, nucleophosmin, and nestin were significantly downregulated in HF-MSS cells. Additionally, caveolin-1, annexin-V, and collagen triple helix repeat containing 1 were upregulated, as previously observed in the proteomics data (Figure 2.7. A and B). Overall, these complementary approaches validated the changes in protein expression identified by proteomics. Finally, based on the downregulation of ribosome and RNA splicing machinery, and the predictions from IPA, we investigated the proliferation rate of HF-MSS cells, and found that these cells grew significantly slower than control cells, suggesting that the reduced protein synthesis may be affecting cell growth.

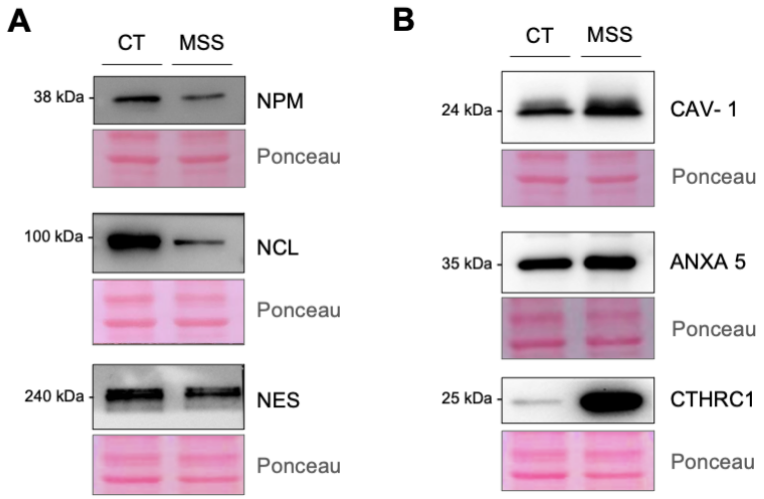


Figure 2.7. Western blot validation of proteomic analysis. (A,B) HF-CT (CT) and HF-MSS (MSS) cultured under standard growth conditions were analyzed by Western blotting to assess the expression of NPM, NCL, NES, CAV-1, ANXA-5, and CTHRC1 as indicated. The proteins downregulated or upregulated in HF-MSS are shown in A and B, respectively. Immunoblots are representative of at least two independent experiments. Ponceau S staining of the blots is shown to control for equal protein loading.

From "*Proteomic Analysis of Marinesco–Sjögren Syndrome Fibroblasts Indicates Pro-Survival Metabolic Adaptation to SIL1 Loss".* Potenza et al. https://doi.org/ 10.3390/ijms222212449

Discussion

The study investigates the effects of SIL1 deficiency, a condition associated with muscle and cerebellar degeneration, on MSS patient skin fibroblasts . Despite SIL1's widespread expression, most organs remain unaffected in this condition. Previous research suggested that ORP150 might compensate for SIL1 loss[13].

This study found no increase in ORP150 but observed heightened ER stress markers, reduced protein synthesis, and increased degradation processes, indicating a kind of unfolded protein response activation. Additionally, significant changes in signaling and metabolic pathways were detected, potentially contributing to cell survival.

The findings suggest that unaffected cells exhibit a mild unfolded protein response and increased endolysosome activity, despite lacking connective tissue problems. Proteomic analysis revealed downregulation of RNA splicing and transport machinery, ribosomes, and translation initiation. These changes might be attributed to reduced protein synthesis due to the unfolded protein response, but the spliceosome downregulation is unexpected and linked to cancer cell survival and fibroblast senescence[26,27].

HF-MSS cells also exhibited metabolic changes, including increased fatty acid and amino acid catabolism, TCA cycle activation, and mitochondrial ATP synthase upregulation. These changes support increased ATP demand in the ER for ion homeostasis and folding activity[28]. The study also suggets the importance of ER-mitochondria contacts in maintaining ATP coupling and found increased mitofusin-2 expression[29].

Overall, the results suggest that HF-MSS cells undergo metabolic adaptations to survive SIL1 deficiency, highlighting the intricate interplay between ER stress, metabolism, and cell survival.

Materials and methods

Reagents

The following antibodies were used for WB and/or IF as indicated: SIL1 (Proteintech #24110-1-AP); ATF4 (Cell Signaling #11815); ATF6B (Proteintech #15794-1-AP); EIF2α (Santa Cruz #sc-11386); pho-EIf2α (Cell Signaling #3597s); PDI (Assay Design #SPA-891); BiP (BD #610979); ORP150 (Abcam #EP5891); LC3B (Cell Signaling #2775); NCL

(Cell Signaling #87792S); NPM (Cell Signaling #3542S); CTHRC1 (Abcam #ab85739); Anti SQSTM1 (BD Bioscience #610833); LAMP1 (Abcam #ab25630); CNX (Cell Signaling #2679S); NES (Millipore #AB5922); CAV-1 (Cell Signaling #3238); and GAPDH (Santa Cruz #sc-32233). Hoechst #33342 from Life Technology was used to counterstain nuclei. For PCR amplification of the spliced and unspliced form of human XBP1, the following primers were used: FW 5′-AGCTCAGACTGCCAGAGATCG-3′; REV 5′-AATCCATGGGGAGATGTTCTA-3′ [30].
Powders, buffers, and other commonly used reagents were supplied by Sigma unless otherwise noted and were of analytical grade or higher.

Cell Culture

Primary Human Dermal Fibroblast (NDHF Promo Cell #FB60C12350) supplied by Carlo Erba were used as the control cell line and compared with primary dermal fibroblast from a young Marinesco–Sjögren syndrome patient, supplied by Telethon Network of Genetic Biobanks—TNGB [31]. Cells were cultured in Dulbecco's modified Eagle's medium + GlutaMAX (GIBCO, 61965-026), supplemented with 10% of Fetal Bovine Serum (FBS) and 1% penicillin/streptomycin PenStrep (GIBCO #15070-063). Cells were maintained at 37°C, 5% CO2, and detached by Trypsin-EDTA 0.5% (GIBCO #15400-054).

Fluorescence Immunostaining and Confocal Microscopy

Cells were plated on cover slips to 70% density and the day after fixed in 4% paraformaldehyde (Electron Microscopy Science) for 10 min at room temperature. Cells were subsequently incubated for non-specific site blocking and permeabilization in blocking solution [0.05% saponin, 0.5% BSA, and 50 mM NH4Cl in PBS] for 30 min at room temperature. Primary antibody incubation was performed overnight at 4°C. The day after, fluorescent Alexa Fluor-conjugated anti-IgG secondary antibody was incubated for 40 min at room temperature together with Hoechst, in order to counterstain nuclei. Signal was than detected with a confocal microscope (Zeiss LSM 800) and images were post-processed and analyzed by Zen 2.3 software (Zeiss, Jena, Germany). The total immunofluorescence intensity of the signals was measured by ImageJ software (National Institutes of Health, Bethesda, MD, USA). The total immunofluorescence intensity was

then normalized for cell number. All experiments were carried out at least two times. The results are shown as arbitrary units (AU).

Western Blot Analysis and PCR

Cells were lysed in RIPA buffer [50 mM tris HCl (pH 7.6), 140 mM NaCl, 5 mM EDTA, 0.1% SDS, 1% NP40, 100 mM NaF, 0.1% Sodium deoxycholate] supplemented with protease (cOmpleteTM Tablets, Roche) and phosphatase (PhosSTOP tablets, Roche) inhibitors. Protein concentration was assessed by Bradford protein assay (Bio-Rad). Equal amounts of proteins were than resuspended in 4x Laemmli buffer [15% b-mercaptoethanol, 0.25 M Tris-HCl pH 6.8, 40% Glycerol, 8% SDS, 0.02% Blu Bromophenol], separated by SDS-PAGE, and transferred onto nitrocellulose membrane. The presence of proteins on the nitrocellulose membranes and their quantity was assessed by Ponceau S staining [0.5% (w/v) Ponceau S dissolved in 1% (v/v) acetic acid]. Membranes were incubated for 5 min in Ponceau S solution and then washed once with water, photographed, and destained with TBST. Ponceau S staining was used as a Western blotting multiprotein loading control throughout the manuscript instead of a single protein (e.g., β-actin), whose expression might be altered in HF-MSS cells. Filters were then blocked for 1 h at room temperature with either 5% non-fat dried milk or 5% BSA, and incubated with the primary antibodies overnight at 4°C. Secondary antibodies α-rabbit and α-mouse were applied the day after for 1 h at room temperature and signal was detected by GE Amersham ECL. For PCR analysis of XBP1 splicing[30], RNA was extracted from cells by a miRneasy kit (QIAGEN cat. 217004). cDNA was then obtained using a reverse transcription amplification kit (Applied Biosystem) and PCR was run using 54°C as the compromise annealing temperature for a total of 40 cycles. 10 µL of amplificated products was separated on a 3% agarose gel.

Proliferation Assay

Cell proliferation was monitored using a Click-iT Edu Proliferation assay kit (#C10499, Invitrogen). About 10,000 cells/well were plated in a 96-well plate the day before the experiment, and the manufacturing instructions were followed.

Label-Free Proteomics Analysis

HF-MSS cells were grown to subconfluency, incubated in serum-free medium for 24 h, washed, lysed in proteomic buffer [UREA 6 M, Tris Base 100 mM, CHAPS 2%, Triton X 1%, DTT 50 mM], and treated by the Filter Aided Sample Preparation (FASP) method. Protein concentration was evaluated through Bradford assay (Bio-Rad, Hercules, CA, USA) in order to digest 25 µg of protein by trypsin (Sigma-Aldrich, St. Louis, MO, USA). For protein label-free identification and quantification, tryptic peptides from each sample were analyzed in triplicate with LC-MS/MS using the UltiMateTM 3000 UPLC (Thermo Fisher Scientific, Waltham, MA, USA) chromatographic system coupled to the Orbitrap FusionTM TribridTM (Thermo Fisher Scientific) mass spectrometer. Peptides were loaded on the Trap Cartridge C18 (0.3 mm ID, 5 mm L, 5 µm PS, Thermo Fisher Scientific) and then separated on an EASY-spray AcclaimTM PepMapTM C18 (75 µm ID, 25 cm L, 2 µm PS, Thermo Fisher Scientific) nanoscale chromatographic column. The mobile phase A was 0.1% formic acid in H2O and the mobile phase B was 0.1% formic acid in acetonitrile. The flow rate was set at 300 nL/min, with a total run time of 125 min using a chromatographic gradient from 2% to 90% of phase B. Proteomics data were acquired in positive-ion polarity with Data Dependent Acquisition (DDA) mode to trigger precursor isolation and MS2 sequence using N2 as the collision gas for HCD fragmentation. The positive ion voltage was set at 1700 V and the ion transfer tube at 275°C for desolvation. MS1 scans were performed in the Orbitrap analyzer covering an m/z range of 375–1500 with a resolution of 240,000. A standard automatic gain control (AGC) target and an automatic maximum injection time (MIT) were used. The signal intensity threshold was set to 1.0×10^4 and the MS2 spectra were acquired using a Top Speed method of 3s. In particular, precursor ions with charges of +2 to +5 were used for MS2 sequencing and scanned in the ion trap by setting the following parameters: MS2 isolation window of 1.6 Da, AGC target of 1.0×10^4, dynamic exclusion time of 60 s, and mass tolerance of ±10 ppm were used covering an m/z range of 300–1200. We performed a HCD fragmentation with a fixed collision energy of 30% and a MIT of 70 ms. The mass spectrometry proteomics data were deposited to the ProteomeXchange Consortium via the PRIDE partner repository with the dataset identifier PXD029086.

Proteomics Data Processing

Proteomics raw data were processed using a free computational platform, MaxQuant version 1.6.6.0 (Max-Planck Institute for Biochemistry, Martinsried, Germany). Peak lists, generated in MaxQuant, were searched using Andromeda peptide search engine against the UniProt database (released 2018_04, taxonomy Homo sapiens, 20,874 entries) supplemented with frequently observed contaminants and containing forward and reverse sequences. As reported previously [32,33], carbamidomethylation of cysteines (C) was defined as fixed modification, while oxidation of methionines (M) and deamidation of asparagines (N) and glutamines (Q) were set as variable modifications. The false discovery rate (FDR) both at the protein level and at the peptide level was set at 1%. LFQ Intensity was used to quantify the protein abundance in each sample [40]. Bioinformatics analysis was performed with Perseus version 1.6.10.50 (Max-Planck Institute for Biochemistry, Martinsried, Germany). LFQ intensities were log2 transformed to facilitate the calculation of the protein expression. Site only and reverse and contaminant peptides were removed from the dataset. The minimum number of valid values accepted was set to 2 in at least one group. In this way, we evaluated not only the different protein expression, but also the presence or absence of proteins between the two conditions. Moreover, a univariate statistical analysis was performed with a p-value threshold of 0.05 in order to define the significantly different proteins between HF-MSS cells and HF-CT through Volcano Plot visualization (FDR = 0.01 and S0 = 0.05). Finally, a selection of significantly modulated proteins (p-value < 0.05) was loaded into the Ingenuity Pathway Analysis tool (IPA, Qiagen, Hilden, Germany) and subjected to a Core Analysis. IPA maps the modulated proteins on the basis of their functional annotations on Gene Ontology and proprietary databases to identify enriched Canonical
Pathways and Disease or Functions. Furthermore, it is possible to infer about the possible upregulation or downregulation of the pathway, disease, or function if the calculated z-score is ≥ 2.00 or ≤ −2.00 respectively.

Electron Microscopy (EM)

Approximately 2×10^6 HF cells cultured in monolayers were prepared for EM as follows. Cells were detached from the dish with trypsin, centrifuged at 180× g for 2.5 min, washed 3 times with PBS at 37 °C, fixed with 3.5% glutaraldehyde in 0.1 M sodium cacodylate

buffer (NaCaCO) for 1h, and stored at 4°C. For embedding, cells were postfixed in 2% OsO4 in the same buffer for 2 h and block-stained in saturated uranyl acetate replacement. After dehydration, specimens were embedded in epoxy resin (Epon 812). Ultrathin sections were cut using a Leica Ultracut R microtome (Leica Microsystem, Austria) with a Diatome knife (DiatomeLtd. CH-2501 Biel, Switzerland) and double-stained with uranyl acetate replacement and lead citrate. Sections were viewed and photographed in a Morgagni Series 268D electron microscope (FEI Company, Brno, Czech Republic) equipped with a Megaview III digital camera and Analy-SIS software (Olympus Soft Imaging Solutions). Quantitative analysis was done on random micrographs of HF cell cultures (CT and MSS). The percentage of cells with cytoplasmic accumulation of vacuoles delimited by membranes and containing electron-dense material was determined in micrographs taken at either 5600 or 7100 of magnification (sample size: 100 cells/group).

3 CRISPR-Cas9 C2C12 SIL1 clone generation

Unpublished data

Rationale

Marinesco-Sjögren syndrome is a rare genetic disorder affecting approximately one in a million people[1]. This rarity makes it challenging to obtain cells from multiple patients for comparative studies. Moreover, the primary cell types affected by the disease, Purkinje neurons and skeletal muscle cells, pose additional challenges. Purkinje neurons are inaccessible for sampling, and obtaining skeletal muscle cells requires invasive muscle biopsies.

To overcome these limitations and establish a reliable in vitro model for studying Marinesco-Sjögren syndrome, we propose using CRISPR/Cas9 technology to introduce specific genetic modifications into a commercially available murine muscle cell line. This approach offers a non-invasive method to generate a stable and representative cellular model of the disease, facilitating in-depth investigations into its underlying mechanisms and potential therapeutic interventions.

C2C12 is an immortalized mouse myoblast cell line, widely used in biomedical research to study muscle cell differentiation, myogenesis, and the effects of various factors on muscle cell behavior[34]. C2C12 cells exhibit a remarkable capacity for both proliferation and differentiation. Under high serum conditions, they rapidly proliferate, while low serum conditions induce differentiation into myotubes. These multinucleated myotubes represent the component of contractile skeletal muscle fibers, making C2C12 cells ideal for studying muscle tissue *in vitro*[35].

CRISPR-Cas9 (Clustered Regularly Interspaced Short Palindromic Repeats) is a revolutionary gene editing technique that allows precise modification of genomes (Figure 3.1). By utilizing a simplified version of the bacterial CRISPR-Cas9 immune system, it is possible to introduce specific genetic alterations into living organisms. This is achieved by delivering a Cas9 enzyme complexed with a guide RNA (gRNA) into a cell. The gRNA directs the Cas9 enzyme to a specific DNA sequence, where it cuts the DNA double strand. This precise cut enables the removal or insertion of genetic material, leading to targeted genome editing[36].

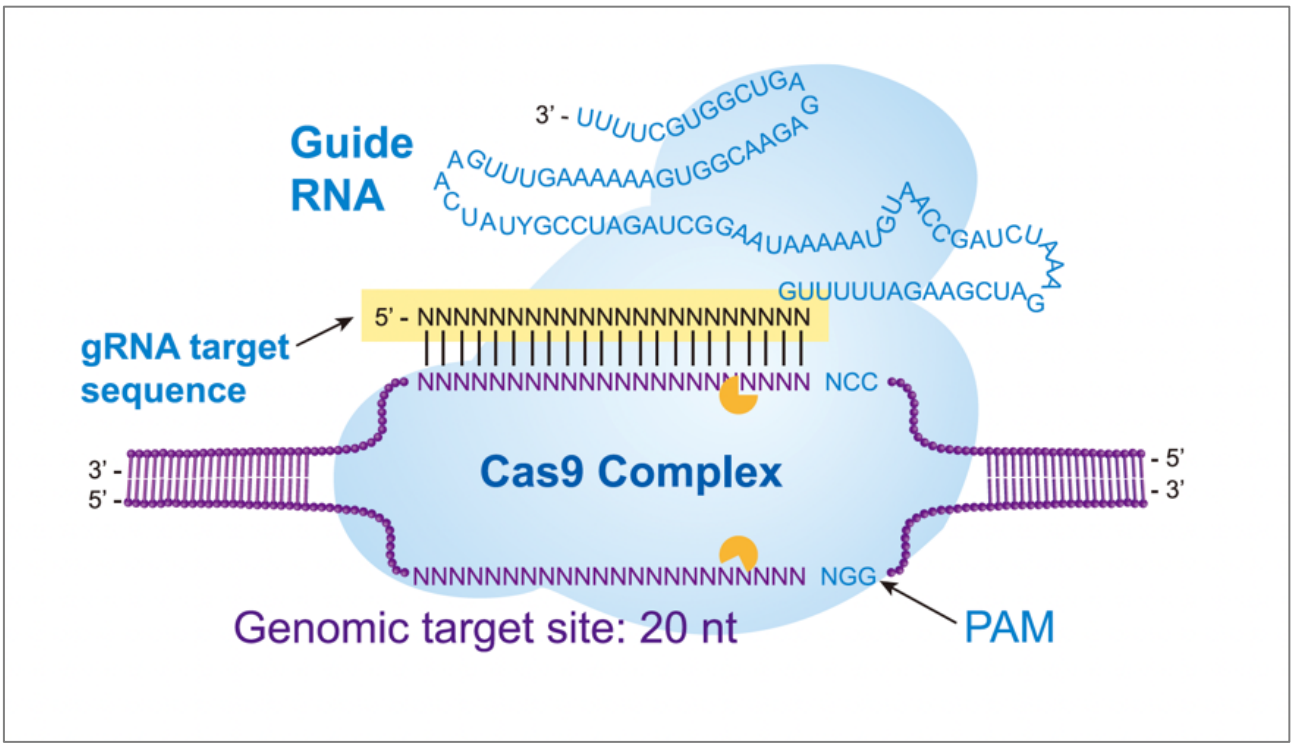


Figure 3.1. Cartoon of the Cas9 complex
From Genescript CRISPR Handbook

Objective: Employing CRISPR/Cas9 technology to generate a stable, immortalized C2C12 myoblast cell line with a targeted deletion of the SIL1 gene.

Results

The C2C12 mouse cell line is a valuable model system for studying muscle biology and disease. These myoblasts exhibit robust proliferation and can be induced to differentiate into myotubes by manipulating the culture conditions, specifically by lowering serum concentrations. This controlled differentiation process allows us to observe the intricate steps involved in muscle cell development, from precursor cells to mature muscle fibers components.

By studying this process, we can gain insights into the role of specific genes and proteins, such as SIL1, in muscle development and repair. For instance, we can investigate how the absence of SIL1 might affect myogenesis and potentially lead to muscle dysfunction. Myogenesis, the formation of muscle tissue, occurs during both embryonic development and adult muscle regeneration[37]. In adults, muscle repair involves the activation of quiescent satellite cells, which are muscle stem cells located beneath the basal lamina of

muscle fibers. Upon activation, satellite cells proliferate and differentiate into myoblasts. Under specific conditions and with the help of regulatory factors, myoblasts differentiate, changing their shape into myocytes. These cells fuse together to create elongated, multinucleated myotubes capable of contraction. Finally, these myotubes align to form muscle fibers[37].

Hence, we knocked out SIL1 in C2C12 cells using the CRISPR/Cas9 technology, and resulting clones were characterized at both the myoblast and myotube stages to investigate any alterations in pathways implicated in Marinesco-Sjögren syndrome during the differentiation process.

First experiments aimed at evaluating the molecular markers usually altered in MSS. Western blotting and immunofluorescence analysis were used to assess the expression of molecular chaperones, endoplasmic reticulum proteins (GRP78, PDI, HSP47, ORP150), and proteins involved in the unfolded protein response (UPR) and protein synthesis (p-eIF2α, p-PERK, ATF4, ATF6β, p-IRE1α).

Surprisingly, as shown in the summary in Figure 3.2. and 3.3 panel (b), no consistent changes in the expression of these markers were observed in either myoblasts or myotubes lacking SIL1 compared to wild-type cells.

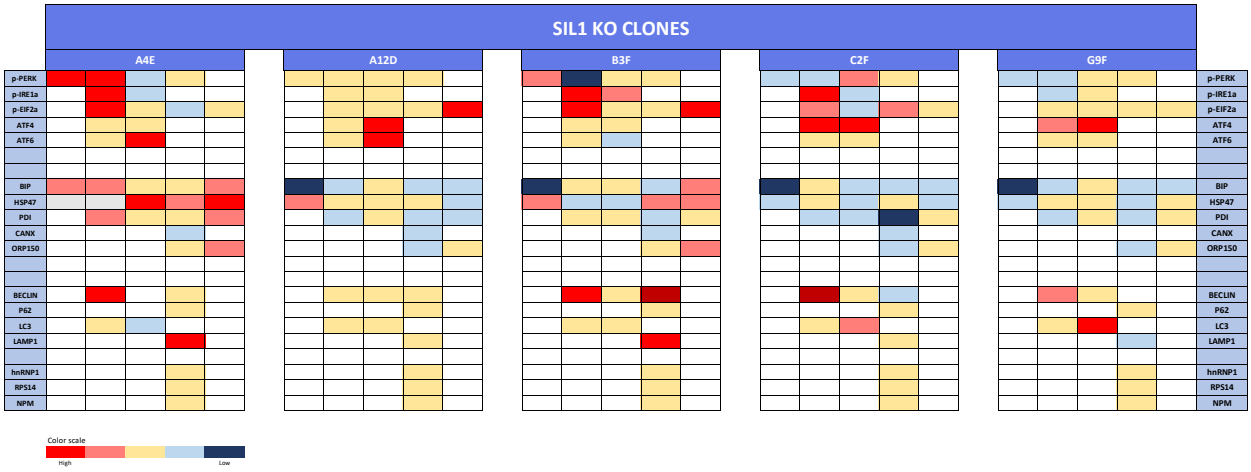


Figure 3.2. Heatmap summary of WB results. According to a color scale, the heatmap displays the expression levels of the molecular markers listed on the table's sides for each of the five KO myoblast clones. Colored rectangles indicate whether a protein in a specific clone has higher (red), equal (yellow), or lower (blue) expression compared to WT myoblasts. Each column represents a single experiment.

Additionally, as clear in Figure 3.3 panel (c), their proliferation rate was not significantly different from that of WT C2C12 cells.

The most evident difference between the C2C12 KO and WT cells was instead observed in the differentiation process. While WT myoblasts readily differentiate into myotubes in

low-serum medium, C2C12 KO cells displayed constant aberrant differentiation phenotypes. Some clones failed to differentiate altogether, while others formed atypical myotubes. Notably, each of the five KO clones exhibited a unique differentiation phenotype, suggesting a complex and variable impact of SIL1 deficiency on myogenesis (Figure 3.3 panel (a)).

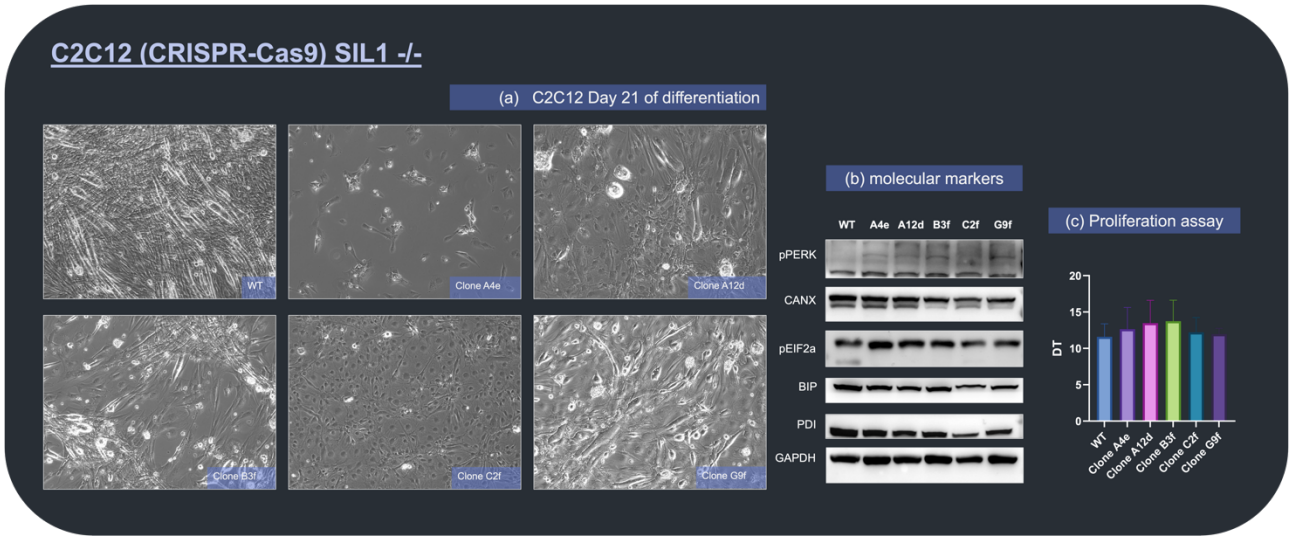


Figure 3.3. CRISPR KO clones characterization. Panel (a) brightfield microscopy images showing the cellular differentiation state after 21 days of culturing in differentiation medium. Panel (b) visualizes protein levels analyzed by Western blot (WB) in KO clones at the myoblast stage. The bar graph in Panel (c) represents the proliferation rate of myoblasts, calculated via trypan blue exclusion assay and doubling time (DT).

From *"Generating an in vitro model for the study of Marinesco- Sjögren syndrome"*. Potenza et al. FEBS Poster

Discussion

The five generated SIL1 knockout clones did not exhibit the typical alterations in marker expression associated with Marinesco-Sjögren syndrome. Furthermore, the expression levels of these markers displayed significant variability, both between the experiments and within individual clones. This variability suggests a complex interplay of factors influencing the expression of these markers, which may not be fully captured by the SIL1 knockout alone.

While the inability to differentiate from myoblasts to myotubes was a consistent phenotype across experimental replicates, the specific manifestation of this defect varied significantly between clones. However variability between clonal populations is a known issue in *in vitro* experiments, we are taking additional steps to confirm that the observed lack of or

abnormal differentiation in these 5 specific populations is directly linked to the SIL1 knockout. In collaboration with a research group in Milan, we are reintroducing SIL1 into the CRISPR clones. By observing whether this reintroduction restores the wild-type phenotype, we aim to establish a definitive causal relationship between the SIL1 knockout and the observed cellular behavior.

At the same time, inconsistent results and the diverse clonal responses hinder the interpretation of the overall phenotype and raise doubts about the model's suitability for representing Marinesco-Sjögren syndrome, requiring a different model to be evaluated.

Materials and Methods

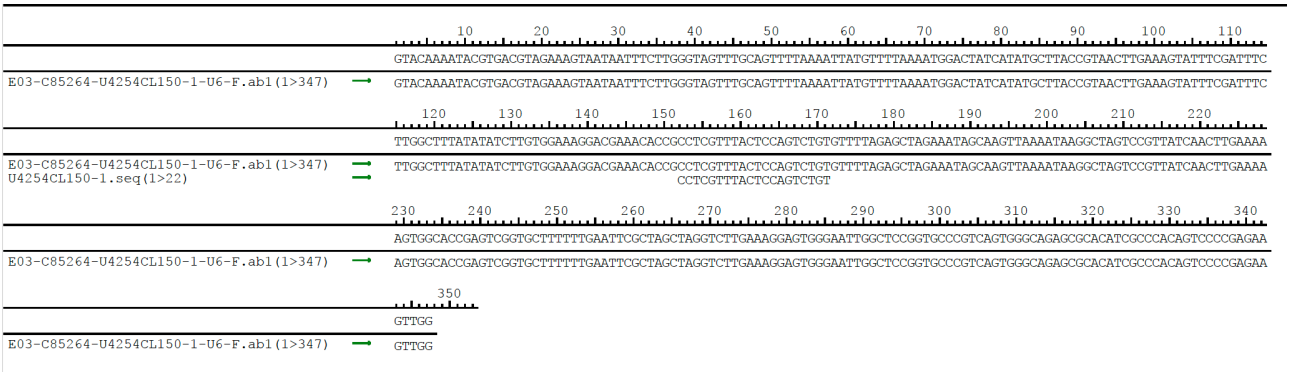
Cell culture

C2C12 cell line from ATCC were cultured in DMEM Glutamax (GIBCO #61965-026) supplemented with FBS and PenStrep (GIBCO #15140122). In detail, to keep C2C12 at the myoblast stage, medium was supplemented with 20% FBS and cells were not allowed to reach high density. In order to get myotube differentiation, medium was instead supplemented with 5% Horse Serum (GIBCO #26050) once cells reached 100% density.

CRISPR/CAS9 Knockout

C2C12 cells were transfected with the pLentiCRISPR v2 plasmid using LIPO3000 reagent (Invitrogen #L3000-008).

mouse SIL1 CRISPR Guide RNA sequence:



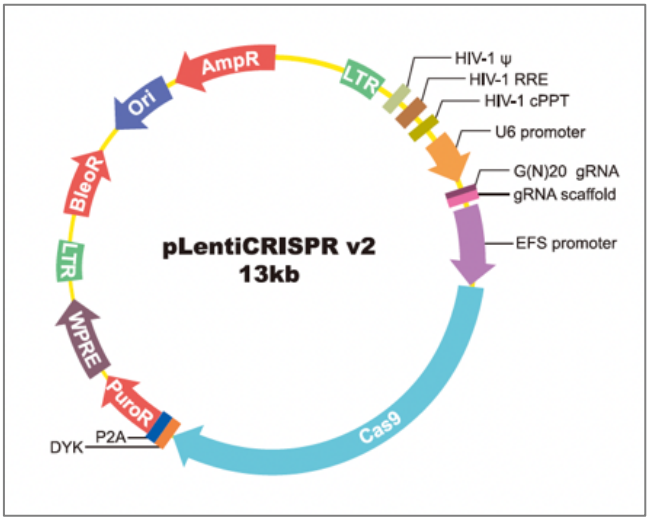


Figure 3.4. Cartoon of the CRIPR plasmid
From Genescript CRISPR Handbook

Subsequently, puromycin selection (2ug/ul puromycin 24h treatment) was used to isolate only successfully transfected cells. After approximately ten days of selection, limiting dilutions were applied to obtain single-cell clones.
Approximately 40 clones were isolated, expanded, and screened for SIL1 protein expression levels using Western blotting. From this analysis, 17 clones exhibiting low levels or no SIL1 expression were selected for Sanger sequencing (Outsource). Ultimately, only 5 clones were found to harbor homozygous mutations, resulting in complete loss of SIL1 protein expression. Nine clones carried heterozygous mutations, while the remaining 3 clones showed no detectable mutations.

Western Blot Analysis

Cells were lysed in RIPA buffer [50 mM tris HCl (pH 7.6), 140 mM NaCl, 5 mM EDTA, 0.1% SDS, 1% NP40, 100 mM NaF, 0.1% Sodium deoxycholate] supplemented with protease (cOmpleteTM Tablets, Roche) and phosphatase (PhosSTOP tablets, Roche) inhibitors. Protein concentration was assessed by Bradford protein assay (Bio-Rad). Equal amounts of proteins were than resuspended in 4x Laemmli buffer [15% b-mercaptoethanol, 0.25 M Tris-HCl pH 6.8, 40% Glycerol, 8% SDS, 0.02% Blu Bromophenol], separated by SDS-PAGE, and transferred onto nitrocellulose membrane. The presence of proteins on the nitrocellulose membranes and their quantity was assessed by Ponceau S staining [0.5% (w/v) Ponceau S dissolved in 1% (v/v) acetic acid]. Filters were then blocked for 1 h at room temperature with either 5% non-fat dried milk or 5% BSA, and incubated with the primary antibodies overnight at 4 °C. Secondary

antibodies α-rabbit and α-mouse were applied the day after for 1 h at room temperature and signal was detected by GE Amersham ECL.

List of primary antibodies used:

ATF4 Cell Signaling #11815
ATF6B Proteintech #15794-1-AP
Phospho-eIF2a (Ser51) Cell Signaling #3597S
PERK Abcam #ab65142
Calnexin Cell signaling #2679S
p-IRE1alpha (pSer725) Thermo scientific #PA1-16-927
Bip/GRP78 BDbioscience #610979
PDI Enzo lifescience #ENSPA891F
HSP47 Novusbio #NBP1-88172
Beclin1 Novusbio #NB500-249
ORP 150 Abcam #ab134944
LC3B Cell Signaling #83506SP62
Lamp1 Cell Signaling #3243S
hnRNP A1 abcam #ab5832
RPS14 Proteintech #16683-1-AP
NPM1 Cellsignaling #3542

Proliferation Assay

Cell proliferation was monitored Trypan blue exclusion assay and Doubling Time calculation.

4 Primary cell cultures

Unpublished data

Rationale

While both primary cell cultures and CRISPR knockout cells are indispensable tools in biological research, they serve distinct purposes and offer unique advantages.
Primary cell cultures are derived directly from living organisms, such as mice or humans. These cultures, established by isolating cells from their native tissue and cultivating them in vitro, retain the physiological properties and characteristics of the original tissue. This makes them invaluable tools for investigating normal cellular processes, drug responses, and disease mechanisms. However, primary cultures exhibit a finite lifespan and may contain a heterogeneous population of cells, which can introduce variability into experimental results .
CRISPR Knockout Cells on the other hand, are genetically engineered and one of the most significant advantages is their precision. It is possible to target and modify specific genes with remarkable accuracy, enabling detailed studies of gene function. Additionally, the ability to immortalize these cell lines ensures a consistent supply of material for long-term experiments.
Both primary cell cultures and CRISPR knockout cells have their strengths and weaknesses. Primary cells offer a more physiological perspective, while CRISPR knockout cells provide a powerful tool for genetic manipulation. In many cases, a combination of both approaches can yield the most comprehensive insights into biological processes[38].

Given the limitations of the CRISPR KO clones in accurately capturing the complex pathophysiological effects of Sil1 deficiency in Marinesco-Sjögren syndrome, we proposed to isolate fibroblasts and myoblasts *ex vivo* from Woozy mice in order to be closer to what occurs in the whole organism and to have a parallel comparison to the patient-derived skin fibroblasts.

Results

Primary fibroblasts were isolated from ear tissue of both Woozy and WT mice following the protocol described by Bravo et al.[39]. As depicted in Figure 4.2. panel (b), the cell culture exhibits morphological heterogeneity, suggesting a mixed population of cell types. This observation is consistent with previous studies indicating that both fibroblasts and myoblasts often co-isolate, resulting in a mixed cell population, sometimes referred to as myofibroblasts [40].

Consequently, the markers employed for cellular characterization, including immunofluorescence staining (Figure 4.1.) and Western blot analysis (Figure 4.2. panel (a)), are not entirely specific to either fibroblasts or myoblasts. Proteins such as α-SMA, vimentin, phalloidin, MyoD, and myogenin, are indeed expressed by both cell types.

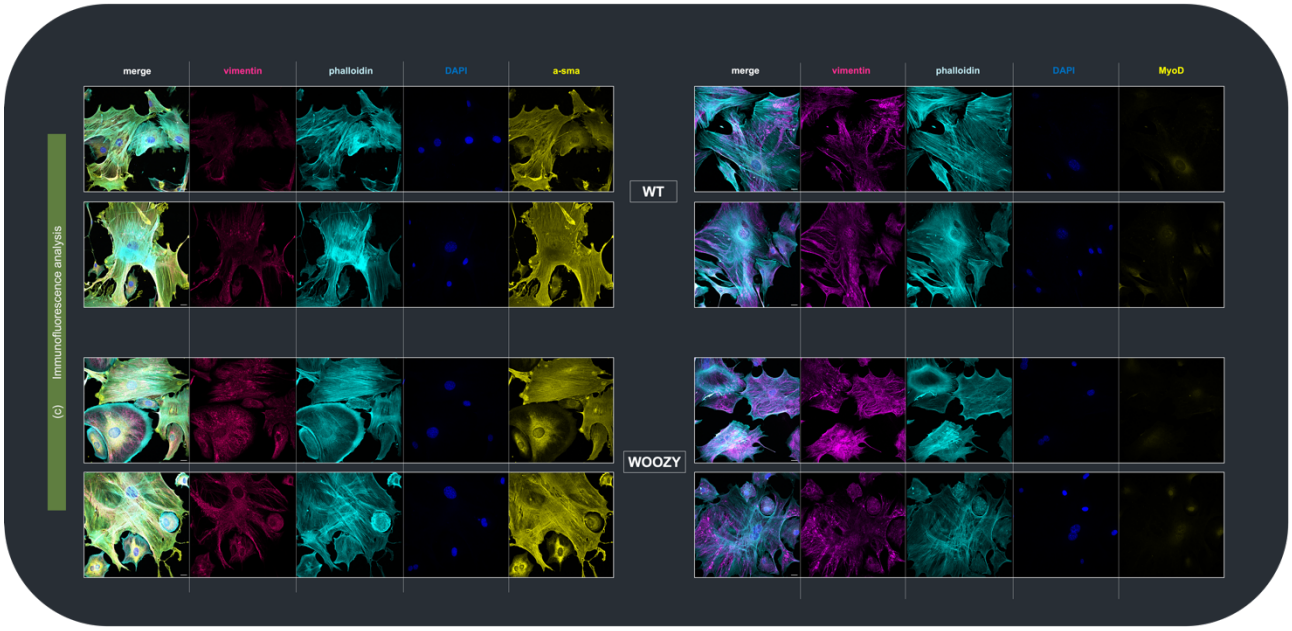


Figure 4.1. Immunofluorescence staining of primary fibroblasts from Woozy mice. Confocal images show staining for different characteristic fibroblast markers, including α-SMA and vimentin, as well as the myoblast marker MyoD. These results highlight that while fibroblasts primarily express markers associated with their lineage, they also exhibit low-level expression of myogenic markers such as MyoD.

From *"Generating an in vitro model for the study of Marinesco- Sjögren syndrome".* Potenza et al. FEBS Poster

To assess whether this relatively pure culture can be representative of MSS and could be compared to patient fibroblasts, we examined the expression levels of several markers previously identified through our proteomic analysis. Figure 4.1. (a) shows an increase of Lysosomal Associated Membrane Protein 1 (LAMP1), Vimentin (VIM), PDZ And LIM

Domain 5 (PDLIM5), and Caveolin-1 (Cav-1) as well as a decrease in Nucleophosmin (NPM).

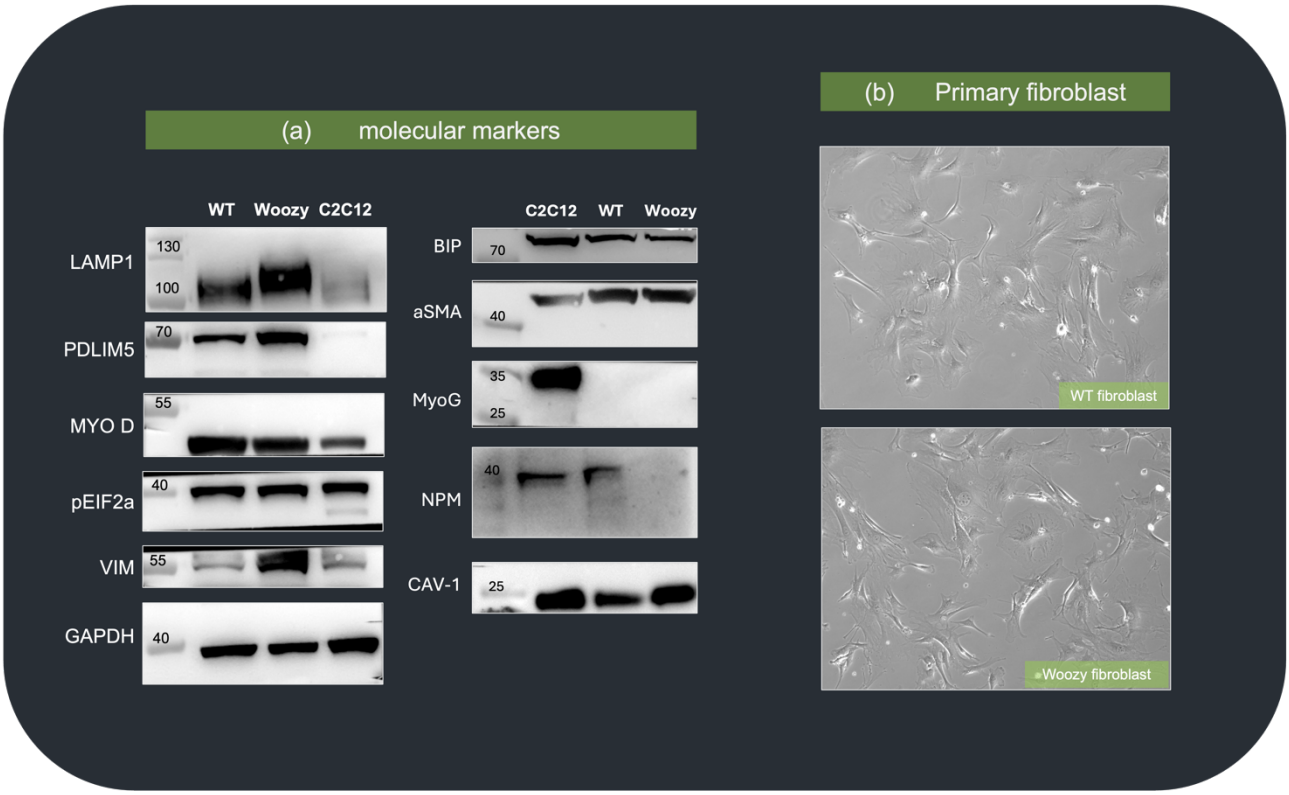


Figure 4.2. Primary fibroblast characterization. Fibroblasts from Woozy mice were compared to wild-type (WT) mice and C2C12 myoblasts. The expression levels of various markers were assessed, including myogenic markers (MyoD, MyoG), fibroblast-specific markers (vimentin, α-SMA), and markers associated with the MSS phenotype. Panel (b) Brightfield microscope images of primary fibroblast from Woozy mice in culture.

From *"Generating an in vitro model for the study of Marinesco- Sjögren syndrome".* Potenza et al. FEBS Poster

This primary cell line demonstrates a molecular profile which is similar to that observed in patient fibroblasts, according to our previous proteomic analysis. Consequently, it presents a promising tool for investigating the underlying pathological mechanisms associated with MSS. While the heterogeneity of the primary cell culture introduces certain limitations, it also provides a unique opportunity to explore the intricate interplay between fibroblasts and myoblasts within a disease context. Further research is warranted to comprehensively characterize the cellular composition of these cultures and to develop more specific markers that can differentiate between fibroblasts and myoblasts.

For this purpose, simultaneously, we sought to isolate myoblasts from woozy mouse muscle explants using a different protocol described by Vaughan and Lamia[41]. Our initial attempts resulted in the successful cultivation of myoblasts and their subsequent

differentiation into myotubes as shown in figure 4.3. panel (d). A comprehensive molecular characterization of these cultures is currently being conducted.

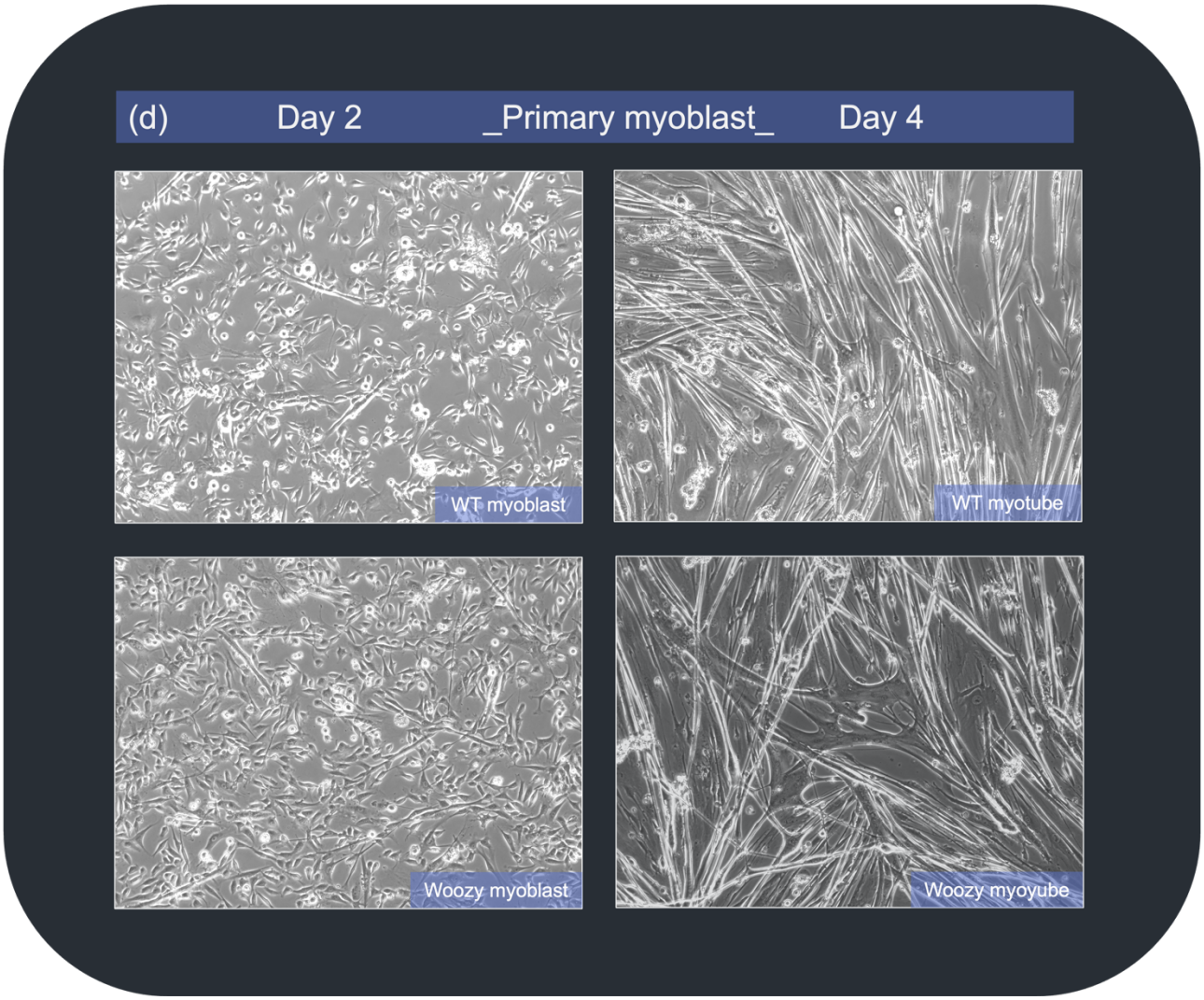


Figure 4.3. First attempt of primary myoblasts from Woozy mice extraction. Brightfield microscope images showing the myoblast stage on the left, and the differentiated myotubes after 4 days of culture.

From *"Generating an in vitro model for the study of Marinesco- Sjögren syndrome".* Potenza et al. FEBS Poster

Material and methods

Primary Fibroblast Isolation

Collect both ears from 5-weeks old mice, wash them with 70% Ethanol and shave as much fur as possible with a razor blade. Dip the ears in PBS with penStrep anf fungizone. Dice both ears in very small fragments (approximately 1-3 mm^3) and distribute them in a collagen pre-coated 10cm dish. Overlay with 3ml of Initial growth medium (DMEM glutamax with 20% FBS), avoid fragments floating. Keep dishes in 37°C incubator without any disturbance for at least 3 days. The 4^{th} day check for fibroblasts outgrow. After about 10 days from the explant, remove ear fragments with sterile forceps and harvest cells with trypsin. Plate cells in a non-coated flask and expand culture with fibroblast medium (DMEM glutamax with 10% FBS)[39].

Primary Myoblast Isolation

Collect muscles from a 4 to 8-week old mouse. To sterilize muscle tissue, rinse gently in PBS containing Pen/Strep and fungizone. Slice the muscle into small fragments (approximately 1-3 mm^3). Transfer the muscle fragments onto the surface of a Collagen-coated six/well plate. Gently overlay Plating Media (DMEM Glutamax-F12, FBS 40%) over the tissue that has to be hydrated but not floating. After 48 h, carefully check the plates to ensure that muscle fragments have adhered. Overlay with 2 mL of Plating Media, taking care not to dislodge the fragments. Keep the plates in the 37 °C incubator for up to an additional 3 days (5 days from original dissection) before harvesting myoblasts. Check every other day for outgrowth of myoblasts. Harvest myoblast with PBS first and resuspend them in Myoblast Medium (DMEM Glutamax-F12, FBS 20%) on pre-coated flask. Detach remaining cells with trypsin and plate them in a separate coated flask. Repeat this step for every other harvest (up to 3). This step allows myoblast to be separated from fibroblasts which are strongly adhering to the surface and need trypsin to be detached. Expand the harvested cells and use differentiation medium (DMEM glutamax-F12, 5% Horse serum), to obtain myotubes[41].

Western Blot Analysis

Cells were lysed in RIPA buffer [50 mM tris HCl (pH 7.6), 140 mM NaCl, 5 mM EDTA, 0.1% SDS, 1% NP40, 100 mM NaF, 0.1% Sodium deoxycholate] supplemented with protease (cOmpleteTM Tablets, Roche) and phosphatase (PhosSTOP tablets, Roche) inhibitors. Protein concentration was assessed by Bradford protein assay (Bio-Rad). Equal amounts of proteins were than resuspended in 4x Laemmli buffer [15% b-mercaptoethanol, 0.25 M Tris-HCl pH 6.8, 40% Glycerol, 8% SDS, 0.02% Blu Bromophenol], separated by SDS-PAGE, and transferred onto nitrocellulose membrane. The presence of proteins on the nitrocellulose membranes and their quantity was assessed by Ponceau S staining [0.5% (w/v) Ponceau S dissolved in 1% (v/v) acetic acid]. Filters were then blocked for 1 h at room temperature with either 5% non-fat dried milk or 5% BSA, and incubated with the primary antibodies overnight at 4 °C. Secondary antibodies α-rabbit and α-mouse were applied the day after for 1 h at room temperature and signal was detected by GE Amersham ECL.

Fluorescence Immunostaining and Confocal Microscopy

Cells were plated on cover slips to 70% density and the day after fixed in 4% paraformaldehyde (Electron Microscopy Science) for 15 min at room temperature. Cells were subsequently incubated for non-specific site blocking and permeabilization in blocking solution [0.05% saponin, 0.5% BSA, and 50 mM NH4Cl in PBS] for 40 min at room temperature. Primary antibody incubation was performed overnight at 4°C. The day after, fluorescent Alexa Fluor-conjugated anti-IgG secondary antibody was incubated for 40 min at room temperature, following a DAPI counterstain 10min RT. Signal was than detected with a confocal microscope (Zeiss LSM 800) and images were post-processed and analyzed by FIJI software.

List of primary antibodies used:

Bip/GRP78 BDbioscience #610979
Lamp1 Cell Signaling #3243S
NPM1 Cellsignaling #3542
Phospho-eIF2a (Ser51) Cell Signaling #3597S

PDLIM5 Proteintech 10530-1-AP

Myogenin Thermo Fisher 14-5643-82

Myo D BD Pharmingen 554130

MF20 Invitrogen 14-6503-82

VIMENTIN Cell Signaling #BK5741S

5 Second breakthrough

Sil1-deficient fibroblasts generate an aberrant extracellular matrix leading to tendon disorganization in Marinesco-Sjögren syndrome. August 2024.
https://www.ncbi.nlm.nih.gov/pmc/articles/PMC11342654/

Rationale

To gain a more comprehensive understanding of the molecular mechanisms underlying Marinesco-Sjögren syndrome (MSS), we delved deeper into the disease's genetic landscape. Building upon our previous proteomic analysis, we conducted a transcriptomic study on the same patient-derived fibroblasts. This approach allowed us to examine the expression levels of individual genes and explore potential correlations between gene and protein expression. By investigating both the proteome and the transcriptome, we aimed to elucidate the intricate molecular pathways involved in MSS pathogenesis.
This analysis revealed a significant number of differentially expressed genes, suggesting widespread cellular alterations. Notably, genes involved in membrane trafficking, extracellular matrix (ECM) remodeling, and cell adhesion were particularly affected.
To investigate the functional consequences of these genetic changes, we performed a series of experiments. Patient fibroblasts exhibited impaired ECM remodeling, reduced cell motility, and slower adhesion to surfaces. Furthermore, analysis of the ECM using electron microscopy revealed structural abnormalities in the organization of collagen fibers.
These findings suggest that alterations in the ECM may contribute to the diverse clinical manifestations of MSS. The ECM provides essential structural support and plays a critical role in cell signaling and tissue homeostasis[42]. Disruptions in ECM integrity can affect various organs, including the nervous system, muscles, bones, and lens, all of which are affected in MSS.

Results

Changes in the extracellular matrix and anchoring junctions in fibroblast isolated from a patient affected by Marinesco-Sjögren syndrome

To elucidate the molecular mechanisms underlying Marinesco-Sjögren Syndrome (MSS), we performed a transcriptomic analysis of skin fibroblasts obtained from a young patient diagnosed with the disease. Total RNA extracted from fibroblasts cultured under standard conditions was subjected to next-generation sequencing to assess gene expression levels. As a control, fibroblasts from a healthy individual were processed in parallel.
Our analysis, conducted in triplicate, identified 664 differentially expressed (DE) transcripts with a fold change (FC) greater than 2 and a false discovery rate (FDR) less than 0.1. A heatmap of the top 50 most variable genes, based on hierarchical clustering of logFC values, is presented in Figure 5.1 A.
To explore the functional implications of these DE genes, we utilized the STRING protein-protein interaction database. The analysis revealed significantly more interactions among the DE genes than expected by chance, supporting the reliability of our transcriptomic results.
To gain further insights into the biological processes affected by these gene expression changes, we performed gene ontology (GO) enrichment analysis. Our gene set was significantly enriched for 237 biological processes, 6 molecular functions, 30 cellular components, and 24 subcellular compartments.
Consistent with previous studies, the enrichment analysis confirmed a membrane trafficking defect in patient fibroblasts. Notably, intracellular organelles accounted for 4 out of 24 subcellular compartments and were represented by over 350 DE genes.
Interestingly, the most represented subcellular compartments were the extracellular space/matrix and those associated with cell-matrix and cell-cell adhesion, collectively accounting for 15 of the 24 compartments and encompassing more than 150 DE genes.
The involvement of both the endomembrane system and ECM/cell adhesion was further corroborated by the enrichment analysis of cellular components (Figure 5.1. B).
Collectively, our findings suggest that alterations in membrane trafficking, extracellular matrix remodeling, and cell adhesion may contribute to the pathogenesis of MSS.
To assess the generalizability of the gene alterations identified in this study to Marinesco-Sjögren Syndrome (MSS), we compared the enriched biological processes from our

transcriptomic analysis with those from our previous proteomic study[14] on the same fibroblasts and with those from Sil1Gt mouse muscle[15].

Approximately 50% of the biological processes were shared between the current transcriptomic and previous proteomic studies, while around 30% overlapped with the mouse muscle proteomic data. To evaluate the statistical significance of this overlap, we performed a computer simulation, which revealed that a random selection of biological processes would result in only a 3% overlap. This suggests that the observed overlap between the studies is highly significant and not due to chance.

We further analyzed the DE genes using Ingenuity Pathway Analysis (IPA). This analysis identified several downregulated pathways related to the extracellular matrix (ECM), including glycoprotein VI signaling, glioma invasiveness signaling, and pathways involved in tumor microenvironment, Rho GTPase signaling, pulmonary fibrosis, and hepatic fibrosis. Additionally, IPA indicated decreased cellular movement and migration, increased apoptosis, decreased cell survival, and decreased cell proliferation. These findings align with our previous study and further support the involvement of the ECM and potential alterations in cell death and proliferation.

To experimentally validate the findings of our transcriptomic analysis, we selected 13 differentially expressed (DE) genes, including SIL1 itself, for quantitative real-time PCR (qPCR) analysis. These genes were chosen based on their significant fold change and low false discovery rate (FDR). However, to ensure a comprehensive assessment of the diverse functional alterations associated with Marinesco-Sjögren syndrome (MSS), we also included genes involved in extracellular matrix (ECM) remodeling, cell cytoskeleton dynamics, vesicle trafficking, and endosome-lysosome-autophagy pathways.

The transcriptomic analysis and the extraction of genes to be validated through real-time PCR was the process in which I had the greatest participation.

The results confirmed the upregulation of seven genes and the downregulation of five genes, further supporting the reliability of the transcriptomic data, as shown in Figure 5.1. C.

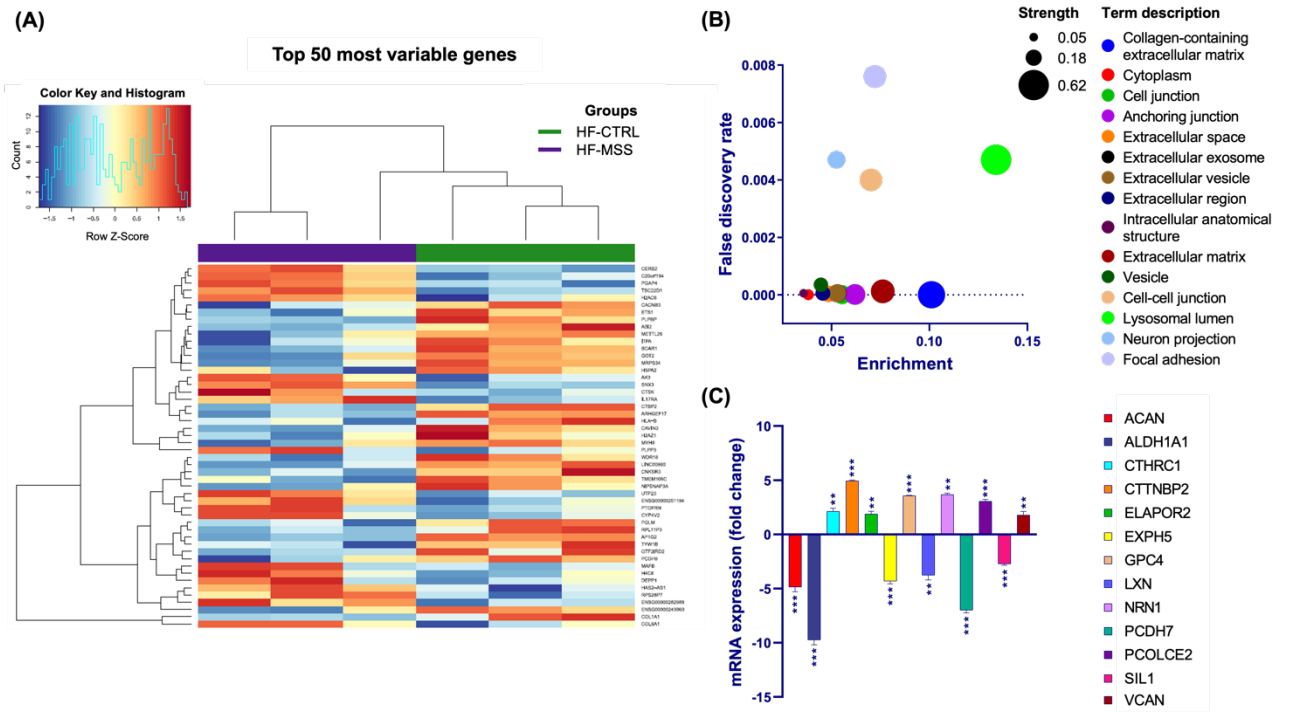


Figure 5.1. Differentially expressed genes in fibroblasts from an MSS patient compared with a healthy control. A) Heat map of the modulated genes. The heatmap shows the top 50 most variable genes based on the logFC value. Upregulated genes are reddish while downregulated genes are in blueish as reported in the colour key histogram. Control and patient fibroblast samples are indicated by a green and violet bar respectively. Gene names are indicated on the right. (B) Bubble plot of cellular components enriched by differentially expressed genes. Enrichment is calculated as the ratio of the number of observed genes to the total number of genes associated with that specific ontology. The strength represents the Log10 of the ratio between the number of genes annotated to a specific ontology and the number of genes expected to be annotated to that ontology if they were picked randomly from a group of the same size. (C) Quantitative PCR analysis. Twelve differentially expressed genes identified by transcriptomic analysis were validated by quantitative reverse transcriptase PCR. Data are expressed as fold change and gene names are in the legend shown on the right. One-way ANOVA was performed to compare ΔCt values. ** p > 0.01, *** p > 0.001. Results are presented as mean± standard error of fold changes from three independent experiments performed in technical triplicate

From "Sil1-deficient fibroblasts generate an aberrant extracellular matrix leading to tendon disorganisation in Marinesco-Sjögren syndrome". Amodei et al. 10.1186/s12967-024-05582-0

Remodelling of extracellular matrix is impaired in both patient fibroblasts and Woozy mice

To further investigate the functional consequences of the identified gene expression changes on extracellular matrix (ECM) remodeling, we assessed the ability of patient fibroblasts to degrade and internalize a fluorescently labeled collagen probe (Figure 5.2. A, B, C, D and F). Both control and patient cells initially internalized the probe. However, over extended incubation periods, patient cells exhibited a significant reduction in collagen degradation and internalization compared to control cells.

This impairment in ECM remodeling was attributed to several factors, including:

- Reduced metalloprotease activity: Patient fibroblasts displayed decreased expression of key metalloproteases responsible for collagen degradation.

- Increased expression of metalloprotease inhibitors: Elevated levels of metalloprotease inhibitors in patient cells further hindered ECM degradation.

These findings were supported by both cellular assays and analysis of conditioned media. The reduced proteolytic activity observed in the conditioned medium of patient fibroblasts directly correlated with the impaired ECM remodeling phenotype (Figure 5.2. E).

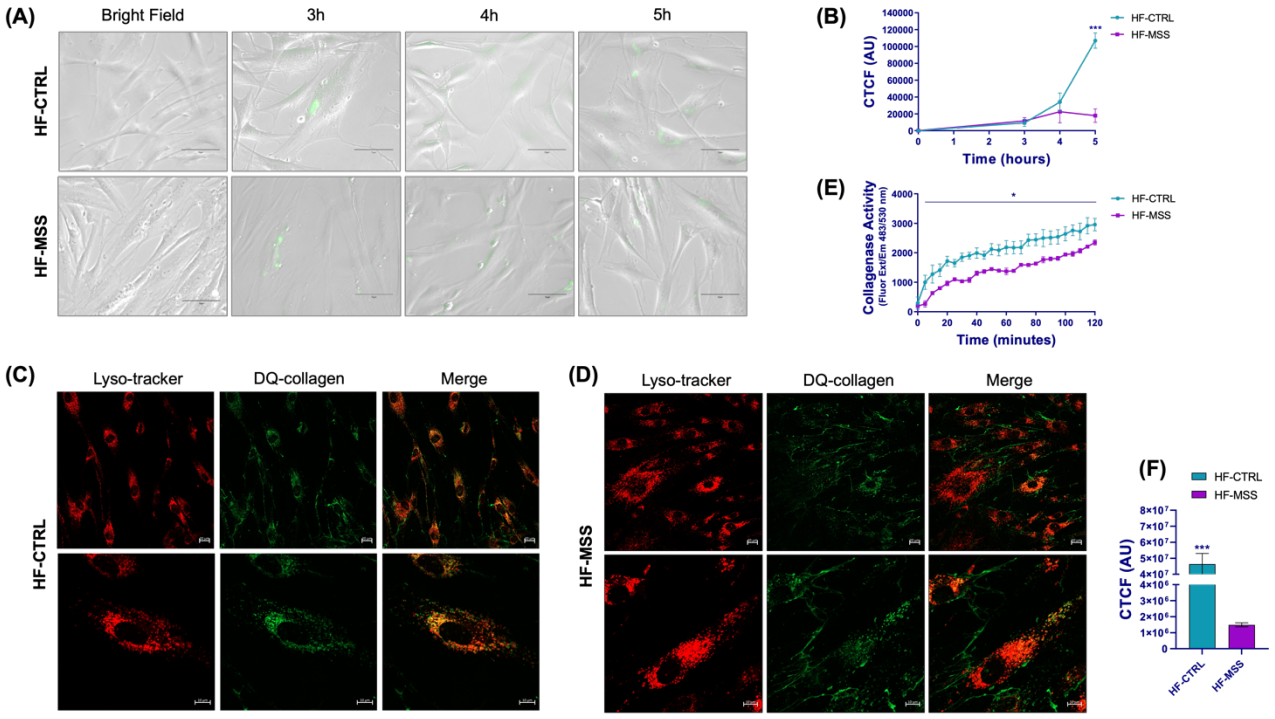


Figure 5.2. Live cell imaging of DQ-collagen internalization in fibroblasts and collagenase activity.
(A) Panels show representative images of DQ-collagen fluorescence internalised in control (HF-CTRL) and patient fibroblasts (HF-MSS) over time. (B) Quantitation of the fluorescence of the experiment shown in A. The y axis represents the corrected total cell fluorescence (CTCF) expressed as arbitrary units. Results are presented as mean ± standard error from three independent experiments. Repeated measure ANOVA over time points and post parametric multiple t test were performed; *** $p < 0.001q < 0.001$. (C-D) Control fibroblasts (HF-CTRL in C) and patient fibroblasts (HF-MSS in D) grown on ibidi µ-slide were incubated with DQ-collagen for 5 h, followed by LysoTracker for 3 h. Live cells were imaged by confocal microscope using the 495 and 647-nm lasers. LysoTracker and DQ-collagen fluorescence are shown in red and green respectively. Colocalization of lysosomes and DQ-collagen is shown by merging the fluorescence. Two different magnifications are shown. Results are from two independent experiments performed in technical triplicate. (E) Collagenase activity of fibroblast conditioned medium. Cell-free supernatants of fibroblasts were incubated with DQ-collagen and fluorescence development was measured every 5 min. Results are presented as mean ± standard error from two independent experiments performed in technical triplicate. Repeated measure ANOVA over time points and post parametric multiple t test were performed; * $P < 0.05$. (F) The graph shows the quantification of internalized collagen in HF-CTRL and HF-MSS of the experiments shown in C and D. *** $P < 0.001$

From "Sil1-deficient fibroblasts generate an aberrant extracellular matrix leading to tendon disorganisation in Marinesco-Sjögren syndrome". Amodei et al. 10.1186/s12967-024-05582-0

Transmission electron microscopy (TEM) analysis revealed significant differences in the extracellular matrix (ECM) produced by patient and control fibroblasts. While the ECM secreted by control fibroblasts exhibited a well-organized network of thin, uniform filaments, the ECM from patient fibroblasts displayed a markedly distinct morphology. The patient-derived ECM was characterized by thicker, ribbon-like filaments that tended to aggregate into larger, primitive fibrils[43]. These aberrant structures were significantly larger than those observed in the control ECM, suggesting a disruption in the normal ECM assembly process.

The altered ECM morphology in patient fibroblasts likely reflects underlying defects in ECM remodeling. The increased thickness and aggregation of filaments may be attributed to impaired proteolytic activity, reduced clearance of ECM components, or altered cross-linking mechanisms. These abnormalities in ECM structure and composition could have profound implications for cell behavior, tissue homeostasis, and disease progression in Marinesco-Sjögren syndrome.

To directly visualize the impact of altered ECM processing on the extracellular matrix (ECM) structure, we employed transmission electron microscopy (TEM) to analyze the ECM produced by patient and control fibroblasts. TEM images revealed striking differences between the two groups (Figure 5.3). The ECM secreted by control fibroblasts exhibited a well-organized network of thin, uniform filaments, indicative of a mature, organized matrix. In contrast, the ECM derived from patient fibroblasts displayed a markedly distinct morphology. Thicker, ribbon-like filaments were observed, often aggregating into larger, primitive fibrils. These aberrant structures were significantly larger than those found in the control ECM, suggesting a disruption in the normal ECM assembly process.

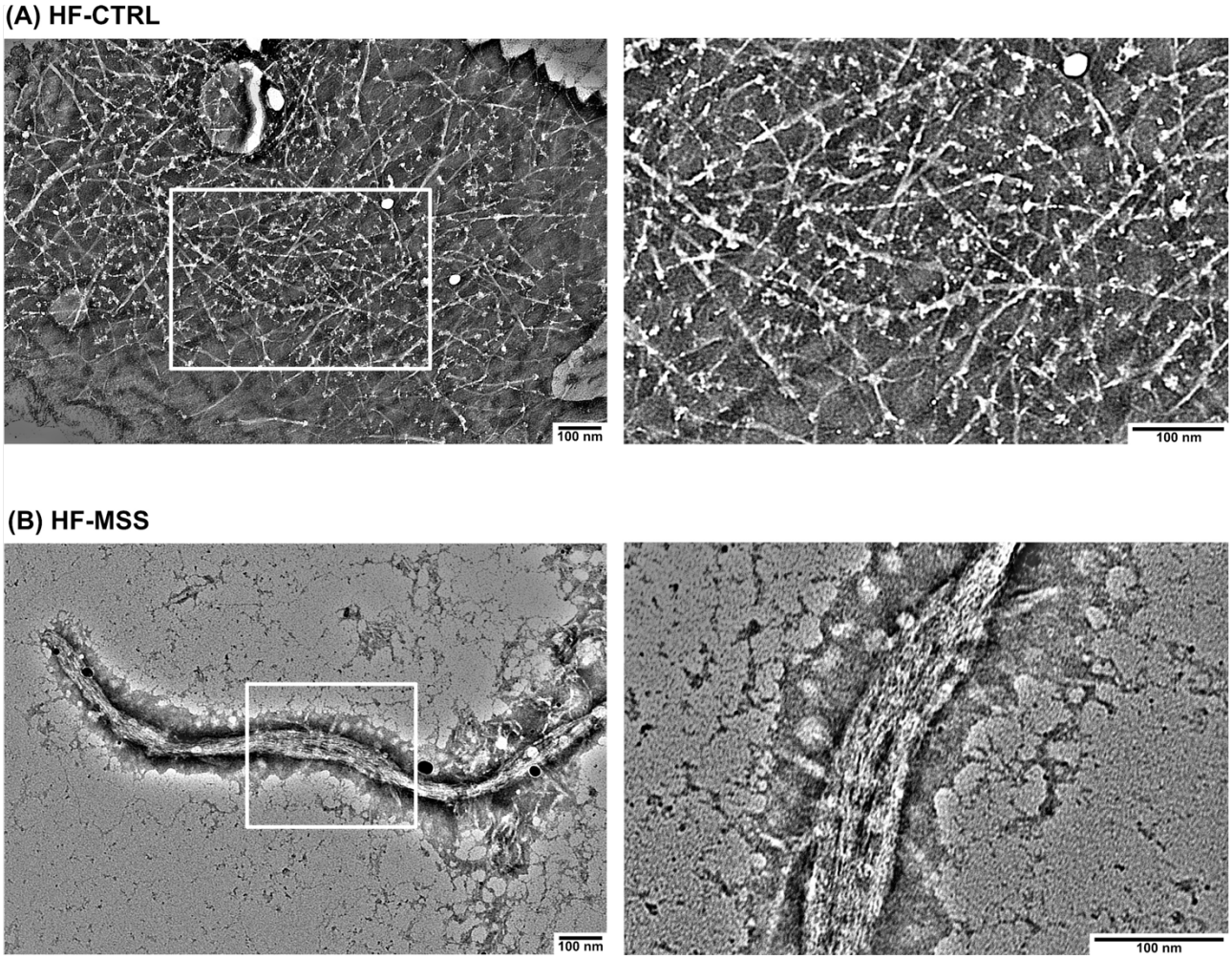


Figure 5.3. TEM analysis of negative-stained ECM released by fibroblasts**.**
Fibroblasts grown to 80% of confluence were incubated with serum free HBSS medium for 24 h. The day after, the conditioned medium was collected, refrigerated and a 5 µL drop has been applied onto carbon-coated grid. The grid was stained and air-dried before imaging by TEM. (A) Representative micrographs of ECM generated by control fibroblast (HF-CTRL), at low (left) and high (right) magnification. (B) Representative micrographs of ECM generated by patient fibroblast (HF-MSS), at low (left) and high (right) magnification. Results are from two independent experiments performed in technical triplicate

From "Sil1-deficient fibroblasts generate an aberrant extracellular matrix leading to tendon disorganisation in Marinesco-Sjögren syndrome". Amodei et al. 10.1186/s12967-024-05582-0

To further investigate the in vivo implications of the ECM alterations observed in cultured fibroblasts, we turned our attention to the "woozy" mouse model of Marinesco-Sjögren syndrome (MSS). The Achilles tendon-soleus muscle junction was selected for detailed examination due to its crucial role in muscle function and integrity.
In wild-type mice, this junction exhibited a well-organized structure. Collagen fibers were arranged in a regular pattern, and tenocytes, the specialized fibroblasts within the tendon, displayed a healthy morphology with intact organelles. In contrast, the woozy mouse model revealed significant deviations from this normal architecture. The collagen fibers

were less organized, exhibiting a more irregular pattern. Tenocytes displayed marked degenerative changes, including damaged mitochondria and cellular debris. Moreover, the ECM surrounding these cells contained irregular, overstructured filaments, reminiscent of those observed in the conditioned medium of patient fibroblasts (Figure 5.4.).

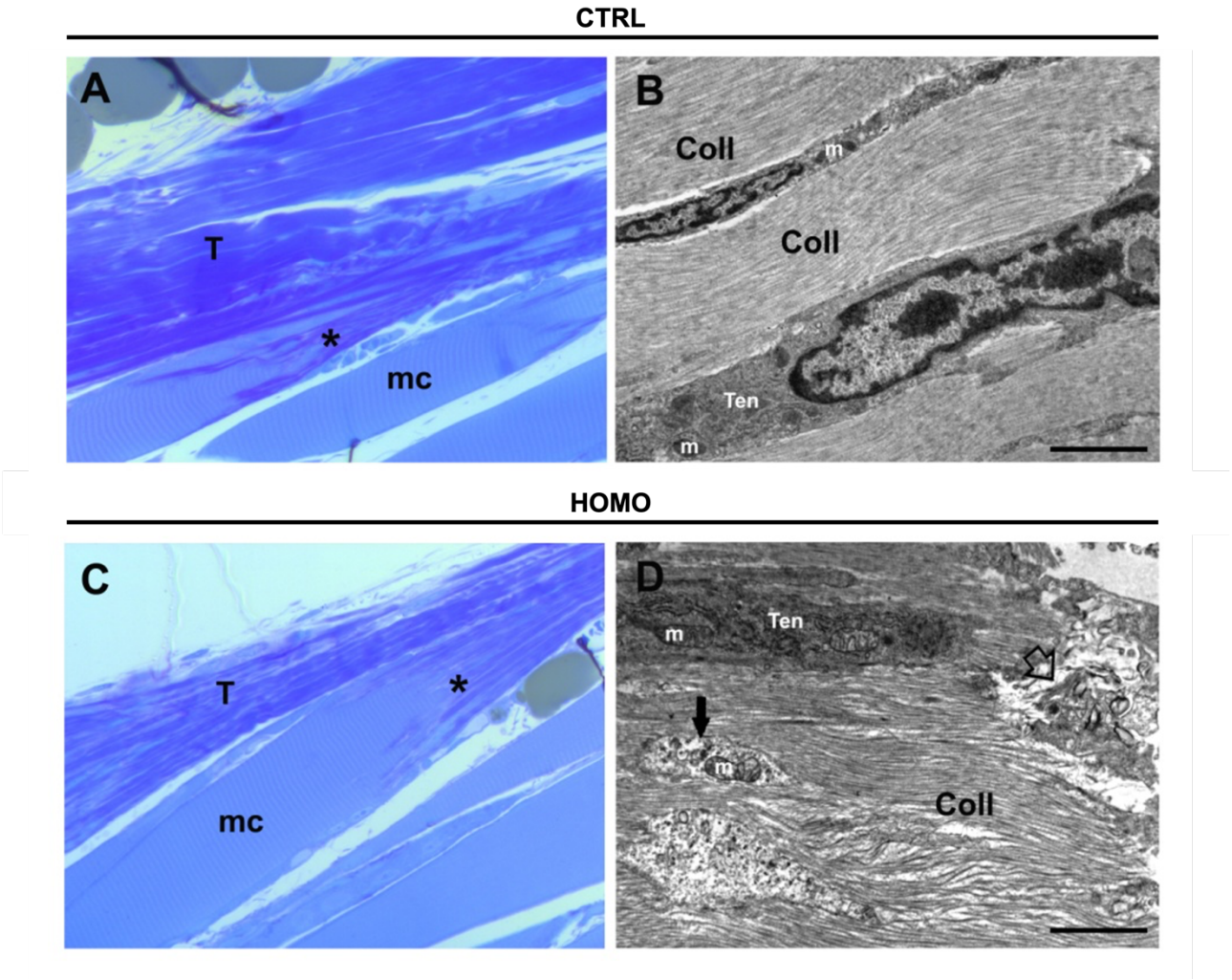


Figure 5.4. Light and transmission electron microscopy (TEM) analysis of Achilles tendons of control and woozy mouse. (A and C) Toluidine blue stained semi thin-sections of the boundary between Achilles tendon (T) and the soleus muscle (mc) from heterozygous (SIL1+/−) control (CTRL, A) and woozy (SIL1−/−) mice (HOMO, C). The myotendinous junction (MTJ) is indicated by asterisk. (B and D) Representative images at TEM higher magnification of the connective tissue in control (CTRL, B) and woozy mice (HOMO, D), with tenocytes (Ten) arranged between the collagenous fibrils (Coll) of the ECM. Some organelles are visible (e.g. mitochondria, m) as well as cell debris (black arrow), and areas of degeneration (empty arrow).

From "Sil1-deficient fibroblasts generate an aberrant extracellular matrix leading to tendon disorganisation in Marinesco-Sjögren syndrome". Amodei et al. 10.1186/s12967-024-05582-0

These in vivo findings suggest that the ECM alterations observed in vitro are not merely a cell culture artifact but may contribute to the pathological changes seen in the woozy mouse model. The disrupted ECM structure and impaired tenocyte function could

potentially impact muscle function and other tissues affected by Marinesco-Sjögren syndrome. Further investigation is warranted to fully elucidate the role of ECM alterations in the pathogenesis of this disease.

Discussion

Marinesco-Sjögren syndrome (MSS) is a rare, autosomal recessive neurodegenerative disorder characterized by ataxia, myopathy, intellectual disability, and skeletal and ocular abnormalities. Mutations in the SIL1 gene, which encodes a critical component of the endoplasmic reticulum (ER) protein quality control system, are a major cause of MSS. However, the precise mechanisms underlying the diverse clinical manifestations of this disorder remain incompletely understood[3].

Recent studies have shed light on the potential role of extracellular matrix (ECM) dysregulation in the pathogenesis of MSS[44]. Transcriptomic analysis of patient-derived fibroblasts has revealed significant alterations in the expression of genes involved in ECM production, remodeling, and cell-matrix interactions. These findings suggest that impaired ECM homeostasis may contribute to the development of various tissue-specific pathologies associated with MSS.

In vivo studies, such as those conducted on the "woozy" mouse model of MSS, have further supported the involvement of ECM alterations in the disease. These studies have demonstrated significant disruptions in the organization of collagen fibers and tenocyte morphology in the Achilles tendon-soleus muscle junction of woozy mice. These findings underscore the importance of ECM integrity in maintaining tissue function and suggest that ECM dysregulation may contribute to the development of muscle weakness and other musculoskeletal manifestations of MSS.

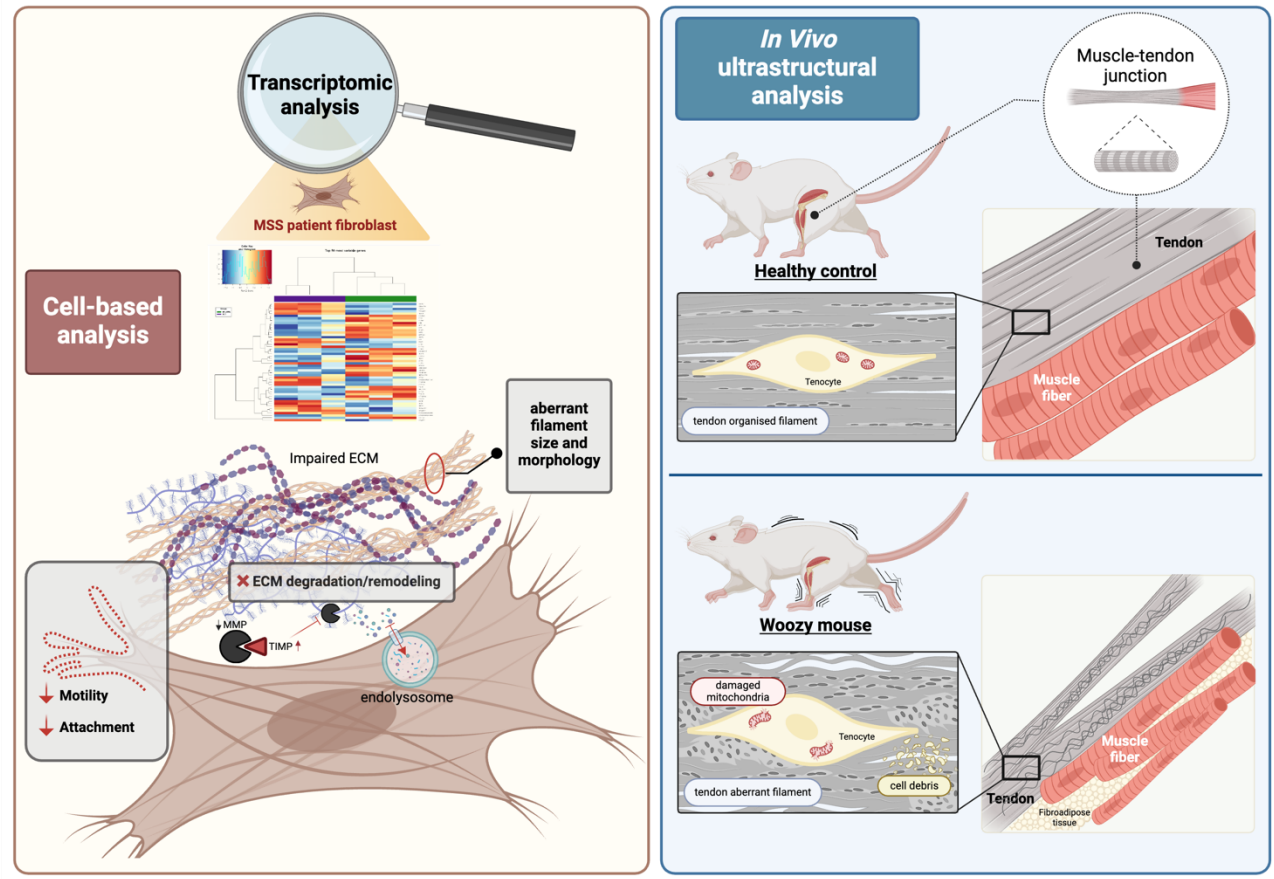


Figure 5.4. Through molecular, cellular and histological approaches in vitro and in vivo, we revealed changes in the ECM and tendons of woozy mice that may explain part of the pathological mechanism of MSS. The left panel summarises in vitro experiments showing genes differentially expressed in control and patient fibroblasts. These molecular changes impair ECM dynamics, resulting in an aberrant ECM that in turn slows cell adhesion and reduces cell motility. The right panel represents the disorganised fibrils of the woozy mouse tendon both histologically and ultrastructurally. It also represents the damage to the tenocytes.

From "Sil1-deficient fibroblasts generate an aberrant extracellular matrix leading to tendon disorganization in Marinesco-Sjögren syndrome". Amodei et al. 10.1186/s12967-024-05582-0

In conclusion, our transcriptomic analysis has identified the extracellular matrix (ECM) as a primary cellular compartment affected in Marinesco-Sjögren syndrome (MSS). The ECM is a dynamic and complex network that plays a pivotal role in various cellular processes, including cell signaling, migration, and differentiation[42]. Given the extensive evidence linking ECM dysregulation to the dysfunction of the central nervous system, skeletal muscle, bone, and lens, we propose that aberrant ECM remodeling may be a key pathological mechanism underlying the diverse clinical manifestations of MSS.

Material and methods

Cell cultures

Primary Human Dermal Fibroblast (NDHF Promo Cell #FB60C12350) supplied by Carlo Erba Reagents were used as the control cell line and compared with primary dermal fibroblast from a young Marinesco–Sjögren syndrome patient, supplied by Telethon Network of Genetic Biobanks-TNGB [21]. Cells were cultured in a humidified CO2 incubator at a temperature of 37 °C using Dulbecco's modified Eagle's medium + GlutaMAX (GIBCO, 61965026), supplemented with 10% of Fetal Bovine Serum (FBS) and 1% penicillin/streptomycin PenStrep (GIBCO, 15070-063). Cells were subcultured when they reached 90% confluence and detached with Trypsin-EDTA 0.5% (GIBCO, 15400-054). All experiments were performed with cells within the 12th passage.

Transcriptomic analysis

Total RNA was extracted from control and patient fibroblast in triplicate experiments using the miRNeasy micro kit (Qiagen, 217004) according to the manufacturer's instructions. Transcriptomic analysis was carried out by next generation sequencing (NGS) RNA sequencing at BMR Genomics Padova, Italy. RNA integrity was determined by analysis of extracted total RNA using a 2100 Bioanalyzer (Agilent Technologies) with RNA 6000 NanoChip. RNA concentrations were measured using Qubit RNA Assay Kit. Libraries were prepared from total RNA according to manufacturer instructions with Lexogen QuantSeq 3' mRNAseq Fwd kit. Libraries quality were evaluated by size analysis on 2100 Bioanalyzer (Chip DNA HS) and concentrations were determined using Qubit DNA HS assay kit (Thermo Fisher). Sequencing was performed on Illumina Nextseq 500 generating about 5 million/read per sample, SE75 format. Reads preprocessing was performed by using fastp v0.20.0 applying specific parameters in order to remove residual adapter sequences and to keep only high quality data. Passing filter reads were mapped to the genome reference (Homo sapiens) v105 of Ensembl repository using STAR v2.7.0. Alignments were elaborated by RSEM v1.3.3 and sample-specific gene-level abundances were merged into a single raw expression matrix applying a dedicated RSEM command (rsem-generate-data-matrix). Genes with at least 10 counts in 3 samples were then selected. Differential expression was computed by edgeR from raw counts in each comparison.

Multiple testing controlling procedure was applied and genes with a false discovery rate (FDR) ≤ 0.1 and log fold change (FC) > |0.5| were considered differentially expressed. The heatmap represents a selection of the 50 most differentially expressed genes based on the logFC value. In order to create the graph, the R library (pheatmap) with an unbiased hierarchical system was used.

Computer simulation

In order to understand the significance of the overlap between the 237 biological processes identified in this study and a previous one which identified 898, we generated 898 uniformly distributed pseudo-random integers ranging from 1 to 27,597 (number of biological processes in the GO database) with the Matlab algorithm. These numbers were associated to the biological processes in the GO database. Random generation, association and overlap calculation of these random biological processes with the 237 biological processes identified in this study was repeated 10,000 times. Then, the mean overlap across the 10,000 repetitions was computed.

Quantitative real-time PCR (q-PCR)

Total RNA from fibroblasts was extracted using TRIzol reagent. RNA was than retrotranscribed using the kit (High Capacity cDNA Reverse Transcription Kit #4368813 from Applied Biosystems) according to the manufacturer's instructions. The q-RT-PCR reactions, based on SYBER green chemistry (Sensifast SYBR HiRox #BIO-92020 from Bioline), were performed using CFX C1000 (BIORAD) and the expression of selected genes is presented relative to the mean of housekeeping reference, i.e. glyceraldehyde-3-phosphate dehydrogenase (GAPDH) (ΔΔCt method) (Table 5.1). The PCR primer sequences were as follows: One-way ANOVAs were performed to compare ΔCt values for each gene between the two groups. Then Benjamini-Hochberg adjusted p-values were computed to adjust for multiple comparisons.

Table 5.1. Primer sequences used in this study

Gene name	FW sequence 3′-5′	REV sequence 3′-5′
ACAN	CTG CTA TGG AGA CAA GGA TGA G	CTG GAG ATG TTG CAT AAA AGA CC
ALDH1A1	AGC AGG AGT GTT TAC CAA AGA	CCC AGT TCT CTT CCA TTT CCA G
CTHRC1	CAA TGG CAT TCC GGG TAC AC	GTA CAC TCC GCA ATT TTC CCA A
CTTNBP2	CCG TGG GAC TTT ATG AGG AAG	GAG GGA TCA TGG AGG CAT AAG
ELAPOR2	CCT GGC AAC ATG AAA ACT TCC	TCA TTG TCA GAA CCT CCA GC
EXPH5	TGG GAC AGA AAG GAT GTG ATG	CTG GCT TTG GGA CAA ATG TAC
GAPDH	CTG GGC TAC ACT GAG CAC C	AAG TGG TCG TTG AGG GCA ATG
GPC4	AGG AAA CGG CAA TGA GGA TG	GAC GAA GGA TCA GTA TGT CTG G
LXN	ACA GAA CTA CAT CAA CTA CCA GC	GTG ATA CTT ATG TCC TCT TCC TGG
NRN1	ACA AGA CGA ACA TCA AGA CCG	TTA TCC CAC ATA TCT TTC GCC C
PCDH7	TGT CAA ACC AAT AAC AAG TAC AGC	ACT GCT TGG TGT TTC TGA CTC
PCOLCE2	GGG AAG TCA ACG ATG CTA GAA G	GTG ACC AAT AAA CCC ATC TGC
SIL1	GCT TCA CCT TCT GCC TCA GTC A	AAC ACC TCC AGG ACT TCG GCA T
VCAN	GGT GGT CTA CTT GGG GTG AG	GTG ATG CAG TTT CTG CGA GGA

Collagen degradation/internalization assay

Control and patient fibroblasts were seeded in 24-well plates (3×10^4 cell/well) or into ibidi µ-slide 8-well glassbottom plates ($19{,}5 \times 10^2$ cell/well) for widefield or confocal analysis, under standard growth conditions. After 24 h medium was replaced with Dulbecco's Modified Eagle Medium (DMEM) serum-free and after 16 h cells were incubated with 10 µg/mL of dye-quenched (DQ)collagen (Invitrogen, Carlsbad, CA) up to 5 h. Collagen degradation was monitored by detection of the green signal in a fluorescence microscope (EVOS®FL, AMG, USA). The fluorescence intensity of each cell was calculated using a formula for corrected total cell fluorescence (CTCF) = integrated density–(area of selected cell × mean fluorescence of background readings). For confocal analysis, cells were treated as above and exposed to LysoTracker (ThermoFisher) as for the manufacturer's instructions. Images were acquired with a Zeiss LSM880 confocal microscope (Zeiss) using 495 and 647-nm lasers and as previously described. Quantification of DQ collagen internalization in confocal images was performed according to the procedure described above for the fluorescence microscope and expressed as CTCF. Collagenase assays Cell-free supernatants were tested for collagenase activity with the EnzChek Gelatinase/Collagenase assay kit (Invitrogen, Carlsbad, CA). Control and patient fibroblasts were seeded in 24-well plates 3×10^4 cell/well under standard growth conditions, and after 24 h medium was replaced with DMEM serum-free. After 16 h cell supernatants were collected, centrifugated at 3000 g for 10 min at room temperature, and filtered using a 0.2 µm Minisart sterile filter (Sartorius). Reactions were prepared by mixing 100 µL of conditioned media with 20 µL of the substrate at 100 µg/mL and 80 µL of reaction buffer in black optical bottom 96- well plates (Greiner BioOne, Monroe, NC).

Plates were incubated in a Synergy H1 microplate reader (BioTek, Winooski, VT) at 37 °C in atmospheric conditions. Kinetic fluorescence reads were measured after 7 s shaking every 5 min at 485 nm excitation/527 nm emission. There was no need to normalize collagenase activity because the total amount of proteins, at the time of the experiment, was the same in the control and in the patient fibroblasts.

Cell adhesion assay

Control and patient fibroblasts were seeded in 96-well plates (5×10^2 cells/well) and settled at RT for 15 min before being placed into Incucyte® Live Cell Analysis System (Incucyte® S3/ -Sartorius) at 37°C in a humidified CO_2 incubator. Four phase-contrast images of each well were acquired every 3 h for 24 h using 10X objective. Images were analysed by Incucyte® Cell-by-Cell Analysis Software, and data were exported for further statistical analysis on GraphPad Prism 9. Statistical differences in the average phase object area between control and patient fibroblasts over time were determined using repeated measure ANOVA over the 9 time points. Fisher LSD post-hoc test was used to compare average phase object area value at the same time point between groups. P value < 0.05 was the threshold for statistical significance.

Motility assay

Cell motility was assessed according to the protocol for Incucyte Scratch Wound Assay. Control and patient fibroblasts were seeded in 96-well ImageLock™ plate to reach maximum density of 100% (2×10^4 cells/well) and incubated overnight in standard growth conditions. The next day, the 96-pin Incucyte WoundMaker (Sartorius) was used to create a precise and uniform wound simultaneously in each well. Cells were washed twice with PBS and then incubated into Incucyte® Live Cell Analysis System (Incucyte® S3/ -Sartorius). Two phase contrast images from each well were acquired every 3 h for 24 h using 10X objective. Relative wound density was analysed using Incucyte® Scratch Wound Analysis Software Module, and data were exported for further statistical analysis on GraphPad Prism. Statistical differences in the relative wound density between control and patient fibroblasts over time were determined using repeated measure ANOVA as

described for the average phase object area. P value < 0.05 was the threshold for statistical significance.

Transmission electron microscopy (TEM) of soluble ECM

Controls and patient fibroblasts at 80% of confluency were incubated with serum and antibiotic-free medium over-night. The next day, the conditioned medium was collected and centrifuged at 20,000 rpm to remove any residual cells or cellular debris. The protein concentration of the conditioned medium quantified by was on average 14.0 ± 1.8 and 10.8± 1.0 µg/mL for control and patient fibroblasts, respectively. The overall morphology of the ECM samples collected as described, has been characterized by TEM using a CM 100 transmission electron microscope (Philips) equipped with a tungsten filament and operating at 100 kV. The specimens have been prepared by negative staining as previously described for protein molecules. Briefly, a 5 µL drop of each ECM sample at concentration 10–15 µg/mL has been applied onto a 200-mesh carbon-coated grid (Agar Scientific Ltd) and let adsorb 1 min before dropping it downwards on 100 µL commercial Nano-W stain (2% organotungsten compound, Nanoprobes Inc.). Thereafter, the excess of stain has been removed by touching the grid side with Whatman filter paper (Merck KGaA) and the grid left to air-dry before imaging by TEM. When necessary, the acquired micrographs have been post-processed using a high-pass or fast Fourier transform (FFT) bandpass filter by means of ImageJ v1.54 to reduce edge artifacts derived from low or over-exposure to the electron beam.

Mice

Woozy mice (CXB5/By-Sil1wz/J) purchased from The Jackson Laboratory (Stock N°. 003777), housed at controlled humidity and temperature were provided with a standard diet and water ad libitum. The mouse colony was propagated by heterozygous mating and genotyped by standard PCR. All procedures involving the mice were performed according to the protocol approved by the Institutional Animal Care and Use Committee of the Italian Ministry of Health (authorization n° 596/2021-PR, issued pursuant to art. 31 of Legislative Decree 26/2014). Animal housing facilities meet international standards and are regularly inspected by a certified veterinarian.

Histology and TEM of woozy mouse Achilles tendon

Samples were carefully dissected from 7 months old woozy (n = 3) and control (n = 3) mice, pinned on Sylgard dishes, fixed at room temperature with 3.5% glutaraldehyde in 0.1 M NaCaCO buffer (pH 7.2) and kept at 4°C in fixative solution until further use. Fixed samples were then postfixed in 2% OsO4 in the same buffer for 2 h, then block-stained in uranyl acetate replacement. After dehydration, specimens were embedded in an epoxy resin (Epon 812; Electron Microscopy Sciences, Hatfield, PA, USA), as previously described. For histological examination by light microscopy, semithin sections (~700 nm) were cut using a Leica Ultracut R microtome (Leica Microsystem, Vienna, Austria) with a diamond knife (Diatome, Biel, Switzerland) and stained in a solution containing 1% toluidine blueO and 1% sodium borate (tetra) in distilled water for 3 min on a hot plate at 55–60°C. After washing and drying, sections were mounted with DPX media for histology (Sigma–Aldrich, Milan, Italy) and observed with a Leica DMLB light microscope connected to a DFC450 camera equipped with Application Suite v 4.13.0 for Windows (Leica Microsystem, CMS GmbH, Switzerland). For TEM, ultrathin sections (~50 nm) were cut using a Leica Ultracut R microtome (Leica Microsystem, Vienna, Austria) with a Diatome diamond knife (Diatome, Biel, Switzerland) and double-stained with uranyl acetate replacement and lead citrate. Sections were viewed in a in a 120 kV JEM1400 Flash Transmission Electron Microscope (Jeol Ltd, Tokyo, Japan) equipped with CMOS camera Matataki and SightX Viewer software (Jeol Ltd, Tokyo, Japan) at 80 kV.

6 Third breakthrough

Identification and characterization of a new pathological variant in the SIL1 gene causing Marinesco-Sjögren's syndrome

Unpublished data

Rationale

This research project is a collaborative effort initiated last year with a Greek research group. The geneticist leading the group identified a novel mutation in the SIL1 gene through genomic sequencing in a pediatric patient, a mutation previously unreported. Subsequently, our team was engaged to conduct a molecular analysis of this mutation's functional consequences and to determine its pathogenicity. The ultimate goal of this study is to make a so-called “molecular diagnosis” of Marinesco-Sjögren syndrome.

The 3-year-old patient presented with ataxia, muscle weakness, and cataracts, the classic triad used to make a clinical diagnosis of MSS. Whole exome sequencing revealed a new c.1024G>A mutation in the SIL1 gene. Multiple in-silico analyses suggested that this variant of unknown significance (VUS) is likely pathogenic. The disruption of the three-dimensional organization of the recombinant mutant protein (p.E342K) was revealed by circular dichroism and native gel electrophoresis. Primary skin fibroblasts isolated from the patient carrying the new SIL1 variant have ten times less SIL1 protein than healthy control fibroblasts, most likely because the protein is misfolded and thus degraded. In fact, inhibition of proteasome activity increased the amount of SIL1 protein. Proteomic analysis of these fibroblasts revealed a typical protein expression pattern and ontologies enrichment overlapping that of MSS patients carrying the R111X mutation and SIL1Gt mouse model of MSS. In addition, they showed a transcription signature characteristic of MSS. Finally, ultrastructural analysis showed the presence of autophagic vacuoles and accumulation of lipid droplets similar to fibroblasts from a patient with a declared MSS. Overall, these evidences support the hypothesis that the novel p.E342K variant is pathological and thus explain the clinical manifestations observed in the patient carrying this mutation.

Results

In silico analysis suggests that the c.1024G>A variant alters the structure of SIL1 and confers a pathogenic role to the protein

This study delved into the functional consequences of a novel mutation, specifically p.E342K, within the SIL1 gene, a genetic variant linked to Marinesco-Sjögren syndrome (MSS). The primary focus was on examining the expression, stability, and structural properties of both the mutant and the wild-type SIL1 proteins.
Thanks to a collaboration with the Analytical Sciences Institute in Lyon, a researcher from our group began by expressing both the mutant and wild-type SIL1 proteins in *E. coli* bacteria, tagging them with a GST protein for purification purposes.
Biochemical and structural analysis (data not shown) revealed a profound impact of the p.E342K mutation on the SIL1 protein. The mutant variant exhibited marked instability and a significant alteration of its three-dimensional conformation compared to the wild-type protein. In particular, a substantial loss of the alpha-helical secondary structure, typical of the native protein, was observed in favor of a coiled-coil conformation, associated with a higher propensity for aggregation. These data suggest that the mutation in question critically compromises the biological function of the SIL1 protein, significantly altering its stability and ability to interact with other molecules.

The p.E342K variant exhibits poor solubility and forms intracellular aggregates when expressed in COS7 cells

Previous studies have demonstrated that pathogenic mutations in the SIL1 gene cause abnormal migration of the protein during native gel electrophoresis and the formation of protein aggregates when expressed in COS7 or HEK293 cells[9,45]. To determine whether the p.E342K variant exhibits a similar phenotype, we conducted a series of experiments. Initially, we assessed the expression levels of wild-type SIL1 protein, the p.E342K variant, and the pathogenic p.L457P mutant in COS7 cells. Western blot analysis confirmed comparable expression levels for all three proteins (Figure 6.1. A). However, while both wild-type and mutant variants were secreted into the culture medium, the amounts of secreted p.E342K and p.L457P were approximately 10-fold lower, suggesting potential solubility issues (Figure 6.1. B).

Subsequently, we examined the solubility of these proteins under native conditions. Both the p.E342K variant and p.L457P showed significantly reduced solubility compared to the wild-type protein (Figure 6.1. C). Further analysis using a denaturing buffer confirmed that the reduced solubility was not due to decreased expression, but rather to intrinsic properties of the mutant proteins.

Finally, by immunofluorescence microscopy, we observed numerous SIL1 aggregates in COS7 cells expressing either the p.E342K or p.L457P variant, whereas aggregates were almost absent in cells expressing the wild-type protein (Figure 6.1. D).

In conclusion, our results demonstrate that the p.E342K variant exhibits phenotypic characteristics similar to the pathogenic p.L457P mutation, such as reduced solubility and a propensity to form aggregates, differing significantly from the wild-type protein. These data strongly support the hypothesis that the p.E342K mutation is pathogenic and contributes to the disease phenotype.

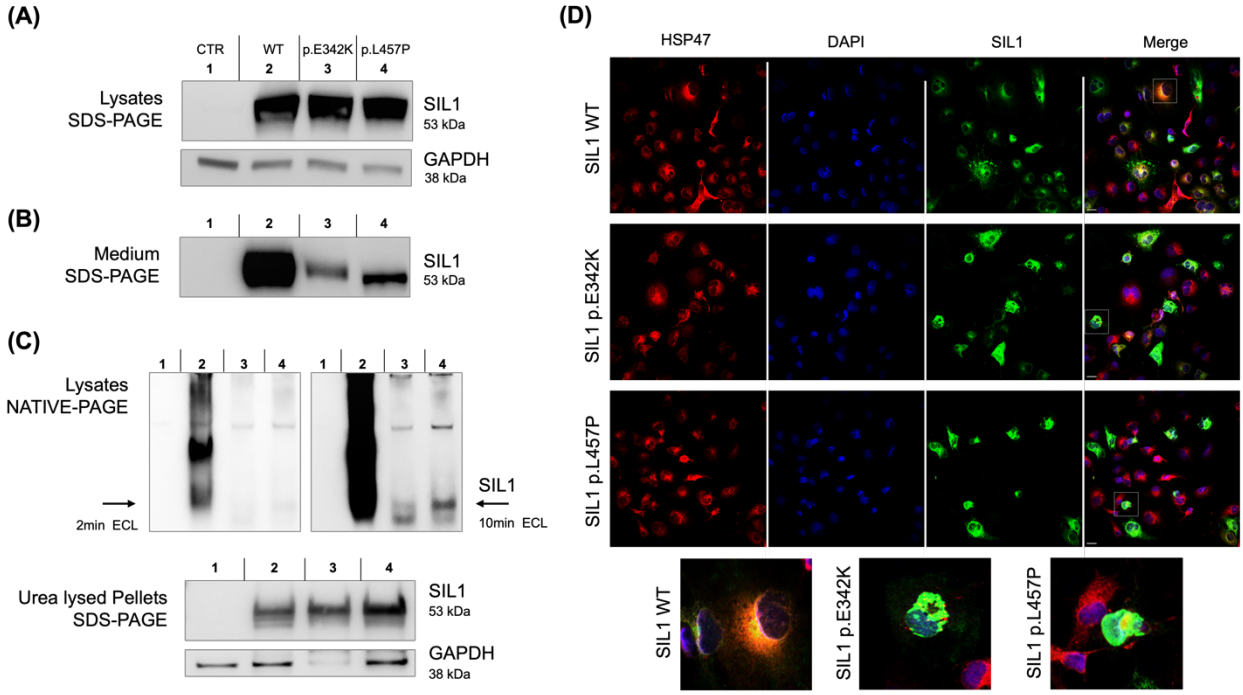


Figure 6.1 Characterization of the new mutation, in COS7 cells. Panels on the left show results on COS7 cells transfected with WT hSIL1, p.E342K SIL1 new mutant and p.L457P known SIL1 mutant. (A) COS7 transfected cell lysate ran on a classical SDS-PAGE. (B) SDS-PAGE of the conditioned medium producede by COS7 transfected cells. (C) upper panel display results from a NATIVE-PAGE, in the lower panel results from the insoluble fraction from the native-page lysed in Urea buffer. Panel (D) confocal images displaying aggregation capacity of SIL1 WT vs SIL1 mutants, by immunofluorescent staining. Digital zoom of the aggregates at the bottom.

Unpublished data

Fibroblasts from patients carrying the p.E342K variant exhibit a gene expression profile characteristic of MSS and reduced levels of SIL1 due to proteasomal degradation

Analyses conducted on the p.E342K mutation revealed a significant alteration in the stability and cellular fate of the SIL1 protein. In particular, we observed a marked reduction in SIL1 protein levels (Figure 6.2. D and E), attributable to an increased rate of degradation mediated by the proteasome and lysosome. Furthermore, gene expression profiling revealed significant alterations in numerous genes, suggesting a broader impact of the mutation on cellular physiology (data not shown). Although the p.E342K mutation induces a pathological phenotype, the data obtained indicate that the phenotypic effects associated with this mutation are less severe than those induced by other previously characterized mutations in the SIL1 gene[14,46].

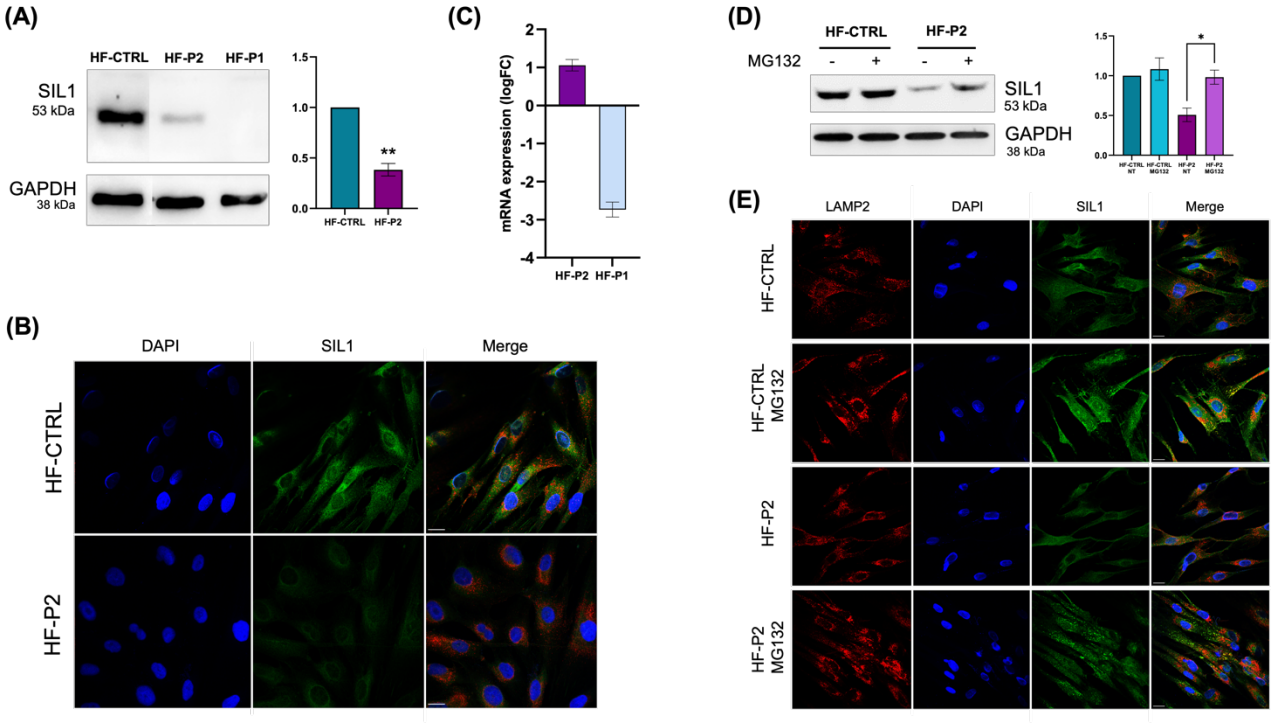


Figure 6.2. HF-P2 primary skin fibroblast characterization. (A) WB analysis and quantification of SIL1 protein levels in both patient 1 and 2. (B) Confocal image of SIL1 protein in patient 2 by immunofluorescent staining. (C) mRNA expression levels of SIL1 transcript in both patient 1 and 2. (D) and (E) MG132 proteosome inhibition treatment. (D) WB quantification and analysis of patient 2 fibroblasts treatment with MG132. **(E)** Immunofluorescent analysis of patient 2 fibroblasts after MG132 treatment.

Unpublished data

Fibroblasts from patients carrying the p.E342K variant show an enlargement of the lysosomal compartment and a cytosolic accumulation of lipid droplets and fibrotic material

In our previous works, we demonstrated that HF-P1 cells exhibit a high number of LAMP1-positive structures, appearing as vacuoles under transmission electron microscopy (TEM)[14,46]. Analyzing HF-P2 cells, we observed a significant increase in these structures and the presence of numerous lipid droplets and protein deposits in the cytoplasm Figure 6.3). These findings, also observed in HF-P1 cells, suggest that the morphological alterations observed are characteristic of Marinesco-Sjögren syndrome and support the hypothesis that the p.E342K mutation is pathogenic.

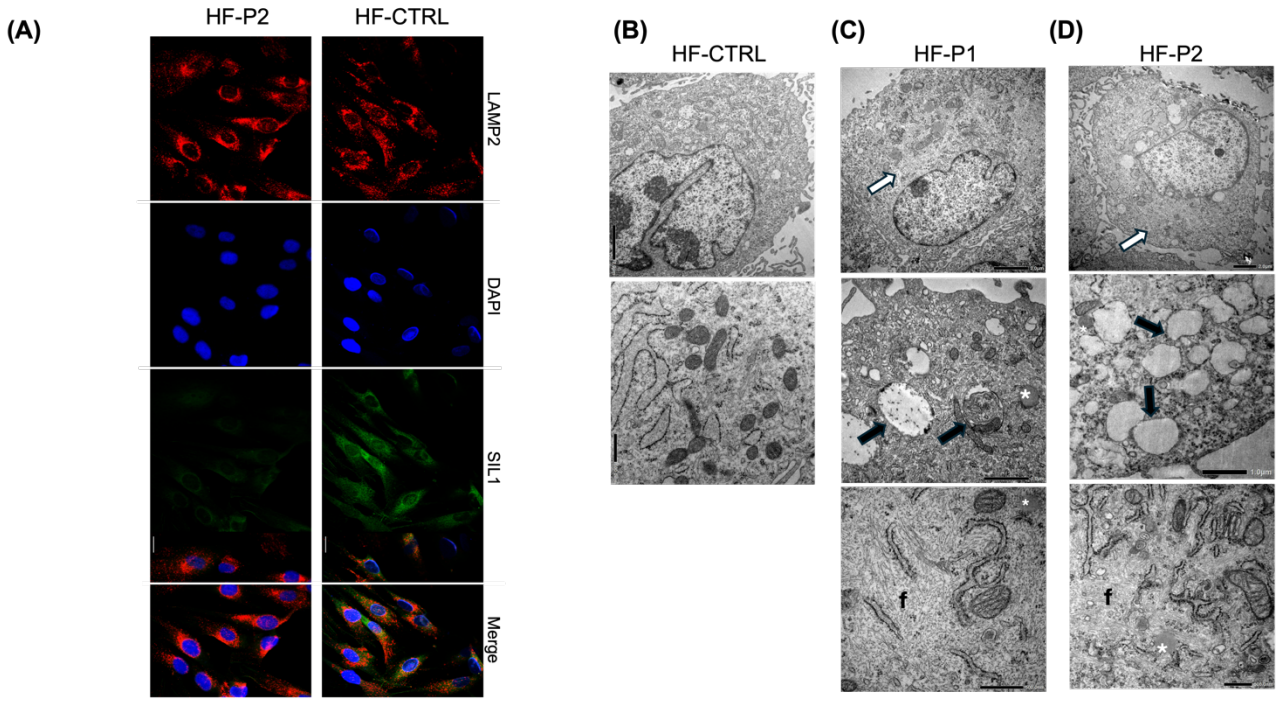


Figure 6.3. Analysis of lipid accumulation in HF-P2 fibroblast. Panel (A) Confocal microscopy images of lysosomes (LAMP2) in CTRL vs P2 staining. Panel (B) Transmission Electron Microscopy of both lipid accumulation (white arrows), multilamellar bodies or empty vacuoles (black arrows) and aberrant fibrillar structure (**f**).

Unpublished data

Proteomic analysis of fibroblasts from patients carrying the p.E342K variant revealed an altered proteostasis, characteristic of MSS

To further investigate the proteomic alterations in HF-P2 cells, we performed a high-resolution proteomic analysis. The results revealed significant differences in protein expression compared to control fibroblasts, with 122 proteins downregulated and 107 upregulated. To visualize the proteomic alterations more comprehensively, we generated heatmaps, which clearly highlight the distinct proteomic profile of patient cells compared to control cells (Figure 6.4 A).

(A)

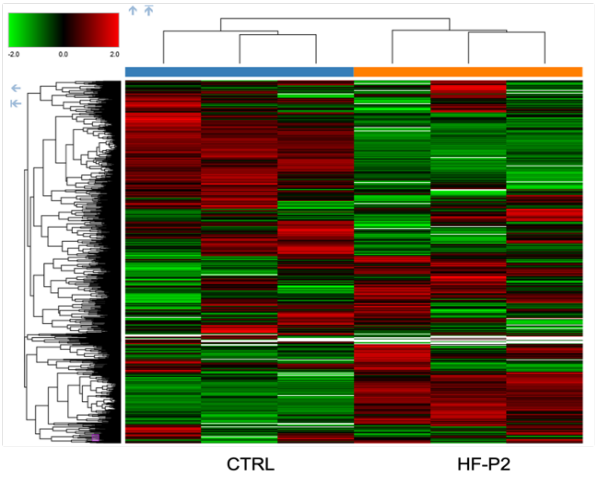


Figure 6.4. Proteomic data elaboration, Heatmap of the proteomic profile.
Unpublished data

A comparative analysis between the altered proteomes in HF-P2 and HF-P1 cells revealed a significant overlap, suggesting the existence of common molecular mechanisms underlying the phenotypic alterations associated with the two mutations. To further validate these results, we selected a subset of differentially expressed proteins and confirmed their altered expression levels by Western blotting (Figure 6.5 A).

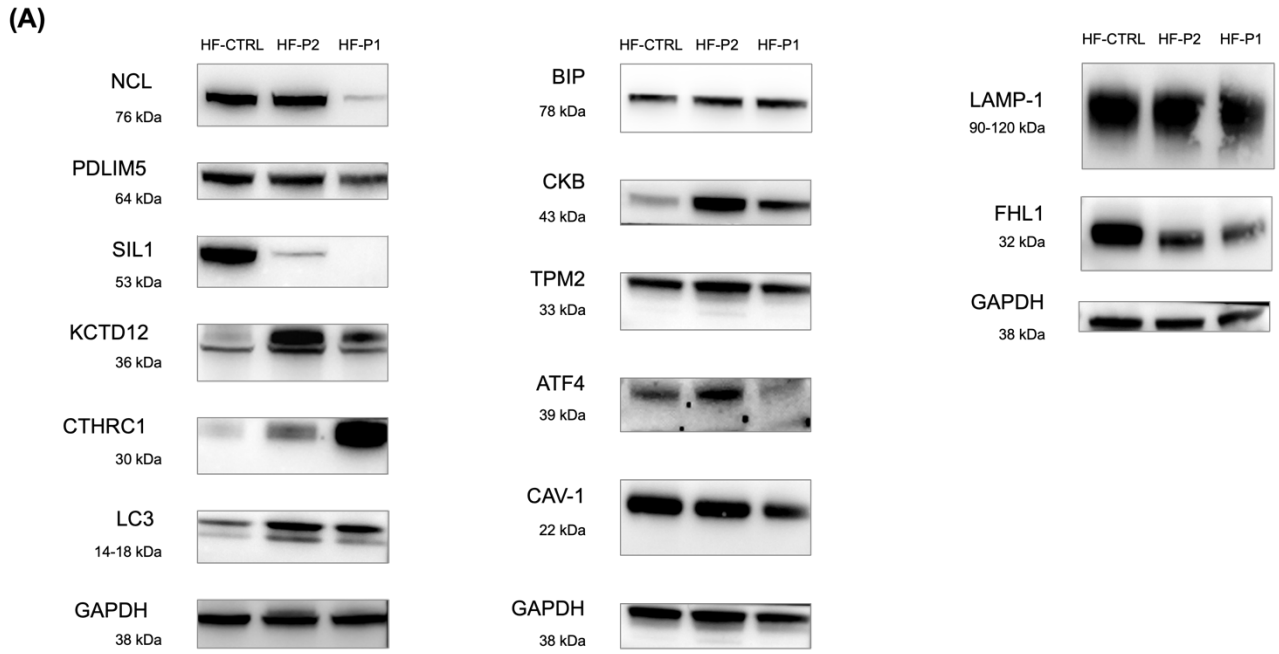


Figure 6.5 Proteomic validation via WB.
Unpublished data

To understand the functional relationships among the differentially expressed proteins, we utilized protein-protein interaction network analysis. The results indicate the formation of a highly significant interaction network, suggesting the existence of protein complexes modulated by the mutations. Gene ontology (GO) enrichment analysis revealed that the proteins involved in these networks are associated with a wide range of biological processes, including large ribosomal subunit biogenesis, cytoplasmic translation, regulation of cell adhesion, and oxidic acid metabolism (data not shown).
In conclusion, our proteomic results highlight a profound remodeling of the cellular proteome induced by the p.E342K mutation. The significant overlap with previously obtained proteomic data for HF-P1 cells further supports the hypothesis that this mutation is pathogenic and induces common molecular alterations.
My primary role involved immunofluorescence microscopy to investigate protein localization and in silico proteomics analysis to identify candidate proteins for subsequent validation via Western blot.

Discussion

We investigated a novel genetic variant, c.1024G>A, in the SIL1 gene linked to Marinesco-Sjögren syndrome (MSS). This variant replaces a glutamate with a lysine, potentially altering SIL1's structure and function. In vitro studies support this hypothesis, showing the mutant protein aggregates and has an altered structure.
Key findings include reduced SIL1 protein levels, altered gene expression, accumulation of lipid droplets, and a proteomic profile similar to other MSS cases. These results suggest that the c.1024G>A variant is pathogenic and contributes to MSS development. However, compared to other SIL1 mutations, this variant seems to cause a less severe form of the disease.

Material and methods

Plasmids

Mammalian gene expression vectors (pRP-CMV) were used to clone respectively the ORF of human SIL1 gene, its variant with the mutation c.1024G>A (p.E342K), and a pathogenic missense variant with the mutation c.1370T>C (p.L457P). These three constructs were provided by Vector Builder.

Cell culture

Cells were cultivated at 37°C in a CO_2 incubator, using Dulbecco's modified Eagle's medium GLUTAMAX (DMEM GLUTAMAX, GIBCO, 61965- 026) supplemented with 10% of Fetal Bovine Serum (FBS, GIBCO) and with 1% penicillin/streptomycin (PenStrep, GIBCO, 15070-063).
At 90% of confluence cells were subcultured and detached with Trypsin/EDTA 0.5% (GIBCO, 15400-054). As control cell line for patient fibroblasts, primary human dermal fibroblast (NDHF Promo Cell #FB60C12350) supplied by Carlo Erba Reagents were used.

Transfection

250,000/well COS-7 cells were plated in a 6-well with a coverslip the day before the experiment. The following day they were transfected with 3µg of respectively hSIL1, SIL1 mut. E342K and SIL1 mut. L457P, using Lipofectamine 3000 (Invitrogen #L3000015) according to manufacturer's instructions. For immunofluorescence analysis, after 18 hours of transfection, cycloheximide (25 µg/ml) was used for 2 hours to inhibit protein production. For western blot analysis, transfection was stopped after 72 hours.

Fluorescence Immunostaining and Confocal Microscopy

Cells seeded on coverslips were fixed, once 70% density was reached, in ice cold methanol for 5 min, -20°C. Cells were than processed according to our previously published study. Primary antibodies used for protein detection are listed in table 6.1. Fluorescence was detected using a LSM800 Zeiss confocal microscope and images were post-processed and analyzed using Fiji software.

SDS-PAGE and Western Blot Analysis

Cells were lysed and processed according to our previously published study cit. with the exception of the additional use of precast gel (Genscript #M00659 SurePAGE™, Bis-Tris, 10x8, 8-16%, 12 wells). Primary antibodies used for protein detection are listed in table 6.1.

Native-PAGE

Cells were lysed in gentle conditions following the instructions of Roychowdhury et al. Native lysis buffer was composed of 20mM Tris pH 7.4, 20mM KCl, 5mM $MgCl_2$ and 0.01% NP40, with the addition of protease and phosphatase inhibitor cocktails.
For lysis, samples were incubated for 10 min on dry ice, and for 2 minutes at 37°C water bath. This step was repeated three times and then samples were incubated on ice for 30 minutes. Following a 12,000-rpm centrifugation for 20 minutes at 4°C, supernatants and pellets were both collected. Pellets were lysed on ice for 30 minutes with native lysis buffer

added with 8M Urea, then sonicated and centrifuged again for 20 minutes at 4°C (12,000 rpm). Protein concentrations was measured with Bradford assay.
Pellets were processed through SDS-PAGE, while supernatants through native-PAGE. For native-PAGE electrophoresis, stacking gel (acrylamide 4%) running gel (acrylamide 10%) and running buffer (1X) were prepared without SDS, according to the instructions of Sino Biological Inc. Samples were loaded with 62.5mM Tris-HCl pH6.8, 25% glycerol and 1% Bromophenol Blue and they were not heated. Electrophoresis run was performed at 100V with the Bio-rad system placed on ice, and then transferred through western blot analysis.

Cell proliferation Assay

10,000 cells/well were plated in a 96-well plate the day before the experiment, and proliferation was monitored using a Click-iT Edu Proliferation assay kit (#C10499, Invitrogen) following the manufacturing instructions as already described in our previous study.

Motility Assay

According to the protocol for Incucyte Scratch Wound Assay 20,000 cells/well were plated in a 96-well ImageLock™ plate the day before the experiment. The day after, a uniform wound was created in each well through the 96-pin Incucyte WoundMaker (Sartorius), and then cells were incubated into Incucyte® Live Cell Analysis System (Incucyte® S3/ - Sartorius). Image acquisition and analysis of relative wound density were performed following the previously published protocol.

MG132 proteosome inhibition treatment

Western blot analysis: 250.000 cells were seeded in 60mm dish.
Immunofluorescent staining : 30.000 cells/well were seeded on coverslips in 24 multi well plate. The day after cells were treated with 20μM MG132 (Calbiochem #474790) in DMSO for 6h. After treatment, both coverslips and cells have been processed as described above.

Table 6.1 List of antibodies used

Target	Brand	Ref. code	Dil. WB	Dil. IF
BIP/GRP78	BD	610979	1:800	
CKB	Abcam	ab92452	1:5000	
CTHRC1	Abcam	ab5739	1:1000	
FHL1	Proteintech	10991-1-AP	1:1000	
GAPDH	Santacruz	sc-32233	1:2000	
KCTD12	Proteintech	15523-1-AP	1:500	
Lamp2a	Santacruz	sc-18822		1:100
PDLIM5	Protientech	10530-1-AP	1:500	
SIL1	Sigma Prestige	S-HPA011949	1:1000	1:100
Ubiquitin	Calbiochem		1:4000	

Quantitative real-time PCR (q-PCR)

For gene expression analysis, total RNA was extracted from cells using QIAzol (RNeasy Lipid Kit, QIAGEN Inc., Valencia, CA), according to the manufacturer's instructions. RNA quality and concentration were determined by NanoDrop 2000 spectrophotometry (Thermo Scientific, Wilmington, DE, USA) and integrity was verified by 1% agarose gel electrophoresis.

1µg total RNA was reverse transcribed into cDNA using the High Capacity cDNA Archive kit in accordance with the manufacturer's recommendations (Applied Biosystems). Relative quantification of gene expression was performed by RT-PCR using the CFX96 Real-Time PCR Detection System (Bio-Rad) and the SensiFAST SYBR kit (Bioline). Target gene levels in patient cells are presented as a ratio to levels detected in control cells according to the Ct method. Primers used for amplification were designed using IDT PrimerQuest Tool software and synthesized by Integrated DNA Technologies (IDT, Coralville, IA, USA). The primer sequences are shown in Table 6.1. Data analysis was performed using CFX Manager software (Bio-Rad). The relative expression of target genes was calculated using the ΔΔCt method, normalizing the expression of target genes to the reference gene (GAPDH). The results were expressed as fold change with respect to the control.

Table 6.1. Primer list

Target gene	Primer Forward (5'→3')	Primer Reverse (5'→3')
ACAN	CTG CTA TGG AGA CAA GGA TGA G	CTG GAG ATG TTG CAT AAA AGA CC
ALDH1A1	AGC AGG AGT GTT TAC CAA AGA	CCC AGT TCT CTT CCA TTT CCA G
CTHRC1	CAA TGG CAT TCC GGG TAC AC	GTA CAC TCC GCA ATT TTC CCA A
CTTNBP2	CCG TGG GAC TTT ATG AGG AAG	GAG GGA TCA TGG AGG CAT AAG
ELAPOR2	CCT GGC AAC ATG AAA ACT TCC	TCA TTG TCA GAA CCT CCA GC
EMB	ATA CCC AAT ACA GGT TCA CCA TC	CCC TAC GTA AGA GAT CAA TGG C
EXPH5	TGG GAC AGA AAG GAT GTG ATG	CTG GCT TTG GGA CAA ATG TAC
GPC4	AGG AAA CGG CAA TGA GGA TG	GAC GAA GGA TCA GTA TGT CTG G
LXN	ACA GAA CTA CAT CAA CTA CCA GC	GTG ATA CTT ATG TCC TCT TCC TGG
NRN1	ACA AGA CGA ACA TCA AGA CCG	TTA TCC CAC ATA TCT TTC GCC C
PCDH7	TGT CAA ACC AAT AAC AAG TAC AGC	ACT GCT TGG TGT TTC TGA CTC
PCOLCE2	GGG AAG TCA ACG ATG CTA GAA G	GTG ACC AAT AAA CCC ATC TGC
SIL1	GCT TCA CCT TCT GCC TCA GTC A	AAC ACC TCC AGG ACT TCG GCA T
VCAN	GGT GGT CTA CTT GGG GTG AG	GTG ATG CAG TTT CTG CGA GGA
GAPDH	CTG GGC TAC ACT GAG CAC C	AAG TGG TCG TTG AGG GCA ATG

7 Conclusions

Summary

To unravel the molecular mechanisms underlying Marinesco-Sjögren syndrome, we delved into a comprehensive proteomic and transcriptomic analysis of patient-derived skin fibroblasts. By systematically dissecting alterations in proteins and transcripts within relevant pathways, we gained valuable insights into the adaptive metabolic strategies employed by cells lacking SIL1.

Expanding our investigation, we conducted a similar proteomic analysis on fibroblasts from a second patient harboring an undisclosed genetic mutation. Comparative analysis of the same markers identified in the initial patient revealed a striking convergence in the adaptive mechanisms, albeit with a less pronounced effect. This intriguing observation suggests that the molecular phenotype is conserved and the second patient represents an intermediate state between the wild-type condition and the more severe phenotype associated with the known mutation.

At the same time, recognizing the limitations of fibroblasts as a model system for a disease primarily affecting muscle and Purkinje cells, we sought to develop a more physiologically relevant in vitro model. Leveraging CRISPR/Cas9 technology, we precisely engineered the murine C2C12 myoblast cell line to eliminate the SIL1 protein. This targeted genetic intervention resulted in a significant impairment of differentiation process, from myoblasts to myotubes, providing a potential mechanistic explanation for the myopathy observed in both patients and animal models. In effect, the analysis of muscle biopsies consistently revealed a characteristic set of alterations, including variability in fiber size, abnormal fast-to-slow fiber ratios, fibroadipose tissue infiltration, and nuclei internalization.

The phenotypic diversity observed among the five generated clones, both in terms of differentiation impairment and molecular marker expression, necessitated the pursuit of a more phenotypically stable *in vitro* model with a genetic background closely mirroring the human and mouse condition. To achieve this, we opted for a direct approach, isolating both myoblasts and fibroblasts from the Woozy mouse, a well-established animal model for Marinesco-Sjögren syndrome. Preliminary molecular analysis of these primary cells revealed a consistent pattern with that observed in patients-derived fibroblasts. While we refine our extraction protocols to obtain purer cell cultures, we also explore the potential

benefits of a mixed culture system, which could provide valuable insights into the complex interactions between muscle cells and matrix-producing cells.

Discussion on key findings

- **Unfolded Protein Response:** Patient skin fibroblasts exhibited only a mild unfolded protein response, characterized by increased ER stress markers and reduced protein synthesis. No increase in ORP150 was found.

The discrepancy between the modest UPR activation in patient fibroblasts and the robust response described by Roos et al. [7] relies on fibroblasts not being the primary cell type affected by the disease. This, in turn, suggests that these cells have developed compensatory mechanisms that allow them to cope with the absence of SIL1 and mitigate somehow the ER stress.
ORP150 can function as a nucleotide exchange factor for BiP, and elevated ORP150 levels have been suggested to compensate for SIL1 loss in surviving cells [13]. However, we did not observe increased ORP150 levels in our patient fibroblasts compared to controls. We hypothesize that the actual levels present in patient fibroblasts are sufficient to cope with SIL1 loss.

- **Metabolic Adaptations:** To compensate for Sil1 loss and maintain cell survival, the cells underwent metabolic adaptations, including increased fatty acid and amino acid catabolism, TCA cycle activation, and mitochondrial ATP synthase upregulation.

- **ER-Mitochondria Coupling:** The study highlighted the importance of ER-mitochondria contacts in maintaining ATP coupling and found increased mitofusin-2 expression.

The endoplasmic reticulum (ER) is a cellular organelle that heavily relies on ATP for its functions, including protein folding, trafficking, and ion homeostasis. However, it lacks its own ATP-generating machinery[28]. To meet its energy demands, the ER primarily relies on ATP produced by mitochondria via oxidative phosphorylation[47]. This

dependence is especially pronounced during cellular stress, such as the unfolded protein response (UPR), when the ER's ATP consumption increases significantly. ATP is transported into the ER through the solute carrier family 35 member B1 (SLC35B1) located at the ER-mitochondria contact sites[28]. These contact sites are crucial for coordinating ATP production and consumption. In heart failure with preserved ejection fraction (HF-pEF), the expression of mitofusin-2, a key protein involved in maintaining ER-mitochondria contacts, is upregulated, suggesting an increased reliance on mitochondrial ATP supply to support ER function in this disease state[30].

- **Spliceosome and Histones Downregulation:** Proteomic analysis revealed downregulation of RNA splicing and transport machinery, ribosomes, and translation initiation, which might be attributed to reduced protein synthesis due to the unfolded protein response. Downregulation of histone proteins production also emerged.

A similar splicing alteration has been reported in over 300 cancer cell lines exposed to diverse anticancer treatments, indicating a common stress response mechanism that promotes cell survival [26]. The spliceosome, a critical molecular machine involved in gene expression, is downregulated during cellular senescence [27]. In line with accelerated cellular aging, HF-MSS cells display a reduction in histone proteins, a well-established hallmark of senescence [48]. Furthermore, these cells exhibit increased cell size, another characteristic feature of senescent cells [49]. The observed reduced proliferation rate of HF-MSS cells further supports the hypothesis that these cells undergo a form of cellular senescence as a survival strategy.

- **Aberrant ECM production :** Transcriptomic analysis of patient-derived fibroblasts as well as TEM analysis on woozy mice muscles and tendons, has revealed significant alterations in ECM production, remodeling, and cell-matrix interactions.

The extracellular matrix (ECM) is a critical component of various tissues, including the brain, muscle, and cartilage. It plays a significant role in tissue development, repair, and function. In the brain, the ECM influences neuronal development, synaptic plasticity, and neurotransmitter signaling[42]. Alterations in ECM components have been

linked to neurodegenerative diseases like Alzheimer's, Huntington's, Parkinson's, epilepsy, and ataxia[50].

Spinocerebellar ataxia type 1 (SCA1) is a neurodegenerative disorder associated with ECM alterations. Genes involved in ECM production and remodeling, such as collagens, laminins, integrins, and matrix metalloproteinases, are dysregulated in SCA1[51]. Additionally, alterations in semaphorin genes and downregulation of ARNT2, a regulator of ECM gene expression, have been observed in SCA1[52].

In skeletal muscle, the ECM is essential for satellite cell function and muscle regeneration. ECM alterations contribute to muscle weakness and sarcopenia[53]. Mutations in ECM genes, particularly collagens and laminins, can lead to muscular dystrophies[54]. Furthermore, ECM disturbances have been linked to cataracts, a common clinical manifestation of SCA1. Versican, a proteoglycan overexpressed in SCA1, may contribute to cataract formation.

Skeletal abnormalities in SCA1 patients may be related to alterations in cartilage ECM. Mutations in cartilage ECM components can lead to chondrodysplasias, characterized by bone deformities[55,56].

The relationship between ER stress and ECM is complex. ER stress can induce ECM production and remodeling, and conversely, ECM alterations can impact ER stress responses. These findings suggest that the UPR may play a role in regulating ECM homeostasis and that disturbances in this pathway may contribute to the development of ECM-related diseases[57,58].

- **C2C12 SIL1 KO Clones_Differentiation Defects:** The five generated CRISPR clones showed the inability to differentiate from myoblasts to myotubes. Although the do not present with the expected molecular pattern typical of MSS.

The difficulty of myoblasts to differentiate into myotubes, as observed in genetically modified clones lacking SIL1, could be explained by the production of an altered extracellular matrix that lacks the essential components normally required for myoblast differentiation[46]. While these engineered clones may not exhibit the molecular signature characteristic of MSS, primary cultures of myoblasts and fibroblasts from the woozy mouse could address this issue. Moreover, primary cell lines could provide a more suitable co-culture system for investigating the communication between the

extracellular matrix of fibroblasts and muscle cells undergoing differentiation in the appropriate microenvironment.

- **Gene expression signature:**

In our transcriptomic analysis[46], we identified a distinctive molecular signature associated with MSS, consisting of 12 transcripts with significantly altered expression levels. We indeed confirmed the altered expression of 10 of these key transcripts in fibroblasts carrying the novel p.E342K mutation in the SIL1 gene. The extent of these gene expression changes was more pronounced in the HF-P1 patient than in the HF-P2 patient, suggesting that the novel p.E342K mutation may be less severe. However, a clear correlation between SIL1 mutations and the severity of the clinical phenotype has yet to be established [2,59].

- **Lipid droplets accumulation:**

Protein degradation was found to be dependent on a functional proteasome, and its inhibition resulted in the misfolded proteins being targeted to the lysosomal compartment for degradation. As reported in numerous previous studies, including our own[2,14,22], the lysosomal compartment, which is enlarged in MSS, plays a critical role in this process. Additionally, we observed an accumulation of lipid droplets, suggesting a metabolic shift in MSS, particularly in lipid metabolism. Our study of the HF-P1 patient demonstrated a decrease in de novo lipogenesis and an increase in beta-oxidation. Intriguingly, lipid droplet accumulation and dysfunction have been associated with several neurodegenerative diseases, including ALS, Huntington's disease, Parkinson's disease, and Alzheimer's disease [60].

Conclusion & further research

Despite not being the primary cell type affected by the pathology, fibroblasts have proven to be a useful model for studying the adaptive mechanisms in response to SIL1 deficiency. On the other side, to fully understand the complex cellular processes involved, there is the strong need to develop a robust in vitro model of the mainly

affected cells. These models will pave the way for new functional experiments to dissect the molecular pathways underlying the disease phenotype and to identify potential therapeutic targets to restore cellular homeostasis.

8 Bibliography

1. Anttonen, A.-K. Marinesco-Sjögren Syndrome. in *GeneReviews®* (eds. Adam, M. P. et al.) (University of Washington, Seattle, Seattle (WA), 1993).
2. Krieger, M. *et al.* SIL1 mutations and clinical spectrum in patients with Marinesco-Sjögren syndrome. *Brain* **136**, 3634–3644 (2013).
3. Chiesa, R. & Sallese, M. Review: Protein misfolding diseases – the rare case of Marinesco-Sjögren syndrome. *Neuropathol. Appl. Neurobiol.* **46**, 323–343 (2020).
4. Ichhaporia, V. P. & Hendershot, L. M. Role of the HSP70 Co-Chaperone SIL1 in Health and Disease. *Int. J. Mol. Sci.* **22**, 1564 (2021).
5. Bayram, N. *et al.* Genotype-phenotype correlations in ocular manifestations of Marinesco-Sjögren syndrome: Case report and literature review. *Eur. J. Ophthalmol.* **32**, NP92–NP97 (2022).
6. Mahjneh, I. *et al.* Myopathy is a prominent featurein Marinesco-Sjögren syndrome. *J. Neurol.* **253**, 301–306 (2006).
7. Roos, A. *et al.* Myopathy in Marinesco–Sjögren syndrome links endoplasmic reticulum chaperone dysfunction to nuclear envelope pathology. *Acta Neuropathol. (Berl.)* **127**, 761–777 (2014).
8. Xu, Y. *et al.* Loss of SIL1 Affects Actin Dynamics and Leads to Abnormal Neural Migration. *Mol. Neurobiol.* (2024) doi:10.1007/s12035-024-04272-8.
9. Inaguma, Y. *et al.* SIL1, a causative cochaperone gene of Marinesco-Sjögren syndrome, plays an essential role in establishing the architecture of the developing cerebral cortex. *EMBO Mol. Med.* **6**, 414–429 (2014).

10. Chung, K. T., Shen, Y. & Hendershot, L. M. BAP, a Mammalian BiP-associated Protein, Is a Nucleotide Exchange Factor That Regulates the ATPase Activity of BiP*. *J. Biol. Chem.* **277**, 47557–47563 (2002).
11. Behnke, J., Feige, M. J. & Hendershot, L. M. BiP and its nucleotide exchange factors Grp170 and Sil1: mechanisms of action and biological functions. *J. Mol. Biol.* **427**, 1589–1608 (2015).
12. Walter, P. & Ron, D. The Unfolded Protein Response: From Stress Pathway to Homeostatic Regulation. *Science* **334**, 1081–1086 (2011).
13. Zhao, L., Rosales, C., Seburn, K., Ron, D. & Ackerman, S. L. Alteration of the unfolded protein response modifies neurodegeneration in a mouse model of Marinesco–Sjögren syndrome. *Hum. Mol. Genet.* **19**, 25–35 (2010).
14. Potenza, F. *et al.* Proteomic Analysis of Marinesco-Sjögren Syndrome Fibroblasts Indicates Pro-Survival Metabolic Adaptation to SIL1 Loss. *Int. J. Mol. Sci.* **22**, 12449 (2021).
15. Ichhaporia, V. P. *et al.* SIL1, the endoplasmic-reticulum-localized BiP co-chaperone, plays a crucial role in maintaining skeletal muscle proteostasis and physiology. *Dis. Model. Mech.* **11**, dmm033043 (2018).
16. Kaufman, R. J. Orchestrating the unfolded protein response in health and disease. *J. Clin. Invest.* **110**, 1389–1398 (2002).
17. Capone, V. *et al.* PERK inhibition attenuates the abnormalities of the secretory pathway and the increased apoptotic rate induced by SIL1 knockdown in HeLa cells. *Biochim. Biophys. Acta BBA - Mol. Basis Dis.* **1864**, 3164–3180 (2018).
18. Grande, V. *et al.* PERK inhibition delays neurodegeneration and improves motor function in a mouse model of Marinesco-Sjögren syndrome. *Hum. Mol. Genet.* **27**, 2477–2489 (2018).

19. Kashimada, A. *et al.* Targeting the enhanced ER stress response in Marinesco-Sjögren syndrome. *J. Neurol. Sci.* **385**, 49–56 (2018).
20. Fischell, J. M. & Fishman, P. S. A Multifaceted Approach to Optimizing AAV Delivery to the Brain for the Treatment of Neurodegenerative Diseases. *Front. Neurosci.* **15**, (2021).
21. Phan, V. *et al.* SIL1 deficiency causes degenerative changes of peripheral nerves and neuromuscular junctions in fish, mice and human. *Neurobiol. Dis.* **124**, 218–229 (2019).
22. Zhao, L., Longo-Guess, C., Harris, B. S., Lee, J.-W. & Ackerman, S. L. Protein accumulation and neurodegeneration in the woozy mutant mouse is caused by disruption of SIL1, a cochaperone of BiP. *Nat. Genet.* **37**, 974–979 (2005).
23. Giau, V. V., Lee, H., Shim, K. H., Bagyinszky, E. & An, S. S. A. Genome-editing applications of CRISPR–Cas9 to promote in vitro studies of Alzheimer's disease. *Clin. Interv. Aging* **13**, 221–233 (2018).
24. Hentschel, A. *et al.* Protein signature of human skin fibroblasts allows the study of the molecular etiology of rare neurological diseases. *Orphanet J. Rare Dis.* **16**, 73 (2021).
25. Parenti, G., Andria, G. & Ballabio, A. Lysosomal Storage Diseases: From Pathophysiology to Therapy. *Annu. Rev. Med.* **66**, 471–486 (2015).
26. Anufrieva, K. S. *et al.* Therapy-induced stress response is associated with downregulation of pre-mRNA splicing in cancer cells. *Genome Med.* **10**, 49 (2018).
27. Kwon, S. M. *et al.* Global spliceosome activity regulates entry into cellular senescence. *FASEB J.* **35**, e21204 (2021).
28. Zimmermann, R. & Lang, S. A Little AXER ABC: ATP, BiP, and Calcium Form a Triumvirate Orchestrating Energy Homeostasis of the Endoplasmic Reticulum. *Contact* **3**, 2515256420926795 (2020).

29. Filadi, R., Pendin, D. & Pizzo, P. Mitofusin 2: from functions to disease. *Cell Death Dis.* **9**, 1–13 (2018).
30. Moore, K. & Hollien, J. Ire1-mediated decay in mammalian cells relies on mRNA sequence, structure, and translational status. *Mol. Biol. Cell* **26**, 2873–2884 (2015).
31. Filocamo, M. *et al.* Cell Line and DNA Biobank From Patients Affected by Genetic Diseases. *Open J. Bioresour.* **1**, (2014).
32. Brocco, D. *et al.* Phenotypic and Proteomic Analysis Identifies Hallmarks of Blood Circulating Extracellular Vesicles in NSCLC Responders to Immune Checkpoint Inhibitors. *Cancers* **13**, 585 (2021).
33. Falasca, K. *et al.* Circulating extracellular vesicles as new inflammation marker in HIV infection. *AIDS* **35**, 595 (2021).
34. Li, L. *et al.* Advances in research on cell models for skeletal muscle atrophy. *Biomed. Pharmacother.* **167**, 115517 (2023).
35. Myotube - an overview | ScienceDirect Topics. https://www.sciencedirect.com/topics/medicine-and-dentistry/myotube.
36. Ran, F. A. *et al.* Genome engineering using the CRISPR-Cas9 system. *Nat. Protoc.* **8**, 2281–2308 (2013).
37. Feng, L., Chen, Z. & Bian, H. Skeletal muscle: molecular structure, myogenesis, biological functions, and diseases. *MedComm* **5**, e649 (2024).
38. Kaur, G. & Dufour, J. M. Cell lines. *Spermatogenesis* **2**, 1–5 (2012).
39. Bravo, J. I., Kim, M. & Benayoun, B. A. Protocol for isolation of adult mouse ear pinnae-derived primary fibroblasts. *STAR Protoc.* **2**, 100406 (2021).
40. Tai, Y. *et al.* Myofibroblasts: Function, Formation, and Scope of Molecular Therapies for Skin Fibrosis. *Biomolecules* **11**, 1095 (2021).
41. Vaughan, M. & Lamia, K. A. Isolation and Differentiation of Primary Myoblasts from Mouse Skeletal Muscle Explants. *J. Vis. Exp. JoVE* (2019) doi:10.3791/60310.

42. Dzobo, K. & Dandara, C. The Extracellular Matrix: Its Composition, Function, Remodeling, and Role in Tumorigenesis. *Biomim. Basel Switz.* **8**, 146 (2023).
43. Kvist, A. J. *et al.* Chondroitin sulfate perlecan enhances collagen fibril formation. Implications for perlecan chondrodysplasias. *J. Biol. Chem.* **281**, 33127–33139 (2006).
44. Wederell, E. D. & de Iongh, R. U. Extracellular matrix and integrin signaling in lens development and cataract. *Semin. Cell Dev. Biol.* **17**, 759–776 (2006).
45. Gatz, C. *et al.* Identification of Cellular Pathogenicity Markers for SIL1 Mutations Linked to Marinesco-Sjögren Syndrome. *Front. Neurol.* **10**, (2019).
46. Amodei, L. *et al.* Sil1-deficient fibroblasts generate an aberrant extracellular matrix leading to tendon disorganisation in Marinesco-Sjögren syndrome. *J. Transl. Med.* **22**, 787 (2024).
47. Yong, J. *et al.* Mitochondria supply ATP to the ER through a mechanism antagonized by cytosolic Ca2+. *eLife* **8**, e49682 (2019).
48. Prado, F., Jimeno-González, S. & Reyes, J. C. Histone availability as a strategy to control gene expression. *RNA Biol.* **14**, 281–286 (2017).
49. Lanz, M. C. *et al.* Increasing cell size remodels the proteome and promotes senescence. 2021.07.29.454227 Preprint at https://doi.org/10.1101/2021.07.29.454227 (2021).
50. Pintér, P. & Alpár, A. The Role of Extracellular Matrix in Human Neurodegenerative Diseases. *Int. J. Mol. Sci.* **23**, 11085 (2022).
51. Opal, P. & Ashizawa, T. Spinocerebellar Ataxia Type 1. in *GeneReviews*® (eds. Adam, M. P. et al.) (University of Washington, Seattle, Seattle (WA), 1993).
52. Rahim, T., Becquart, P., Baeva, M.-E. & Quandt, J. Expression of the neuroprotective protein aryl hydrocarbon receptor nuclear translocator 2 correlates with neuronal stress and disability in models of multiple sclerosis. *J. Neuroinflammation* **15**, 270 (2018).

53. Melouane, A., Yoshioka, M. & St-Amand, J. Extracellular matrix/mitochondria pathway: A novel potential target for sarcopenia. *Mitochondrion* **50**, 63–70 (2020).
54. Barraza-Flores, P., Bates, C. R., Oliveira-Santos, A. & Burkin, D. J. Laminin and Integrin in LAMA2-Related Congenital Muscular Dystrophy: From Disease to Therapeutics. *Front. Mol. Neurosci.* **13**, (2020).
55. Gibson, B. G. & Briggs, M. D. The aggrecanopathies; an evolving phenotypic spectrum of human genetic skeletal diseases. *Orphanet J. Rare Dis.* **11**, 86 (2016).
56. Cho, S. Y. *et al.* BGN Mutations in X-Linked Spondyloepimetaphyseal Dysplasia. *Am. J. Hum. Genet.* **98**, 1243–1248 (2016).
57. Chen, X., Shi, C., He, M., Xiong, S. & Xia, X. Endoplasmic reticulum stress: molecular mechanism and therapeutic targets. *Signal Transduct. Target. Ther.* **8**, 1–40 (2023).
58. Schinzel, R. T. *et al.* The Hyaluronidase, TMEM2, Promotes ER Homeostasis and Longevity Independent of the UPRER. *Cell* **179**, 1306-1318.e18 (2019).
59. Ezgu, F. *et al.* Phenotype–genotype correlations in patients with Marinesco–Sjögren syndrome. *Clin. Genet.* **86**, 74–84 (2014).
60. Cerasuolo, M. *et al.* Exploring the Dynamic Changes of Brain Lipids, Lipid Rafts, and Lipid Droplets in Aging and Alzheimer's Disease. *Biomolecules* **14**, 1362 (2024).